STATE OF THE CLIMATE IN 2021

THE TROPICS

H. J. Diamond and C. J. Schreck, Eds.

Special Online Supplement to the *Bulletin of the American Meteorological Society*, Vol.103, No. 8, August 2022

https://doi.org/10.1175/BAMS-D-22-0069.1.

Corresponding author: Howard J. Diamond / howard.diamond@noaa.gov

STATE OF THE CLIMATE IN 2021
The Tropics

Editors
Jessica Blunden
Tim Boyer

Chapter Editors

Freya Aldred
Peter Bissolli
Kyle R. Clem
Howard J. Diamond
Matthew L. Druckenmiller
Robert J. H. Dunn
Catherine Ganter
Nadine Gobron
Gregory C. Johnson
Rick Lumpkin
Ademe Mekonnen
John B. Miller
Twila A. Moon
Marilyn N. Raphael
Ahira Sánchez-Lugo
Carl J. Schreck III
Richard L. Thoman
Kate M. Willett
Zhiwei Zhu

Technical Editor

Laura Ohlmann

BAMS Special Editor for Climate

Michael A. Alexander

American Meteorological Society

Cover credit:
Hurricane Ida hits near the Louisiana and Mississippi border on August 29, 2021 bringing high winds, flooding and a dangerous storm surge as seen. © Warren Faidley, Getty

The Tropics is one chapter from the *State of the Climate in 2021* annual report and is available from https://doi.org/10.1175/BAMS-D-22-0069.1. Compiled by NOAA's National Centers for Environmental Information, *State of the Climate in 2021* is based on contributions from scientists from around the world. It provides a detailed update on global climate indicators, notable weather events, and other data collected by environmental monitoring stations and instruments located on land, water, ice, and in space. The full report is available from https://doi.org/10.1175/2022BAMSStateoftheClimate.1.

How to cite this document:

Citing the complete report:
Blunden, J. and T. Boyer, Eds., 2022: State of the Climate in 2021. *Bull. Amer. Meteor. Soc.,* **103** (8), Si–S465, https://doi.org/10.1175/2022BAMSStateoftheClimate.1.

Citing this chapter:
Diamond, H.J. and C. J. Schreck, Eds., 2022: The Tropics [in "State of the Climate in 2021"]. *Bull. Amer. Meteor. Soc.,* **103** (8), S193–S256, https://doi.org/10.1175/BAMS-D-22-0069.1.

Citing a section (example):
Halpert, M. S., M. L'Heureux, A. Kumar, E. Becker, and Z.-Z. Hu, 2022: ENSO and the tropical Pacific [in "State of the Climate in 2021"]. *Bull. Amer. Meteor. Soc.,* **103** (8), S199–S203, https://doi.org/10.1175/BAMS-D-22-0069.1.

Editor and Author Affiliations (alphabetical by name)

Allgood, Adam, NOAA/NWS Climate Prediction Center, College Park, Maryland
Becker, Emily J., University of Miami Rosenstiel School of Marine and Atmospheric Science, Miami, Florida
Blake, Eric S., NOAA/NWS National Hurricane Center, Miami, Florida
Bringas, Francis G., NOAA/OAR/AOML Physical Oceanography Division, Miami, Florida
Camargo, Suzana J., Lamont-Doherty Earth Observatory, Columbia University, Palisades, New York
Chen, Lin, Institute for Climate and Application Research (ICAR)/KLME/ILCEC/CIC-FEMD, Nanjing University of Information Science and Technology, Nanjing, China
Coelho, Caio A. S., CPTEC/INPE Center for Weather Forecasts and Climate Studies, National Institute for Space Research, Cachoeira Paulista, Brazil
Diamond, Howard J., NOAA/OAR Air Resources Laboratory, College Park, Maryland
Fauchereau, Nicolas, National Institute of Water and Atmospheric Research, Ltd., Auckland, New Zealand
Goldenberg, Stanley B., NOAA/OAR/AOML Hurricane Research Division, Miami, Florida
Goni, Gustavo, NOAA/OAR/AOML Physical Oceanography Division, Miami, Florida
Halpert, Michael S., NOAA/NWS Climate Prediction Center, College Park, Maryland
He, Qiong, Earth System Modeling Center, Nanjing University of Information Science and Technology, Nanjing, China
Hu, Zeng-Zhen, NOAA/NWS Climate Prediction Center, College Park, Maryland
Klotzbach, Philip J., Department of Atmospheric Science, Colorado State University, Fort Collins, Colorado
Knaff, John A., NOAA/NESDIS Center for Satellite Applications and Research, Fort Collins, Colorado
Kumar, Arun, NOAA/NWS Climate Prediction Center, College Park, Maryland
Landsea, Chris W., NOAA/NWS National Hurricane Center, Miami, Florida
L'Heureux, Michelle, NOAA/NWS Climate Prediction Center, College Park, Maryland
Lin, I.-I., National Taiwan University, Taipei, Taiwan
Lorrey, Andrew M., National Institute of Water and Atmospheric Research, Ltd., Auckland, New Zealand
Luo, Jing-Jia, Institute for Climate and Application Research (ICAR)/KLME/ILCEC/CIC-FEMD, Nanjing University of Information Science and Technology, Nanjing, China
Magee, Andrew D., Centre for Water, Climate and Land, School of Environmental and Life Sciences, University of Newcastle, Callaghan, NSW, Australia
Pasch, Richard J., NOAA/NWS National Hurricane Center, Miami, Florida
Pezza, Alexandre B., Greater Wellington Regional Council, Wellington, New Zealand
Rosencrans, Matthew, NOAA/NWS Climate Prediction Center, College Park, Maryland
Schreck III, Carl J., North Carolina State University, North Carolina Institute for Climate Studies, Cooperative Institute for Satellite Earth System Studies, Asheville, North Carolina
Trewin, Blair C., Australian Bureau of Meteorology, Melbourne, Victoria, Australia
Truchelut, Ryan E., WeatherTiger LLC, Tallahassee, Florida
Wang, Bin, SOEST, Department of Meteorology and IPRC, University of Hawaii, Honolulu, Hawaii
Wang, Hui, NOAA/NWS Climate Prediction Center, College Park, Maryland
Wood, Kimberly M., Department of Geosciences, Mississippi State University, Mississippi State, Mississippi
Woolley, John-Mark, National Institute of Water and Atmospheric Research, Ltd., Auckland, New Zealand

Editorial and Production Team

Allen, Jessicca, Graphics Support, Cooperative Institute for Satellite Earth System Studies, North Carolina State University, Asheville, North Carolina
Hammer, Gregory, Content Team Lead, Communications and Outreach, NOAA/NESDIS National Centers for Environmental Information, Asheville, North Carolina
Love-Brotak, S. Elizabeth, Lead Graphics Production, NOAA/NESDIS National Centers for Environmental Information, Asheville, North Carolina
Misch, Deborah J., Graphics Support, Innovative Consulting and Management Services, LLC, NOAA/NESDIS National Centers for Environmental Information, Asheville, North Carolina
Ohlmann, Laura, Technical Editor, Innovative Consulting and Management Services, LLC, NOAA/NESDIS National Centers for Environmental Information, Asheville, North Carolina
Riddle, Deborah B., Graphics Support, NOAA/NESDIS National Centers for Environmental Information, Asheville, North Carolina
Veasey, Sara W., Visual Communications Team Lead, Communications and Outreach, NOAA/NESDIS National Centers for Environmental Information, Asheville, North Carolina

4. Table of Contents

*Please refer to Chapter 8 (Relevant datasets and sources) for a list of all climate variables and datasets used in this chapter for analyses, along with their websites for more information and access to the data.

4. THE TROPICS

H. J. Diamond and C. J. Schreck, Eds.

a. Overview—H. J. Diamond and C. J. Schreck

The tropics in 2021, in terms of the El Niño-Southern Oscillation (ENSO), featured La Niña episodes at both the beginning and end of the year. The year started with the continuation of a moderate strength La Niña (peak Oceanic Niño Index [ONI] value between –1.0° and –1.4°C is considered to be moderate strength) that had begun during July–September 2020 and ended during April–June 2021. The ONI then reflected a brief period of ENSO-neutral conditions May–July through June–August 2021, with the index increasing to –0.4°C, just greater than the minimum La Niña threshold of –0.5°C. Moderate La Niña conditions continued through the end of the year.

For the global tropics, NOAA GlobalTemp (Zhang et al. 2019) indicates the combined average land and ocean surface temperature (measured 20°S–20°N) was +0.07°C above the 1991–2020 average, tying with 1987 as the 12th-warmest year for the tropics since records began in 1880. While 2021 marked the coolest year since 2013, the five warmest years have all occurred since 2015. Data from the Global Precipitation Climatology Project indicate a mean annual total precipitation value of 1402.5 mm across the 20°S–20°N latitude band over land. This is just 0.5 mm below the 1991–2020 average and in the middle of all years (23rd wettest) for the 1979–2021 period of record.

Globally, 97 named tropical cyclones (TCs; maximum sustained winds ≥ 34 kt; or ≥ 17 m s^{-1}) were observed during the 2021 Northern Hemisphere season (January–December 2021) and the 2020/21 Southern Hemisphere season (July–June 2020/21; see Table 4.2), as documented in IBTrACSv4 (Knapp et al. 2010). Overall, this number was well above the 1991–2020 global average of 87 TCs but well below the 102 TCs reported during the 2020 season (Diamond and Schreck 2021) and the record 104 named storms in 1992. The 21 named storms in the North Atlantic during 2021 were the third most on record behind the 30 named storms from 2020 and the 28 in 2005. The 2021 season marked the second consecutive season, and third season overall, during which the designated list of 21 storm names was exhausted. For the North Atlantic, the seven hurricanes that occurred during 2021 were much less the 14 hurricanes in 2020. The four major hurricanes were also fewer than the seven observed in 2020.

Globally, Accumulated Cyclone Energy (ACE; Bell et al. 2000) was 13% higher in 2021 than in 2020, but still 18% below normal. The eastern North Pacific, western North Pacific, and Australian region each observed ACE in the bottom tercile of their 1991–2020 climatologies. The North Atlantic was more active than normal with 149% of the 1951–2020 median ACE.[1] This value is the 13th highest since 1970 and is above NOAA's threshold of 130% of the median ACE for an above-normal season. There have now been a record six consecutive above-normal seasons, which far surpasses the previous record of three set in 2003–05 and equaled in 2010–12. The western North Pacific observed four super typhoons in 2021 (Surigae, Chanthu, Mindulle, and Rai) that achieved Category 5 on the Saffir–Simpson Hurricane Wind Scale (SSHWS; https://www.nhc.noaa.gov/aboutsshws.php), but the overall ACE was still 30% below the 1991–2020 average. In total, there were seven Category 5 tropical cyclones across the globe—four in the western North Pacific and one each in the South Indian Ocean.

[1] Given the long-term North Atlantic hurricane record, we continue to use the 1951–2020 timeframe here to assist with year-to-year comparisons with past versions of The Tropics chapter.

b. ENSO and the tropical Pacific—M. S. Halpert, M. L'Heureux, A. Kumar, E. Becker, and Z.-Z. Hu

The El Niño-Southern Oscillation (ENSO) is a coupled ocean–atmosphere climate phenomenon centered across the tropical Pacific Ocean, with its opposite phases called El Niño and La Niña. For historical purposes, NOAA's Climate Prediction Center (CPC) classifies and assesses the strength and duration of El Niño and La Niña events using the Oceanic Niño Index (ONI, shown for mid-2020 through 2021 in Fig. 4.1). The ONI is the 3-month (seasonal) running average of sea surface temperature (SST) anomalies in the Niño-3.4 region (5°S–5°N, 170°–120°W), currently calculated as the departure from the 1991–2020 base period mean.[2] El Niño (the warm phase) is classified when the ONI is at or greater than +0.5°C for at least five consecutive, overlapping seasons, while La Niña (the cool phase) is classified when the ONI is at or less than −0.5°C for at least five consecutive, overlapping seasons.

The time series of the ONI (Fig. 4.1) shows that 2021 featured La Niña episodes at both the beginning and the end of the year. The year started with the continuation of a moderate strength La Niña (peak ONI value between −1.0° and −1.4°C is considered to be moderate strength) that began during July–September 2020 and ended during April–June 2021. The ONI then reflected a brief period of ENSO-neutral conditions May–July through June–August (JJA) 2021, with the index increasing to −0.4°C, just above the minimum La Niña threshold of −0.5°C. Starting in July–September (JAS) 2021, La Niña thresholds were again met, with ONI values decreasing through October–December (OND) 2021. In OND, the ONI reached −1.0°C, indicating that the second consecutive boreal winter (2021/22) would feature at least a moderate strength episode, albeit weaker than the previous winter (2020/21).

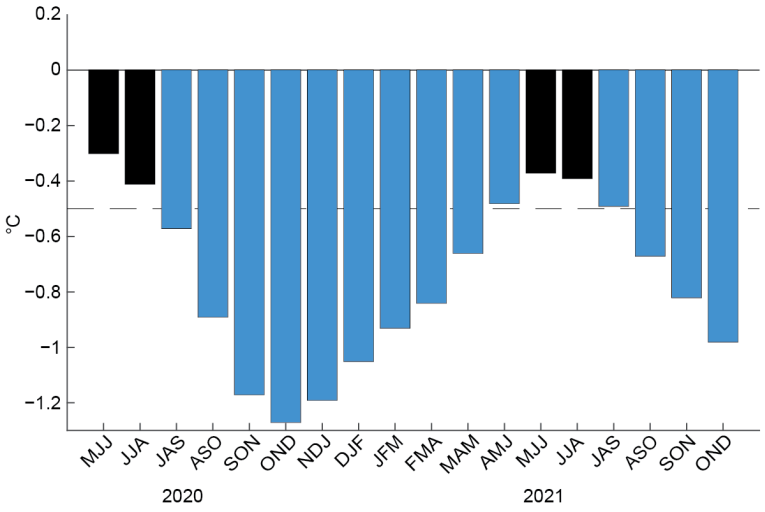

Fig. 4.1. Time series of the Oceanic Niño Index (ONI; °C) from mid-2020 through 2021. Overlapping 3-month seasons are labeled on the x-axis, with initials indicating the first letter of each month in the season. Blue bars indicate negative values below −0.5°C (dashed line). ONI values are derived from the ERSSTv5 dataset and are based on departures from the 1991–2020 period monthly means (Huang et al. 2017).

1) OCEANIC CONDITIONS

Figure 4.2 displays the mean SST (left column) and SST anomalies (right column) during December–February (DJF) 2020/21 through September–November (SON) 2021. SST anomalies on the equator during DJF (Fig. 4.2b) were less than −1.0°C in the central Pacific between 160°E and 140°W. Associated with this cooling, the western Pacific warm pool contracted westward, with the 30°C isotherm only extending to about 160°E (Fig. 4.2b). The east-central and eastern equatorial Pacific SSTs were also below average during DJF, but less so than SST anomalies in the central Pacific, remaining between −1.0°C and −0.5°C. Conversely, SSTs were above average in the western equatorial Pacific and portions of the western subtropical Pacific of both hemispheres. The resulting horseshoe-shaped anomaly pattern is typical of La Niña.

During MAM, La Niña weakened (ONI of −0.6°C) as the central Pacific returned to near-average and the largest SST departures shifted into the eastern part of the Pacific (Fig. 4.2c). By JJA (Fig. 4.2e), the entire tropical Pacific returned to average with NOAA's CPC officially declaring the

[2] The ONI is an index measuring a climate phenomenon, ENSO, and for that reason, the base period is updated every five years with a rolling 30-year climatology. SSTs in the Niño-3.4 region have a positive trend going back to 1950 or earlier, and the rolling climatology is partially used to remove those SST trends and focus on the state of ENSO.

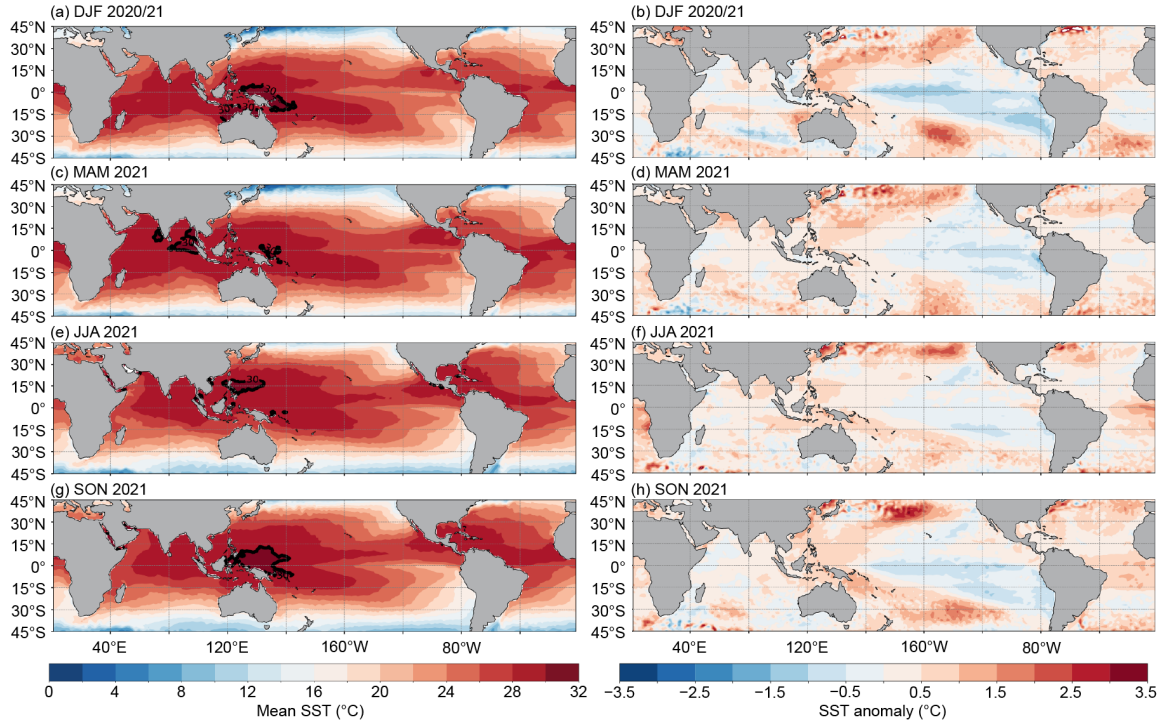

Fig. 4.2. Mean SST (left) and SST anomaly (right) for (a, b) DJF 2020/21, (c, d) MAM 2021, (e, f) JJA 2021, and (g, h) SON 2021. The bold contour for total SST is located at 30°C. Anomalies are departures from the 1991–2020 seasonal adjusted OISST climatology (Huang et al. 2020).

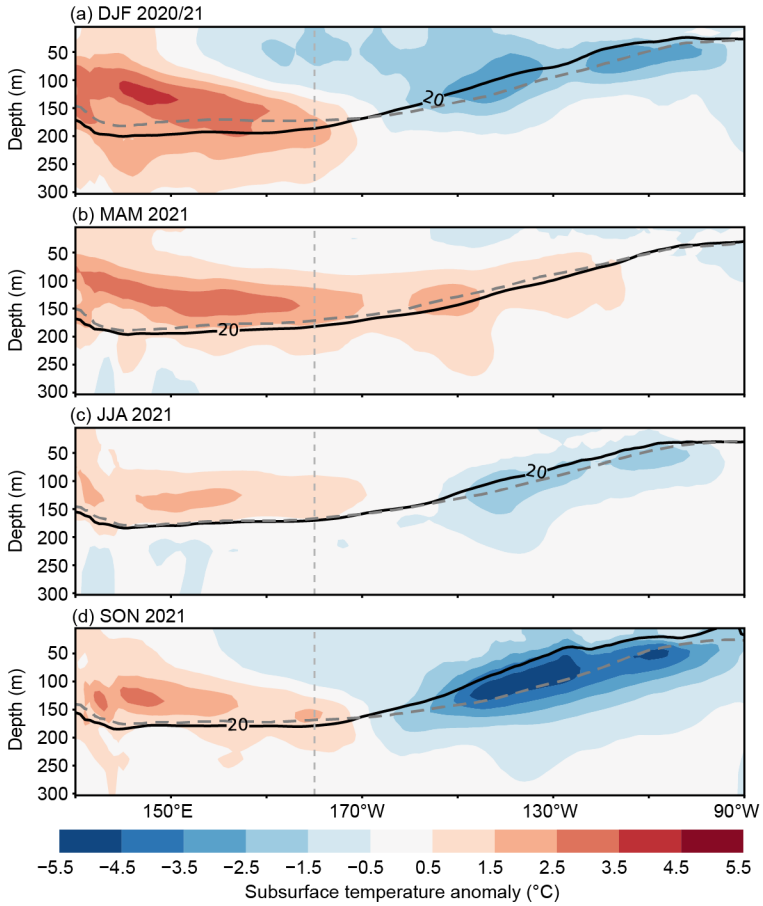

end of La Niña in May. After a brief period of ENSO-neutral conditions, the tropical Pacific again cooled, with SST anomalies generally between –0.5°C and –1.0°C observed during SON (Fig. 4.2g), and NOAA's CPC declaring La Niña had returned in October. The equatorial cold tongue strengthened and expanded westward in association with the renewed development of La Niña (Fig. 4.2h).

Consistent with the above evolution, the subsurface temperature anomaly structure varied considerably during the year (Fig. 4.3). Subsurface temperatures during DJF 2020/21 were below average in the central and eastern equatorial Pacific Ocean and above average in the western and central Pacific, mostly at ocean depths of 100–200 m (Fig. 4.3a). This overall anomaly pattern is typical of La Niña with

Fig. 4.3. Equatorial depth–longitude section of Pacific Ocean temperature anomalies (°C) averaged between 5°S and 5°N during (a) DJF 2020/21, (b) MAM 2021, (c) JJA 2021, and (d) SON 2021. The 20°C isotherm (thick solid line) approximates the center of the oceanic thermocline. The gray dashed line shows the climatology of the 20°C isotherm based on 1991–2020. The data are derived from a reanalysis system that assimilates oceanic observations into an oceanic general circulation model (Behringer 2007). Anomalies are departures from the 1991–2020 period monthly means.

the thermocline shallower than average in the eastern Pacific and deeper than normal in the western Pacific.

During MAM 2021, subsurface temperatures returned to near-average in the eastern half of the equatorial Pacific, and the area of above-average temperatures expanded eastward into the central and east-central Pacific (Fig. 4.3b). This evolution reflected the transition to ENSO-neutral conditions that began in AMJ, partly in association with the downwelling phase of an equatorial oceanic Kelvin wave (see section 4c). During JJA 2021, below average subsurface temperatures returned to the east-central and eastern Pacific (Fig. 4.3c). By SON, the subsurface temperature pattern again reflected an increased east–west thermocline gradient more reminiscent of conditions seen during DJF 2020/21, heralding the return of La Niña (Fig. 4.3d).

2) ATMOSPHERIC CIRCULATION

Although SSTs and sub-surface temperatures in the equatorial Pacific returned to near-average during the boreal summer, many aspects of the tropical atmospheric circulation at least weakly retained their La Niña characteristics. As a result, the low-level 850-hPa trade or easterly winds in the western and central equatorial Pacific (west of 150°W) were generally enhanced throughout the year (Fig. 4.4). Additionally, westerly wind anomalies generally prevailed at 200 hPa throughout the year across the central equatorial Pacific, as did a cyclonic circulation couplet straddling the equator in the central Pacific of the subtropics of both hemispheres, particularly during DJF and MAM (Fig. 4.5). These conditions were associated with below-average precipitation (positive OLR anomalies, brown shading in Fig. 4.6) in the western and central Pacific during all seasons. Collectively, they reflected well-known La Niña-related features, such as an enhanced equatorial Walker circulation and a suppressed Hadley circulation over the central Pacific.

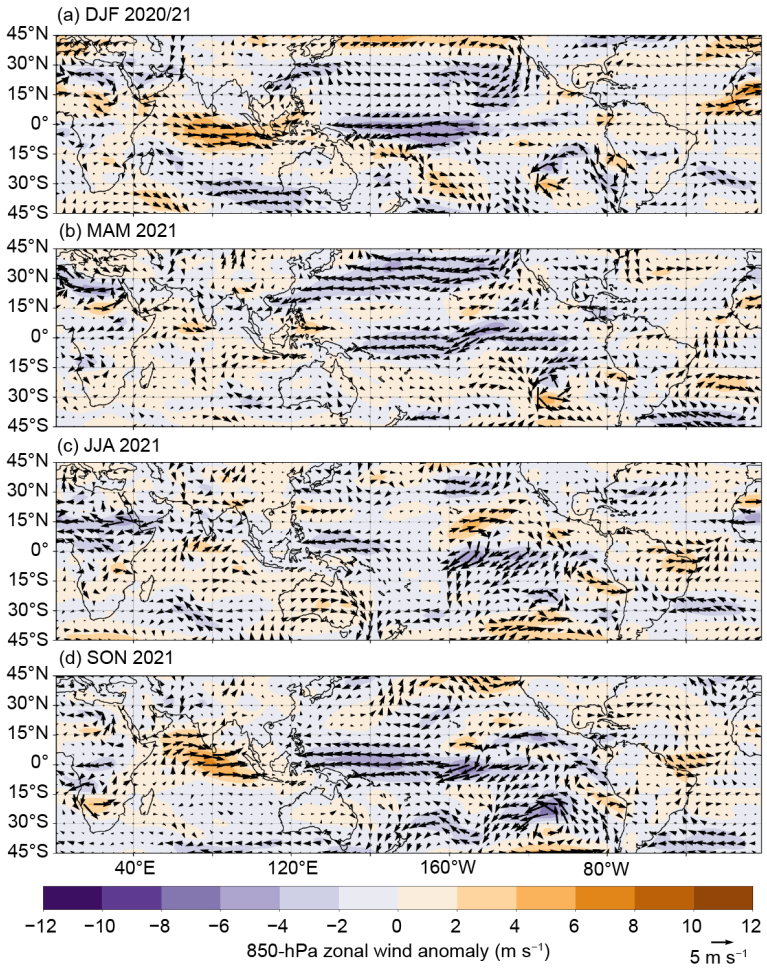

Fig. 4.4. Anomalous 850-hPa wind vectors (arrows) and zonal wind speed (m s^{-1}) during (a) DJF 2020/21, (b) MAM 2021, (c) JJA 2021, and (d) SON 2021. The reference wind vector (m s^{-1}) is located on the bottom left. Anomalies are departures from the 1991–2020 period monthly means. Data are from the NCEP/NCAR Reanalysis (Kalnay et al. 1996).

While the large-scale tropical atmospheric circulation was mainly consistent with La Niña throughout the year, there were some notable circulation differences among the seasons. The pattern of enhanced convection over Indonesia (green shading) and suppressed convection over the west-central equatorial Pacific was strongest as mature La Niña conditions developed during DJF (Fig. 4.6a) and again during SON when La Niña redeveloped and strengthened (Fig. 4.6d). The region of suppressed convection near the date line was weakest during the middle of the year (Figs. 4.6b,c), while the enhanced convection near Indonesia weakened in MAM (Fig. 4.6b), before strengthening again in JJA (Fig. 4.6c) and especially during SON (Fig. 4.6d).

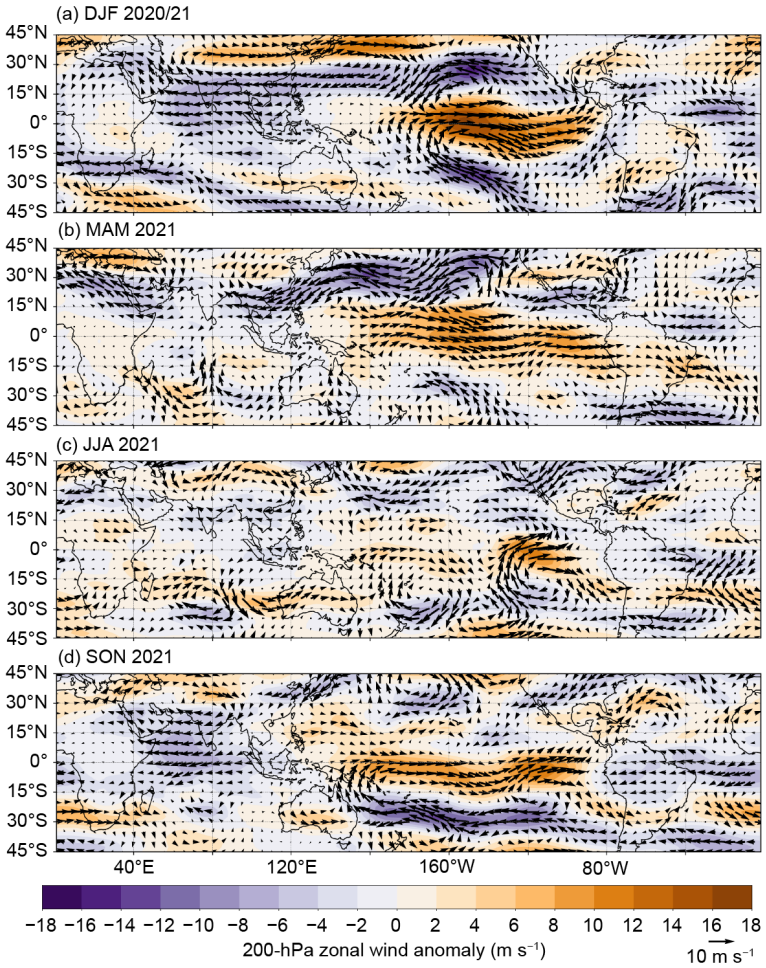

Fig. 4.5. Anomalous 200-hPa wind vectors (arrows) and zonal wind speed (m s^{-1}) during (a) DJF 2020/21, (b) MAM 2021, (c) JJA 2021, and (d) SON 2021. The reference wind vector (m s^{-1}) is located on the bottom right. Anomalies are departures from the 1991–2020 period monthly means. Data are from the NCEP/NCAR Reanalysis (Kalnay et al. 1996).

Consistent with the declining strength of the convective anomalies through the middle of the year, the anomalous 850-hPa equatorial easterlies and anomalous 200-hPa equatorial westerlies over the tropical Pacific were also strongest during DJF (Figs. 4.4a, 4.5a) and SON (Figs. 4.4d, 4.5d). This pattern of winds also persisted during MAM (Figs. 4.4b, 4.5b), before weakening during JJA (Figs. 4.4c, 4.5c). The anomalous cyclonic circulation anomalies in the subtropics of both hemispheres, located just to the east of suppressed convection, were prominent during DJF and MAM. These anomalies were weaker and located farther east during JJA, and then only in the Southern Hemisphere during SON, also farther west, closer to the date line.

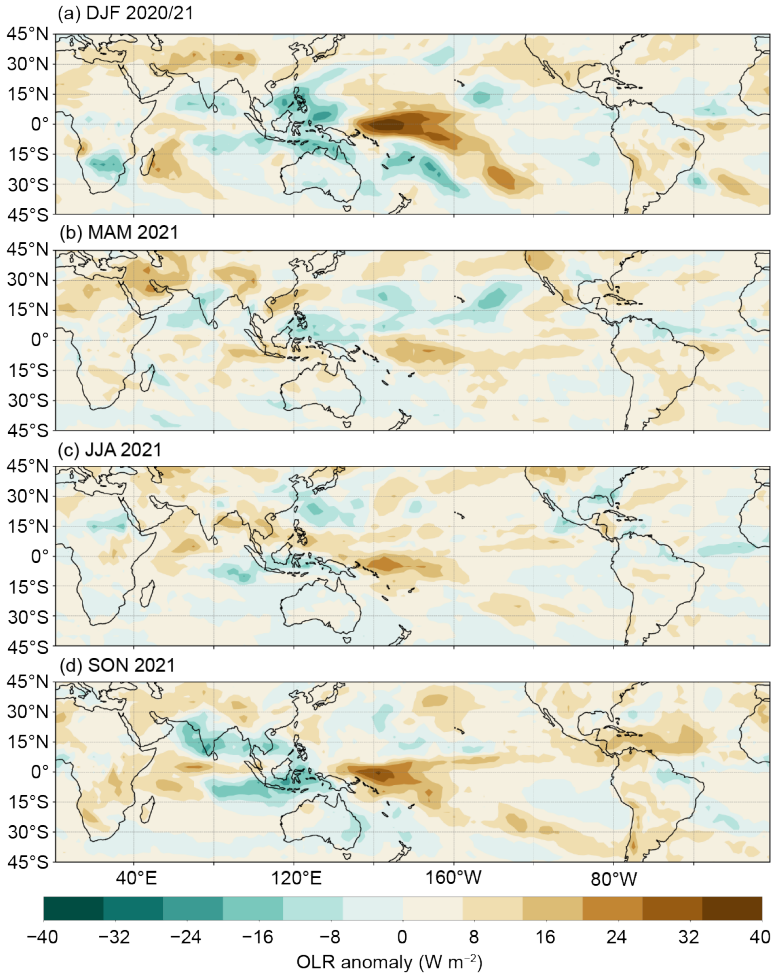

Fig. 4.6. Outgoing longwave radiation (OLR) anomalies (shaded, W m^{-2}), during (a) DJF 2020/21, (b) MAM 2021, (c) JJA 2021, and (d) SON 2021. Anomalies are departures from the 1991–2020 period monthly means. Data are from the NCEP/NCAR Reanalysis (Kalnay et al. 1996).

3) GLOBAL PRECIPITATION LINKS

During DJF 2020/21 (Appendix Fig. 4.1a), precipitation patterns typically associated with La Niña (Ropelewski and Halpert 1989) were observed over many parts of the world. These included below-average precipitation over the tropical central Pacific Ocean, much of the southern tier of the contiguous United States, and southeastern South America. With the development of La Niña during the latter part of the year, many of these impacts also became re-established (Appendix Fig. 4.1b). Impacts during both DJF and SON also included above-average precipitation over northern and eastern Australia, northern South America, Indonesia, the Philippines, and Southeast Asia. During SON (Appendix Fig. 4.1b), above-average precipitation was also observed over India, indicating an enhanced end to their monsoon season.

c. Tropical intraseasonal activity—A. Allgood and C. J. Schreck

Tropical intraseasonal activity is primarily modulated by several different modes of coherent atmospheric variability, most notably the Madden-Julian oscillation (MJO; Madden and Julian 1971, 1972, 1994; Zhang 2005). The MJO is characterized by eastward propagating envelopes of large-scale enhanced and suppressed convection that typically circumnavigate the globe in a 30–60-day period. MJO-related convective anomalies are similar in spatial extent to those generated by the atmospheric response to ENSO, but the latter signal does not propagate around the world. Other impactful modes of variability include convectively coupled waves, such as atmospheric Kelvin waves and westward propagating equatorial Rossby waves (Wheeler and

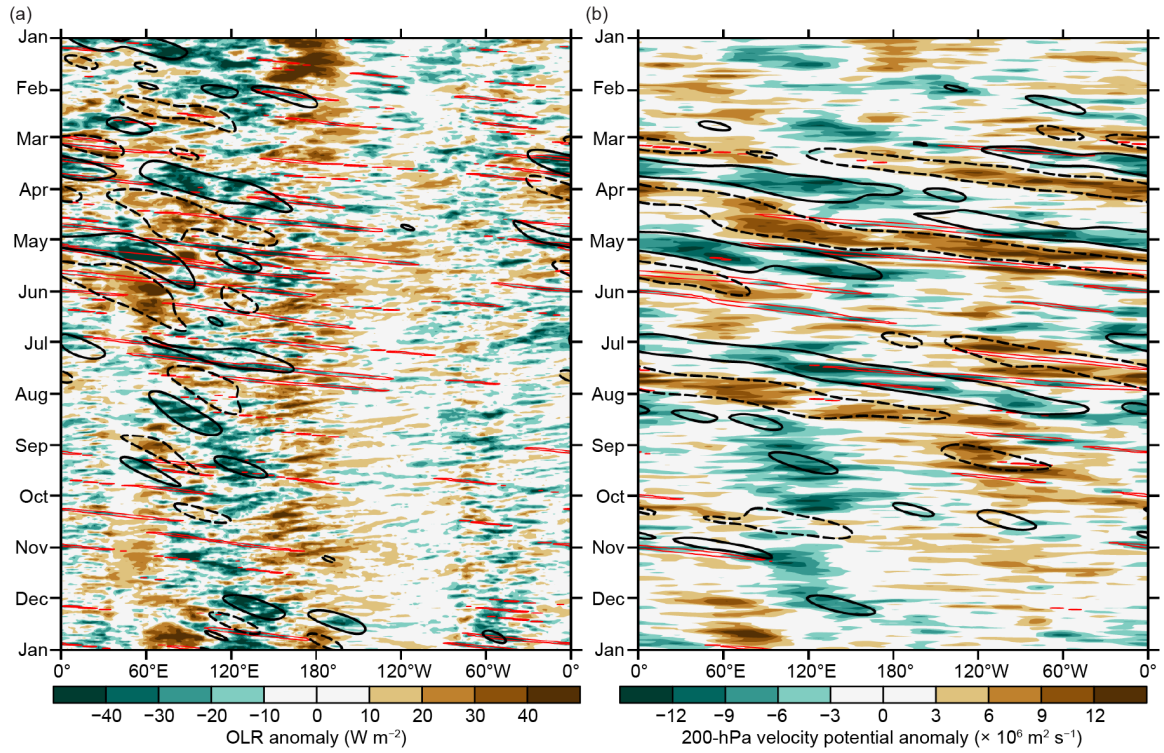

Fig. 4.7. Time–longitude section with (a) OLR anomalies (W m^{-2}; Schreck et al. 2018) and (b) 200-hPa velocity potential anomalies (× 10^6 m^2 s^{-1}) from the CFSR (Saha et al. 2014). Both variables are averaged 10°S–10°N. Time increases downward on this graph, beginning with Jan 2021 at the top and ending with Jan 2022 at the bottom. Negative anomalies indicate enhanced convection, and positive anomalies indicate suppressed convection. Contours identify anomalies filtered for the MJO (black) and atmospheric Kelvin waves (red, negative only). Contours are drawn at ±12 W m^{-2} and ±4 × 10^6 m^2 s^{-1} with the enhanced (suppressed) convective phase of these phenomena indicated by solid (dashed, MJO only) contours. Anomalies are departures from the 1991–2020 base period daily means.

Kiladis 1999; Kiladis et al. 2009). These waves are typically shorter and propagate faster than the MJO. Therefore, the MJO typically generates the strongest extratropical responses (Knutson and Weickmann 1987; Kiladis and Weickmann 1992; Mo and Kousky 1993; Kousky and Kayano 1994; Kayano and Kousky 1999; Cassou 2008; Lin et al. 2009; Riddle et al. 2012; Schreck et al. 2013; Baxter et al. 2014), and plays a role in modulating both monsoonal activity (Krishnamurti and Subrahmanyam 1982; Lau and Waliser 2012) and tropical cyclone activity (Mo 2000; Frank and Roundy 2006; Camargo et al. 2009; Schreck et al. 2012; Diamond and Renwick 2015).

MJO activity can exhibit sustained periods of robust activity, as well as periods of weak or indiscernible activity (Matthews 2008). This activity can be diagnosed through time–longitude analyses of various atmospheric fields, including anomalous outgoing longwave radiation (OLR, Fig. 4.7a) and 200-hPa velocity potential. OLR can be used as a proxy for convective anomalies due to the strong connection between OLR and high cloud cover. Velocity potential identifies the large-scale divergent circulations. MJO activity appears on these diagrams as coherent anomaly couplets that propagate eastward from the upper left towards the lower right. Computerized filtering on these analyses identifies this MJO activity, with enhanced convective activity represented by solid black contours and suppressed activity represented by dashed black contours. Another diagnostic tool frequently used to identify MJO activity is the Wheeler-Hendon (2004) Real-time Multivariate MJO (RMM) index. In RMM plots, robust atmospheric anomalies on a spatial scale resembling the MJO appear as a signal outside of the unit circle, and eastward propagation is represented by counterclockwise looping of the index about the origin (Fig. 4.8).

MJO activity was weak during early 2021, which is fairly typical when La Niña conditions are present. La Niña produces destructive interference with the MJO's enhanced convective envelope over the equatorial Pacific and the suppressed envelope over the Maritime Continent

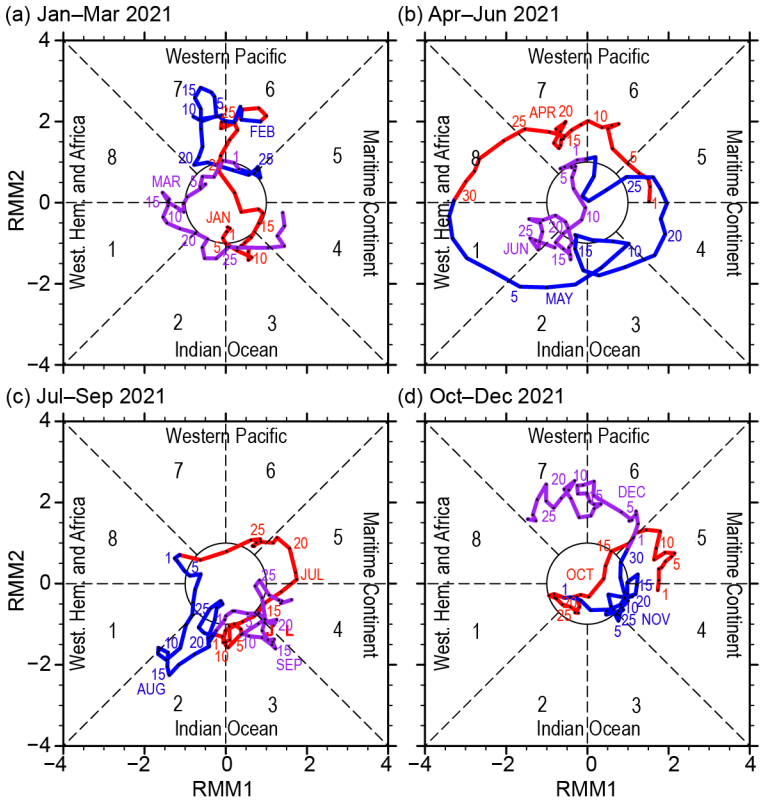

Fig. 4.8. Wheeler and Hendon (2004) Real-time Multivariate MJO (RMM) index for (a) Jan–Mar, (b) Apr–Jun, (c) Jul–Sep, and (d) Oct–Dec 2021. Each point represents the MJO amplitude and location on a given day, and the connecting lines illustrate its propagation. Amplitude is indicated by distance from the origin, with points inside the circle representing weak or no MJO activity. The eight phases around the origin identify the region experiencing enhanced convection, and counter-clockwise movement is consistent with eastward propagation.

(Hendon et al. 1999; Zhang and Gottschalck 2002; Zhang 2005). SST anomalies were below average across the equatorial Pacific during the first few months of 2021 (see Fig. 4.2). A sustained period of MJO activity began in March, lasting through mid-May (Figs. 4.7, 4.8). The enhanced convective phase of the MJO crossed the Pacific during April, weakening the enhanced trade wind regime (Fig. 4.9a) and coincided with the weakening of La Niña conditions observed at that time. After circumnavigating the globe and returning to the Indian Ocean during early May, the MJO weakened over the Pacific by the end of the month, with higher frequency modes such as Kelvin waves becoming the dominant features during June (Fig. 4.7b, red contours).

A second period of MJO activity initiated in July, with the enhanced phase crossing the Western Hemisphere and returning to the Indian Ocean during August. This intraseasonal activity very possibly contributed to the beginning of a hyperactive period of tropical cyclone development over the Atlantic basin during the second half of August and September (see section 4g2).

During October, MJO activity became less discernible as low frequency climate anomalies associated with the redevelopment of La Niña conditions became increasingly dominant and destructively interfered with the MJO enhanced convective envelope over the Pacific during the latter half of October. The atmospheric response to the increased negative SST anomalies across the equatorial Pacific was evident as stationary envelopes of anomalous ascent (negative OLR and 200-hPa velocity potential anomalies) centered near 120°E and descent (positive OLR and 200-hPa velocity potential anomalies) near or east of the date line (Fig. 4.7). Developing La Niña conditions remained the dominant driver of anomalous tropical convection in November. However, a third period of MJO activity initiated in December, with the enhanced phase propagating to the Pacific, generating a fairly substantial low-level westerly wind burst over the West Pacific. This westerly wind burst generated a downwelling oceanic Kelvin wave in the Pacific (Fig. 4.9b).

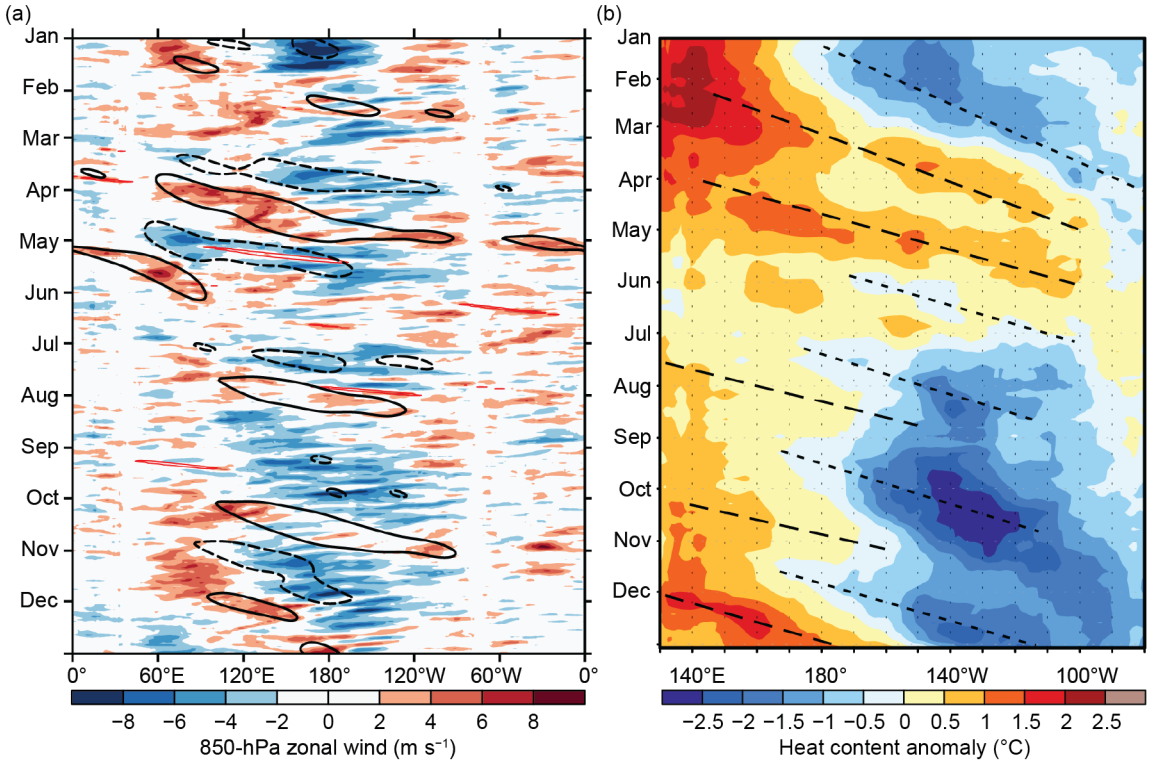

Fig. 4.9. (a) Time–longitude section for 2021 of anomalous 850-hPa zonal wind (m s^{-1}) averaged between 10°N and 10°S. Contours identify anomalies filtered for the MJO. (b) Time–longitude section for 2021 of anomalous equatorial Pacific Ocean heat content (°C), calculated as the mean temperature anomaly between 0 and 300-m depth. Yellow/red (blue) shading indicates above- (below-) average heat content. Relative warming (dashed lines) and cooling (dotted lines) due to downwelling and upwelling equatorial oceanic Kelvin waves are indicated. Anomalies are departures from the 1991–2020 base period pentad means. Data in (b) are derived from an analysis system that assimilates oceanic observations into an oceanic general circulation model (Behringer et al. 1998).

d. Intertropical convergence zones

1) PACIFIC—N. Fauchereau

Tropical Pacific rainfall patterns are dominated by two convergence zones: the Intertropical Convergence Zone (ITCZ; Schneider et al. 2014) north of the equator, and the South Pacific Convergence Zone (SPCZ; Vincent 1994). Figure 4.10 summarizes the behavior for both convergence zones during 2021 using rainfall from NOAA's Climate Prediction Center (CPC) Merged Analysis of Precipitation (CMAP) dataset (Xie and Arkin 1997). Rainfall transects over 30°S to 20°N are presented for each quarter of the year, averaged across successive 30-degree longitude bands, starting in the western Pacific at 150°E–180°. The 2021 seasonal variation is compared against the longer-term 1991–2020 climatology.

Early in the year, the tropical Pacific was still in a La Niña state, albeit weakened compared to the peak reached in October 2020 (section 4b). The maximum negative SST anomalies were also shifted slightly towards the central Pacific, compared to earlier during the development of the event. The transects for January–March (Fig. 4.10a) for the western and central Pacific (150°E to 150°W, especially 150°E to the date line) show that the SPCZ mean signature was shifted south and west of its climatological position, while rainfall rates within the ITCZ were reduced compared to climatology. This signature is consistent with typical anomalies recorded in the Southern Hemisphere summer during La Niña.

La Niña conditions eased as the year progressed and officially ended in May 2021, marking a return to ENSO-neutral state, although weak negative SST anomalies persisted in the central and eastern tropical Pacific. These anomalies re-intensified starting in October, reaching –2°C towards the end of the year off the coast of South America, in a typical 'canonical' ENSO pattern. Accordingly, rainfall anomalies, especially in the western Pacific (Fig. 4.10d), responded in

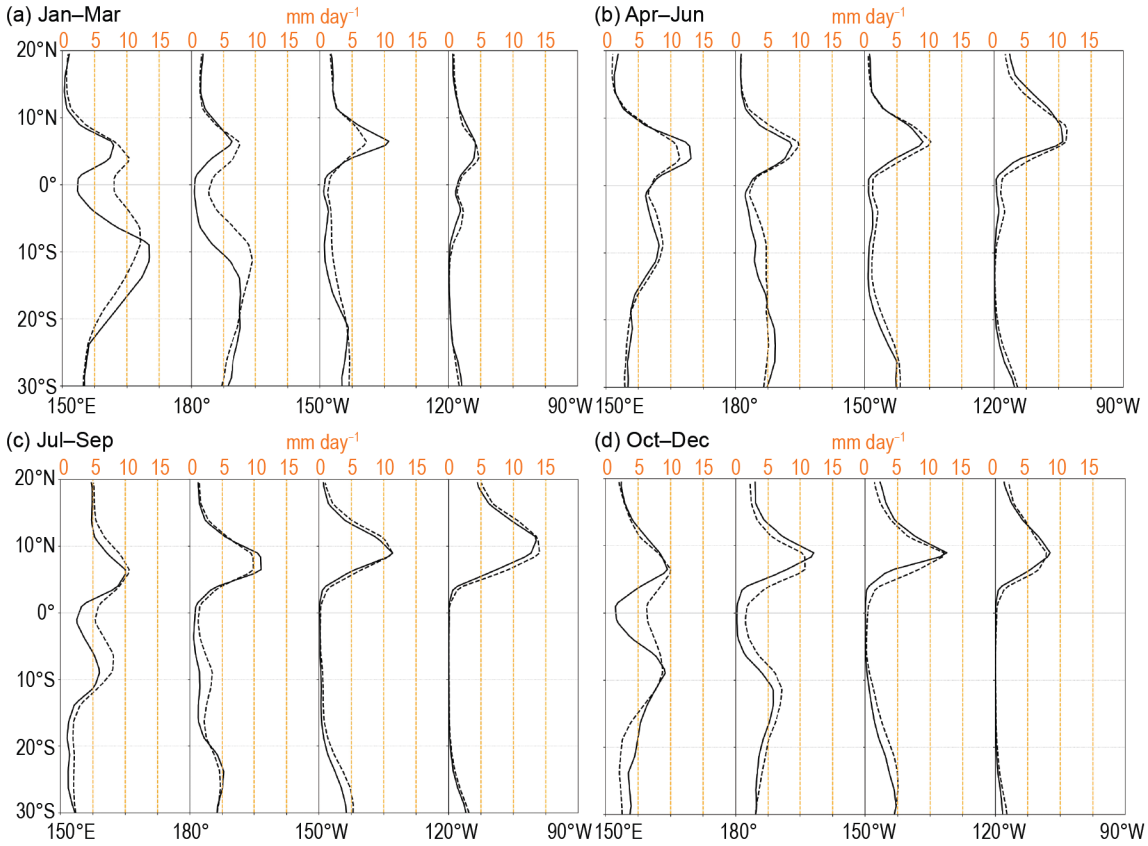

Fig. 4.10. Rainfall rate (mm day^{-1}) from CMAP for (a) Jan–Mar, (b) Apr–Jun, (c) Jul–Sep, and (d) Oct–Dec 2021. The separate panels for each quarter show the 2021 rainfall cross-section between 30°S and 20°N (solid line) and the 1991–2020 climatology (dotted line), separately for four 30° sectors from 150°E–180° to 120°–90°W.

a pattern broadly similar to the one present during the first quarter of the year, with decreased rainfall rates in the equatorial band. Rainfall rates were higher than climatology south of ~10°S.

The most consistent, large, and spatially coherent rainfall anomalies were recorded in the first months of 2021. When averaged over January–March 2021, for example (Fig. 4.11), a large area of below-normal rainfall extended from just north of the Solomon Islands southeast towards French Polynesia, while above-normal precipitation was recorded from Vanuatu to southeast of Fiji, corresponding to a clear southwestward shift in the mean position of the SPCZ. Meanwhile, the ITCZ was suppressed in the western Pacific (Fig. 4.10a) and slightly intensified in the central-eastern Pacific and is consistent with the climatologies as depicted in Figs. 4.10a and 4.11.

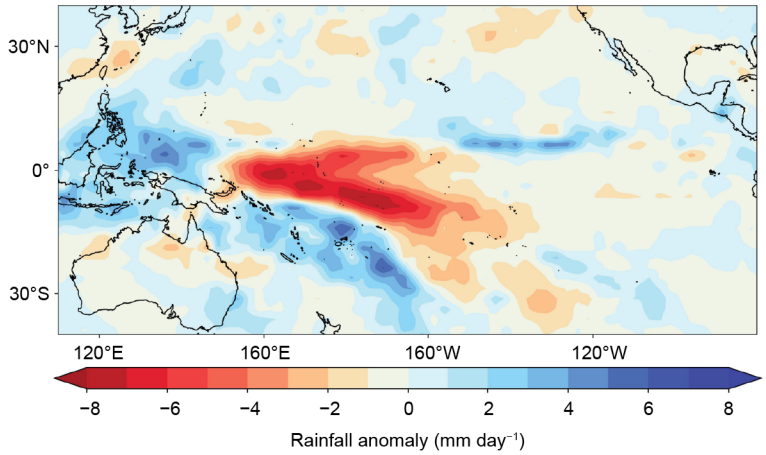

Fig. 4.11. Rainfall anomalies (mm day^{-1}) from CMAP for Jan–Mar 2021. The anomalies are calculated with respect to the 1991–2020 climatology.

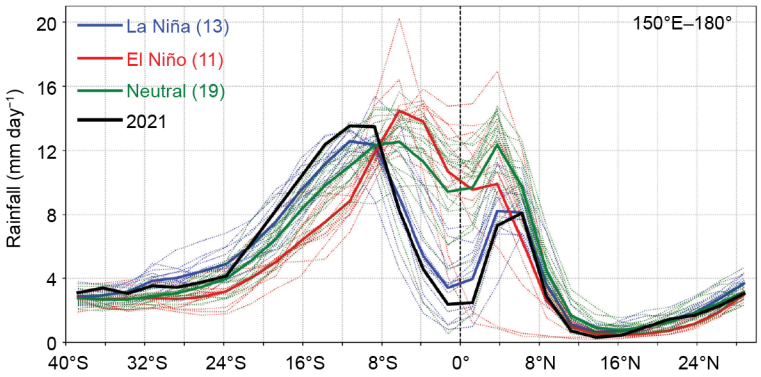

Fig. 4.12. CMAP rainfall rate (mm day^{-1}) for the Jan–Mar quarter, for each year from 1979 to 2021, averaged over the longitude sector 150°E–180°. The cross-sections are color-coded according to NOAA's ONI (with a threshold of ± 0.5°C), except 2021 which is shown in black. Dotted lines are individual years, and solid lines are the average over all years in each ENSO phase. The inset legend indicates how many years went into each composite.

Figure 4.12 shows a more detailed comparison of the western Pacific (150°E–180°) CMAP rainfall transect during January–March 2021, corresponding to the period where La Niña conditions were clearly established, relative to all other years in this dataset. It shows a clear La Niña signal, with the mean anomalies during these three months (black line) closely following the average of La Niña seasons (blue line).

2) ATLANTIC—A. B. Pezza and C. A. S. Coelho

The Atlantic ITCZ is a well-organized convective band that oscillates between approximately 5°–12°N during July–November and 5°S–5°N during January–May (Waliser and Gautier 1993; Nobre and Shukla 1996). Equatorial atmospheric Kelvin waves can modulate ITCZ intraseasonal variability (Guo et al. 2014). ENSO and the Southern Annular Mode (SAM) can also influence the ITCZ on interannual time scales (Münnich and Neelin 2005). The SAM, also known as the Antarctic Oscillation (AAO), describes the north–south movement of the westerly wind belt that circles Antarctica. A negative SAM event reflects an expansion of the westerly wind belt towards the equator, with more abundant precipitation at midlatitudes in general (Ding et al. 2012; Liu et al. 2021; Moreno et al. 2018).

As in 2020, a highlight of the year was a strongly positive SAM pattern (see section 2e), with vigorous low-pressure anomalies around Antarctica and a weaker South Atlantic subtropical anticyclone (Fig. 4.13a). A La Niña pattern and near-neutral equatorial Atlantic Ocean (Fig. 4.13b) temperatures dominated most of the year. Albeit mostly neutral for the yearly average, the Atlantic SST anomalies north of the equator were slightly above normal at the start of 2021, with

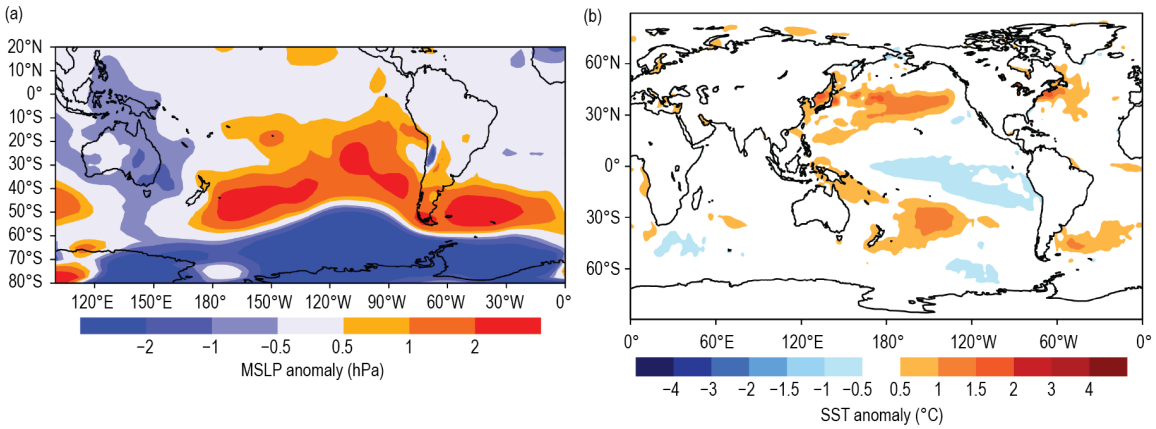

Fig. 4.13. Observed (a) South American and Southern Hemisphere high latitude MSLP anomalies (hPa) and (b) global SST anomalies (°C) for Jan–Dec 2021. MSLP anomalies are calculated with respect to a 1991–2020 climatology derived from the NCEP/NCAR Reanalysis (Kalnay et al. 1996).

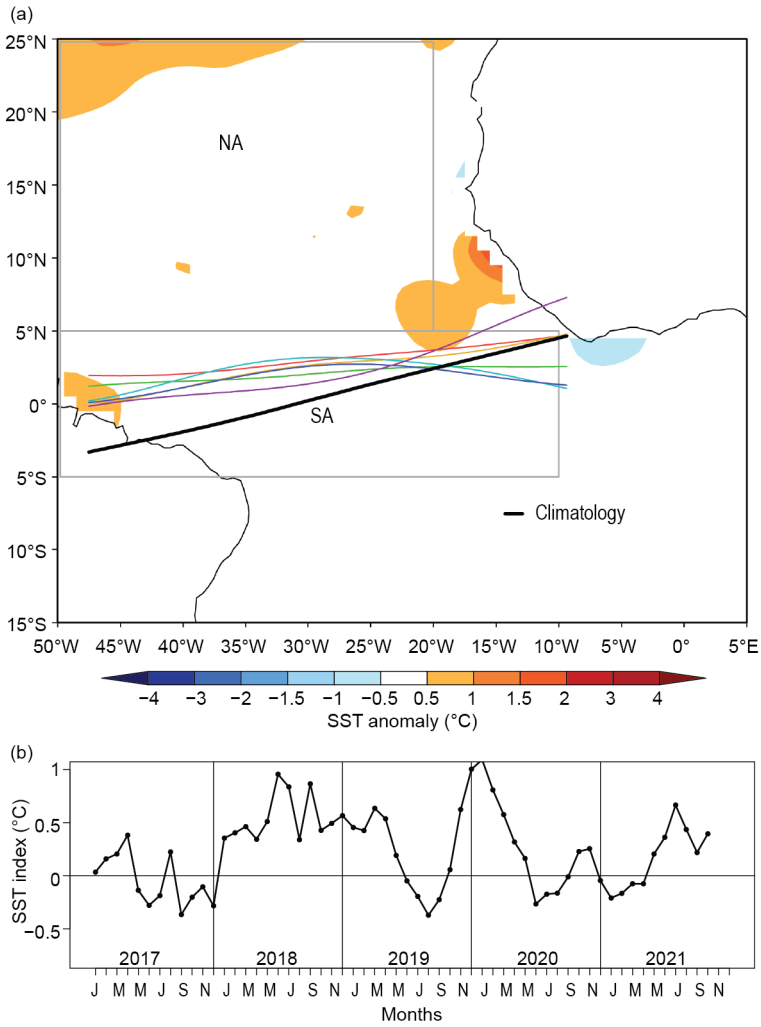

Fig. 4.14. (a) Atlantic ITCZ position inferred from OLR (Liebmann and Smith 1996) during Mar 2021. The colored thin lines indicate the approximate position for the six pentads of the month. The black thick line indicates the Atlantic ITCZ climatological position for Mar. The SST anomalies (°C) for Mar 2021 calculated, with respect to the 1982–2020 climatology, are shaded. The two boxes indicate the areas used for the calculation of the Atlantic index in (b), which shows the monthly OISST (Smith et al. 2008) anomaly time series averaged over the South Atlantic sector (SA region, 5°S–5°N, 10°–50°W) minus the SST anomaly time series averaged over the North Atlantic sector (NA region, 5°–25°N, 20°–50°W) for the period 2017–21, forming the Atlantic index. The positive phase of the index indicates favorable conditions for enhanced Atlantic ITCZ activity south of the equator.

the warm band moving southward in the second half of the year. As expected, the ITCZ and the Atlantic Index (see Fig. 4.14 for definition) followed suit, staying over the area of positive SST anomalies, with associated low-level wind convergence north of the equator at the start of the year (Fig. 4.14a), before shifting south from around May onward (Fig. 4.14b). A large portion of inland Brazil experienced severe precipitation deficits, especially during the first half of the year when the ITCZ stayed north of its climatological position, during the negative phase of the index (Fig. 4.14b). Compared to 2020 (Pezza and Coelho 2021), less anomalous activity in the equatorial Atlantic in 2021 coincided with a greater dominance of the positive SAM pattern encircling the Southern Hemisphere (Fig. 4.13a), with strong pressure anomalies concentrated over mid and high latitudes. Liu et al. (2021) found that the SAM modulates the Walker circulation, which may have contributed to the southern shift of the Atlantic ITCZ.

e. Global monsoon summary—B. Wang and Q. He

Globally, monsoon activity is the dominant mode of annual precipitation and circulation variability and one of the defining features of Earth's climate system. Here, we summarize the global and regional monsoon precipitation anomalies in the 2021 monsoon year, which includes the Southern Hemisphere (SH) summer (November 2020–April 2021) and Northern Hemisphere (NH) summer (May 2021–October 2021) monsoons. Figure 4.15 presents the monsoon domain (red lines) defined by rainfall characteristics (rainy summer versus dry winter; Wang 1994) rather than the traditional definition by winds (Ramage 1971). Two criteria define the monsoon domain: (1) the annual precipitation range (hemispheric summer minus hemispheric winter) exceeds 300 mm and (2) the hemispheric summer precipitation is > 55% of the total annual precipitation amount, where summer here means May–September for the NH and November–March for the SH (Wang and Ding 2008). The NH monsoon includes five regional monsoons: Northern Africa, India, East Asia, the western North Pacific, and North America. The SH monsoon consists of three monsoons: southern Africa, Australia, and South America.

Regional precipitation and circulation indices are used to measure the regional monsoon intensity. The precipitation indices represent the anomalous precipitation rate averaged over the blue rectangular box regions shown in Fig. 4.15. Note that the precipitation averaged in each blue box represents the precipitation averaged over the entire corresponding regional monsoon domain value (r >0.90; Yim et al. 2014). The definitions of the circulation indices for each monsoon region are provided in Table 4.1. They are modified from indices originally depicted by Yim et al. (2014). All circulation indices are defined by the meridional shear of the zonal winds at 850 hPa (or 700 hPa in highland southern Africa), which measures the intensity (relative vorticity) of the monsoon troughs except for the northern African and East Asian monsoons. The northern African monsoon circulation index is defined by the westerly monsoon strength, reflecting the north–south thermal contrast between the South and North Atlantic. The East Asian summer monsoon (EASM) circulation index is determined by the meridional wind strength, reflecting

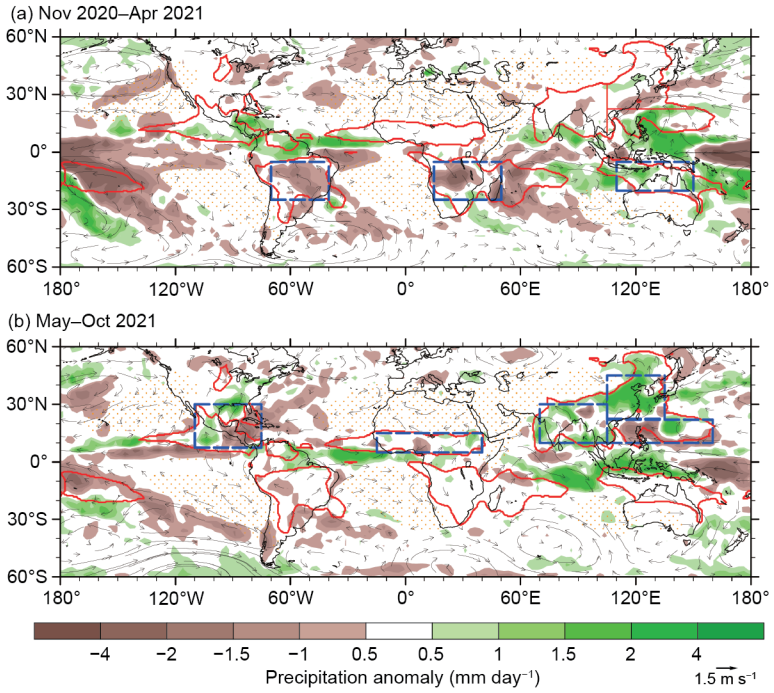

Fig. 4.15. Seasonal mean precipitation anomalies (mm day^{-1}) and 850-hPa wind anomalies (m s^{-1}) for (a) the SH summer monsoon season: Nov 2020–Apr 2021 and (b) the NH summer monsoon season: May–Oct 2021. Climatological mean was made for 1991–2020. Red lines outline the monsoon precipitation domain defined in the text. The dotted area represents the dry region where the local summer precipitation rate is below 1 mm day^{-1}. Rainfall data were taken from the Global Precipitation Climatology Project (GPCP; Huffman et al. 2009).

Table 4.1. Definition of the regional summer monsoon circulation indices and their correlation coefficients (*r*) with the corresponding regional summer monsoon precipitation indices for 1979/80–2020/21. The precipitation indices are defined by the areal mean precipitation over the blue box regions shown in Fig. 4.15. The correlation coefficients were computed using monthly time series (168 summer months; Jun–Sep in NH [1980–2021] and Dec–Mar in SH [1979/80–2020/21]). Bolded numbers represent significance at the 99% confidence level. (Adapted from Yim et al. 2014.)

Regional monsoon	Definition of the circulation index	*r*
Indian (ISM)	U850 (5°–15°N, 40°–80°E) minus U850 (25°–35°N, 70°–90°E)	**0.72**
Western North Pacific (WNPSM)	U850 (5°–15°N, 100°–130°E) minus U850 (20°–35°N, 110°–140°E)	**0.87**
East Asian (EASM)	V850 (20°–35°N, 120°–140°E) plus V850 (10°–25°N, 105°–115°E)	**0.74**
North American (NASM)	U850 (5°–15°N, 130°–100°W) minus U850 (20°–30°N, 110°–80°W)	**0.85**
Northern African (NAFSM)	U850 (0°–10°N, 40°W–10°E)	**0.70**
South American (SASM)	U850 (20°–5°S, 70°–40°W) minus U850 (35°–20°S, 70°–40°W)	**0.82**
Southern African (SAFSM)	U700 (10°S–0°S, 0°–30°E) minus U700 (25°–10°S, 40°–70°E)	**0.46**
Australian (AUSSM)	U850 (15°S–0°, 90°–130°E) minus U850 (30°–20°S, 100°–140°E)	**0.88**

the east–west thermal contrast between the Asian continent and the western North Pacific. The precipitation and circulation indices are well correlated for most regional monsoons, with correlation coefficients ranging from 0.70 to 0.88, except for the southern African monsoon (Table 4.1). Thus, the precipitation and circulation indices generally provide consistent measurements of the strength of each regional monsoon system.

ENSO dominates year-to-year variation of the monsoons (Ropelewski and Halpern 1987). La Niña conditions prevailed during the 2020/21 SH summer from November 2020 to April 2021. During the 2021 NH summer monsoon season, La Niña weakened to ENSO-neutral conditions in June–July (although eastern and central Pacific SSTs were still below average), La Niña re-emerged in August and rapidly cooled in September (section 4b).

During the 2020/21 SH summer, the La Niña-driven anomalous Walker circulation caused suppressed rainfall over the central-western Pacific and increased rainfall over the Maritime Continent. Precipitation in the Australian monsoon region was above normal (Fig. 4.15a). However, precipitation was significantly reduced over the South American and southern African monsoon regions. The Indian Ocean rainfall anomalies were also driven by the negative phase of the Indian Ocean dipole (Saji et al. 1999; section 4f). Figure 4.16 shows areal-averaged monsoon intensities. The Australian summer monsoon precipitation was 0.5 standard deviations (std. dev.) above normal, and the corresponding circulation intensity was 1 std. dev. above average (Fig. 4.16g). The South American monsoon region measured precipitation that was 2 std. dev. below normal, yet the related circulation's strength was less than 0.5 std. dev. below normal (Fig. 4.16h). The southern African summer monsoon precipitation was 2 std. dev. below normal, but the circulation intensity was 1 std. dev. above average (Fig. 4.16f). Overall, the South American and southern African monsoons responded uncharacteristically to the 2020/21 La Niña, although the reasons why are unclear.

During the 2021 NH summer monsoon season (May–October), precipitation over the Maritime Continent was significantly above normal, while there was a noticeable reduction of precipitation in the equatorial western Pacific and near the northern Philippines (Fig. 4.15b).

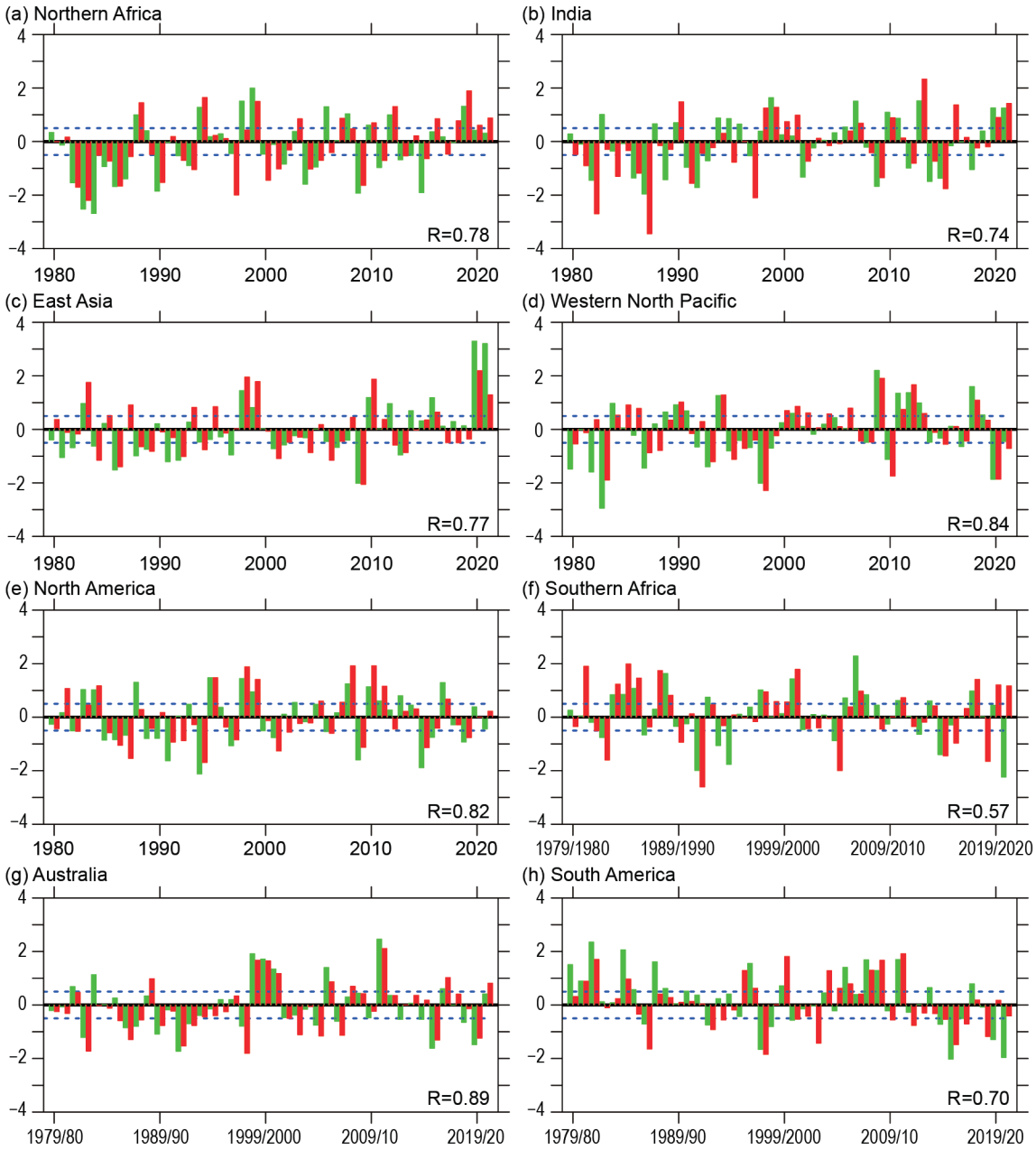

Fig. 4.16. (a–h) Temporal variations of summer monsoon precipitation and low-level circulation indices for eight regional monsoons. Green and red bars show the summer mean precipitation and circulation indices, respectively. All indices were normalized by their corresponding standard deviation with respect to the mean during 1991–2020 (ordinate). Numbers shown in the bottom right of each panel denote the correlation coefficient (R) between the seasonal mean precipitation and circulation indices (sample size: 42). Dashed lines indicate ±0.5 std. dev. The summer monsoon seasons are May–Oct for the NH and Nov–Apr for the SH. (Data source: GPCP for precipitation and ERA5 [Hersbach et al. 2020] for circulation.)

These characteristics resemble a typical precipitation anomaly pattern during a La Niña. While there is a general increase in NH monsoon precipitation, there are notable regional differences. The EASM showed record high precipitation and enhanced southerly monsoon in consecutive seasons in 2020 and 2021, with 2020 a bit greater (Fig. 4.16c). The EASM precipitation anomaly was nearly 3 std. dev. above average, and the corresponding southerly monsoon intensity was 1.2 std. dev. above normal (Fig. 4.16c). The Indian summer monsoon precipitation and circulation indices were both more than 1 std. dev. above normal (Fig. 4.16b). Precipitation over the northern African monsoon region was slightly above average (Fig. 4.16a). The North American monsoon showed average precipitation and circulation intensity due to a dipole pattern in the area (Fig. 4.16e). The western North Pacific oceanic monsoon precipitation, generally out of phase with the EASM, was 0.5 std. dev. below normal (Fig. 4.16d).

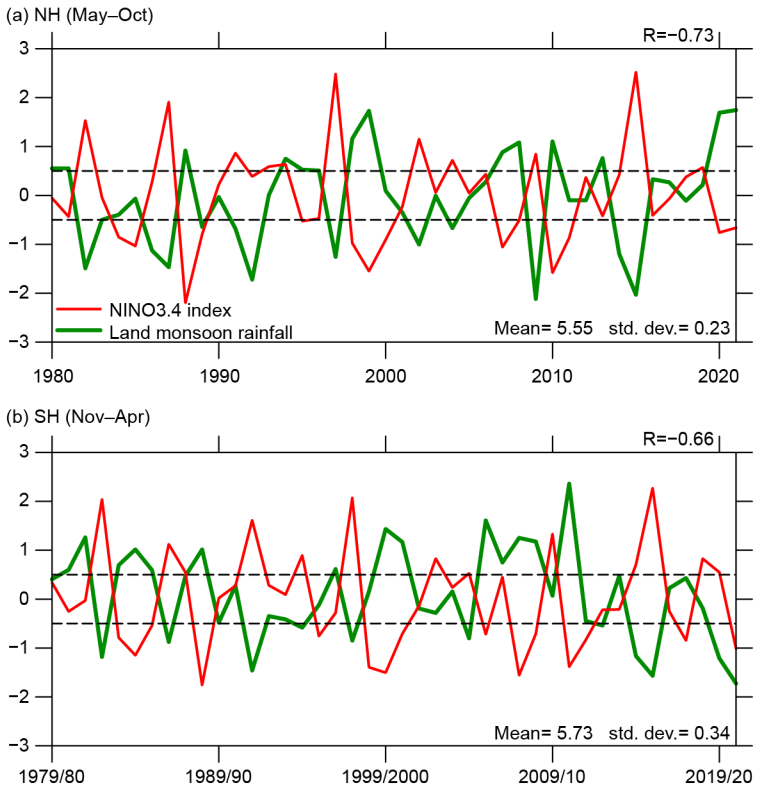

Fig. 4.17. (a) NH summer (May–Oct) land monsoon precipitation anomaly (green) normalized by its standard deviation. The climatological mean NH summer land monsoon precipitation during 1991–2020 (mean) and standard deviation (std. dev.) are shown in the lower right panel (mm day^{-1}). Numbers shown in each panel's top right denote the correlation coefficient (R) between the seasonal mean precipitation anomaly and the simultaneous Niño 3.4 index (red). Dashed lines indicate ±0.5 std. dev. (b) As in (a) except for the SH summer (Nov–Apr). Note that the land monsoon precipitation excludes the monsoon rainfall over the oceanic monsoon domain. (Data source: GPCP for precipitation, HadISST and ERSSTv5 for SST.)

Monsoon rainfall over land has more important socio-economic impacts than oceanic monsoon rainfall. Therefore, we specifically examine land monsoon rainfall (LMR). The NH and SH LMR indices were computed by the average precipitation over the corresponding land areas within the monsoon domain. The LMR on a global scale is strongly influenced by ENSO (Wang et al. 2012). Figure 4.17 shows that both the NH and SH land summer monsoon precipitation are anti-correlated with the simultaneous Niño-3.4 index. This is especially the case for NH land monsoon rainfall which has a simultaneous correlation of −0.73 from 1980 to 2021. Of note, the total amount of 2021 NH land monsoon precipitation was a record high over the past four decades, with the average daily rainfall almost 2 std. dev. higher than normal. Furthermore, the NH land monsoon rainfall was high in both 2020 and 2021 (Fig. 4.17a). This is primarily attributed to nearly consecutive annual record-high East Asian monsoon precipitation that exceeded 3 std. dev. (Fig. 4.16c). The summer precipitation total in northern China was the second highest in the last 40 years just behind 2020 (see section 7g3 for more details).

f. Indian Ocean dipole—L. Chen and J.-J. Luo

The Indian Ocean dipole (IOD), referring to the anomalous SST gradient between the eastern and western equatorial Indian Ocean (IO), is a major interannual mode in the tropical Indian Ocean. It can stem from tropical ENSO forcing and/or local air–sea interaction processes (Saji et al. 1999; Luo et al. 2010, 2012). In general, the IOD starts to develop in boreal summer, peaks in boreal autumn, and decays rapidly in early boreal winter. A positive IOD (pIOD) event usually features cold SST anomalies in the eastern IO and weak warm SST anomalies in the western IO, and vice versa for a negative event. The IOD exhibits nonlinearity, e.g., the magnitude of a

pIOD event is generally stronger than that of a negative IOD (nIOD) event, due to the asymmetric ocean–atmosphere coupling between the two phases of the IOD phenomenon (Luo et al. 2007; Hong et al. 2008).

A nIOD event occurred in the latter half of 2021 (Figs. 4.18, 4.19), marking the first negative event since 2016. The IOD index reached −0.55°C in October–November 2021 (Fig. 4.18b), with significant positive SST anomalies in the eastern pole and small negative SST anomalies in the western pole (Fig. 4.18a). For comparison, the two strongest nIOD events on record in 1998 and 2016 reached −0.97°C and −0.95°C, respectively (Luo 2017).

The nIOD development in 2021 was mainly due to the rapid increase of SST anomalies over the eastern pole of the IOD (hereafter IODE) during January–July 2021 (Fig. 4.18a). Following a neutral IOD in boreal autumn 2020 (Chen and Luo 2021), below-average SSTs and precipitation occurred across the entire equatorial IO during the boreal winter 2020, from the western pole of the IOD (IODW) to the IODE, as seen in Figs. 4.19a and 4.20a. The SST anomalies averaged over IODE were −0.7°C in January 2021 but quickly increased to +0.6°C in July 2021 (Fig. 4.18a). The development of the nIOD-related SST anomalies during the first half of the year is mainly attributed to anomalous westerly winds over the entire equatorial IO region during December 2020–February 2021 (Fig. 4.19a) and anomalous westerly winds over the western equatorial IO region during March–May (Fig. 4.19b).

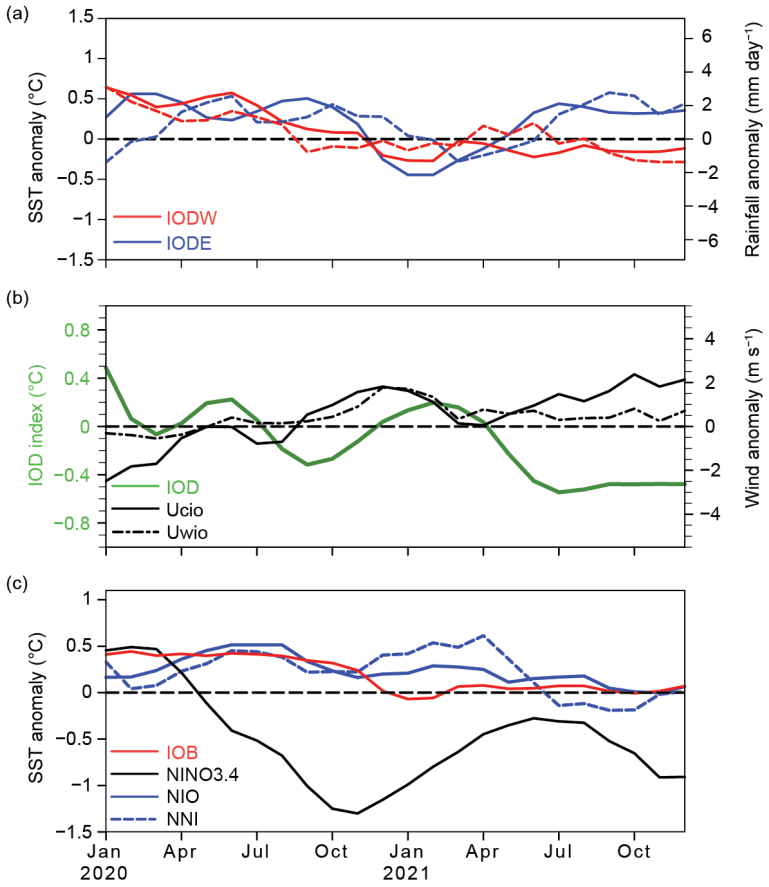

Fig. 4.18. (a) 3-monthly running mean SST anomalies (°C; solid lines) and precipitation (mm day^{-1}; dashed lines) in the eastern pole (IODE; 10°S–0°, 90°–110°E; blue lines) and the western pole (IODW; 10°S–10°N, 50°–70°E; red lines) of the IOD. (b) As in (a), but for the IOD index (measured by the SST difference between IODW and IODE, green line) and surface zonal wind anomaly (m s^{-1}) in the central equatorial IO (Ucio; 5°S–5°N, 70°–90°E; solid black line) and western equatorial IO (Uwio; 5°S–5°N, 50°–70°E; dashed black line). (c) As in (a), but for SST anomalies in the Niño 3.4 region (5°S–5°N, 170°–120°W; black line), the tropical IO (IOB; 20°S–10°N, 40°–120°E; red line), the northern IO (NIO; 5°–20°N, 60°–120°W; solid blue line), and the region off western Australia (22°–28°S, 108°–117°E; dashed blue line). Anomalies are relative to the 1991–2020 base period. (Sources: NOAA OISST [Reynolds et al. 2002]; monthly GPCP precipitation analysis [https://psl.noaa.gov/data/gridded/data.gpcp.html]; and JRA-55 atmospheric reanalysis [Ebita et al. 2011].)

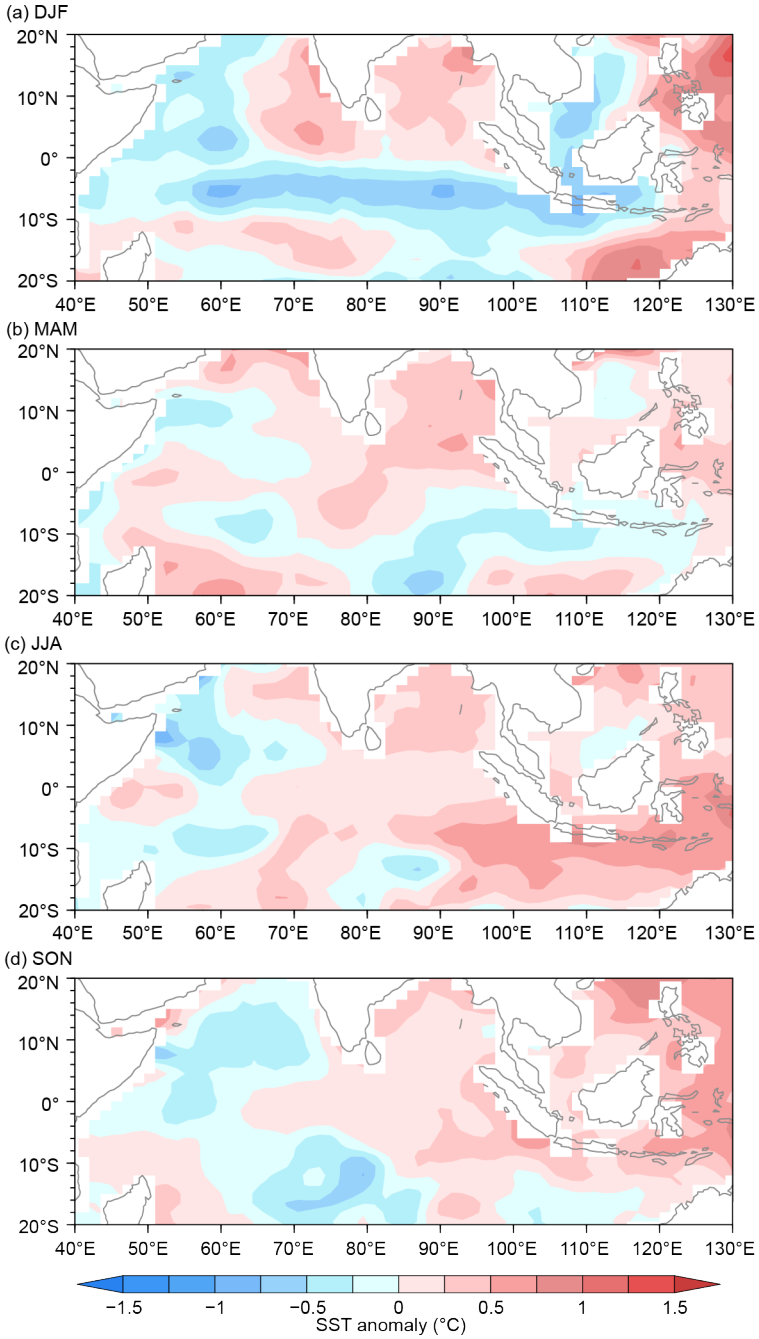

Fig. 4.19. SST anomalies (°C, colored scale) during (a) Dec 2020–Feb 2021, (b) Mar–May 2021, (c) Jun–Aug 2021, and (d) Sep–Nov 2021. Anomalies were calculated relative to the 1991–2020 climatology. (Sources: NOAA OISST [Reynolds et al. 2002].)

The westerly wind anomalies over the equatorial IO region during December 2020–February 2021 were consistent with a Rossby–Kelvin wave response (Matsuno 1966; Gill 1980) to two positive precipitation belts located on both sides of the equator in the IO (Fig. 4.20e). The convection in the northern IO (NIO; including the eastern Arabian Sea and the Bay of Bengal) was due to the above-average SST anomalies in that region (Figs. 4.19a, 4.20a). The anomalous warmth in the southern tropical IO region (5°–20°S, 78°–108°E) was largely attributed to the warm Ningaloo Niño event (a phenomenon featured by above-average SST off the coast of western Australia; Feng et al. 2013), as previous studies (e.g., Zheng et al. 2020) have indicated that the above-average precipitation tends to occur in the northwestern regions of the above-average SST anomalies associated with the Ningaloo Niño.

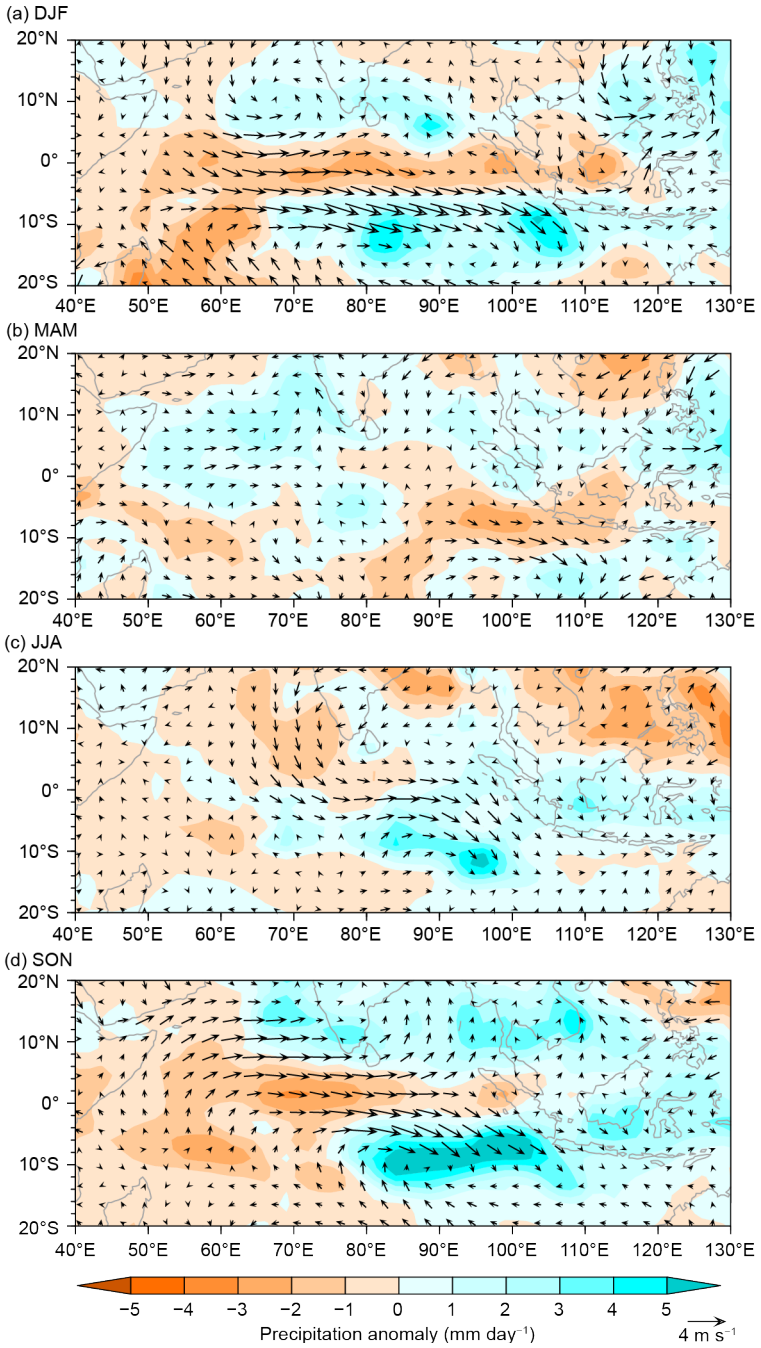

Fig. 4.20. Precipitation (mm day^{-1}) and surface wind (m s^{-1}) anomalies relative to 1991–2020 during (a) Dec 2020–Feb 2021, (b) Mar–May 2021, (c) Jun–Aug 2021, and (d) Sep–Nov 2021. (Sources: monthly GPCP precipitation analysis [https://psl.noaa.gov/data/gridded/data.gpcp.html] and JRA-55 atmospheric reanalysis [Ebita et al. 2011].)

During March–May 2021, the anomalous westerly wind was confined over the western equatorial IO region, arising from above-average precipitation and corresponding above-average SST over the northeastern Arabian Sea (Figs. 4.19b, 4.20b). To summarize, the aforementioned two convective centers induced by the above-average SST over the NIO and the western Australian coast (hereafter subtropical IO regions) contributed to the westerly wind anomalies over the whole IO equator during December 2020–February 2021, and the northern convection continued to trigger westerly wind anomalies over the western equatorial IO during March–May 2021. As a result, the continuous warm Kelvin wave propagated eastward along the IO equator, causing warm SSTs in the IODE during the first half of 2021.

During boreal summer and autumn 2021, the nIOD event continued due to air–sea coupling over the tropical IO. As seen in Figs. 4.19c,d and Figs. 4.20c,d, positive (negative) SST anomalies

in IODE (IODW) are accompanied by positive (negative) precipitation anomalies, along with pronounced westerly wind anomalies over the central equatorial IO. Meanwhile, ENSO-neutral conditions were present in boreal summer 2021 before La Niña re-emerged in boreal autumn (Fig. 4.18c). The rapid growth of the nIOD in the first half of 2021 was largely due to the above-average SSTs and the concurring above-average precipitation over the subtropical IO regions. Additionally, considering the entire IO, only a marginal IO basin-wide warming appeared throughout 2021, despite the multidecadal basin-wide warming over the tropical IO SST (Luo et al. 2012), while a strong IO basin-wide warming persisted throughout 2020 (Chen and Luo 2021).

In summary, a moderate nIOD event occurred in 2021, with the IOD index reaching −0.55°C during boreal autumn. The development of this event was mainly due to the rapid increase of SSTs over the IODE during the first half of 2021, from −0.7°C below average in January to +0.6°C above average in July. It is suggested that the convection induced by the above-average SSTs over the subtropical IO regions caused the westerly wind anomalies over the equatorial IO regions, which led to the positive SST anomalies over IODE. The nIOD event continued due to air–sea interactions during boreal summer and autumn.

g. Tropical cyclones

1) OVERVIEW—H. J. Diamond and C. J. Schreck

The IBTrACS dataset comprises historical tropical cyclone (TC) best-track data from numerous sources around the globe, including all of the World Meteorological Organization (WMO) Regional Specialized Meteorological Centers (RSMCs; Knapp et al. 2010). This dataset represents the most complete compilation of global TC data. From these data, 1991–2020 climatological values of TC activity for each basin using statistics from both the WMO RSMCs and the Joint Typhoon Warning Center (JTWC) are calculated following Schreck et al. (2014). These values are referenced in each subsection. Tallying the global TC numbers is challenging and involves more than simply adding up basin totals, because some storms cross TC basin boundaries, some TC basins overlap, and multiple agencies track and categorize TCs. The Northern Hemisphere (NH) basins are typically measured from January to December while Southern Hemisphere (SH) basins are typically measured from July to June. Global values here are the sum of the Northern Hemisphere for 2021 and the Southern Hemisphere for 2020/21.

Based on preliminary data from NOAA's National Hurricane Center and the JTWC as archived in IBTrACS (Fig. 4.21), the combined 2021 season had 97 named storms (sustained wind speeds ≥ 34 kt or 17 m s^{-1}), which is five fewer than last season (2020; Diamond and Schreck 2020). The 2021 season count had the eighth most named storms on record and is well above the 1991–2020 average of 87. However, there were just 38 hurricanes/typhoons/cyclones (HTCs; sustained wind speeds ≥ 64 kt or 33 m s^{-1}; average 48), and only 17 of those reached major HTC status (sustained wind speeds ≥ 96 kt or 49 m s^{-1}; average 26). Both of these numbers are at least tied for the third fewest on record since 1980. The Accumulated Cyclone Energy (ACE) for the season was 649×10^4 kt^2, which is 10% higher than last year (Diamond and Schreck 2019) but still 17% below the climatological mean.

In sections 4g2–4g8, 2020/21 (SH) and 2021 (NH) seasonal TC activity is described and compared to the historical record for each of the seven WMO-defined TC basins. For simplicity, all counts are broken down by the U.S. Saffir-Simpson Hurricane Wind Scale (SSHWS).[3] The overall picture of global TCs during 2021 is shown in Fig. 4.21, and counts by category are documented in Table 4.2. Similar to 2020, the North Atlantic played an out-sized role in global tropical cyclone activity in 2021. The 21 named storms were the third most on record, behind 2020 (30) and 2005 (28). The seven hurricanes were near normal, the four major hurricanes were above normal, and

[3] SSHWS is based on 1-minute averaged winds, and the categories are defined at: https://www.weather.gov/mfl/saffirsimpson; the Australian category scale is based on 10-minute averaged winds, and those categories are defined at http://www.bom.gov.au/cyclone/tropical-cyclone-knowledge-centre/understanding/tc-info/

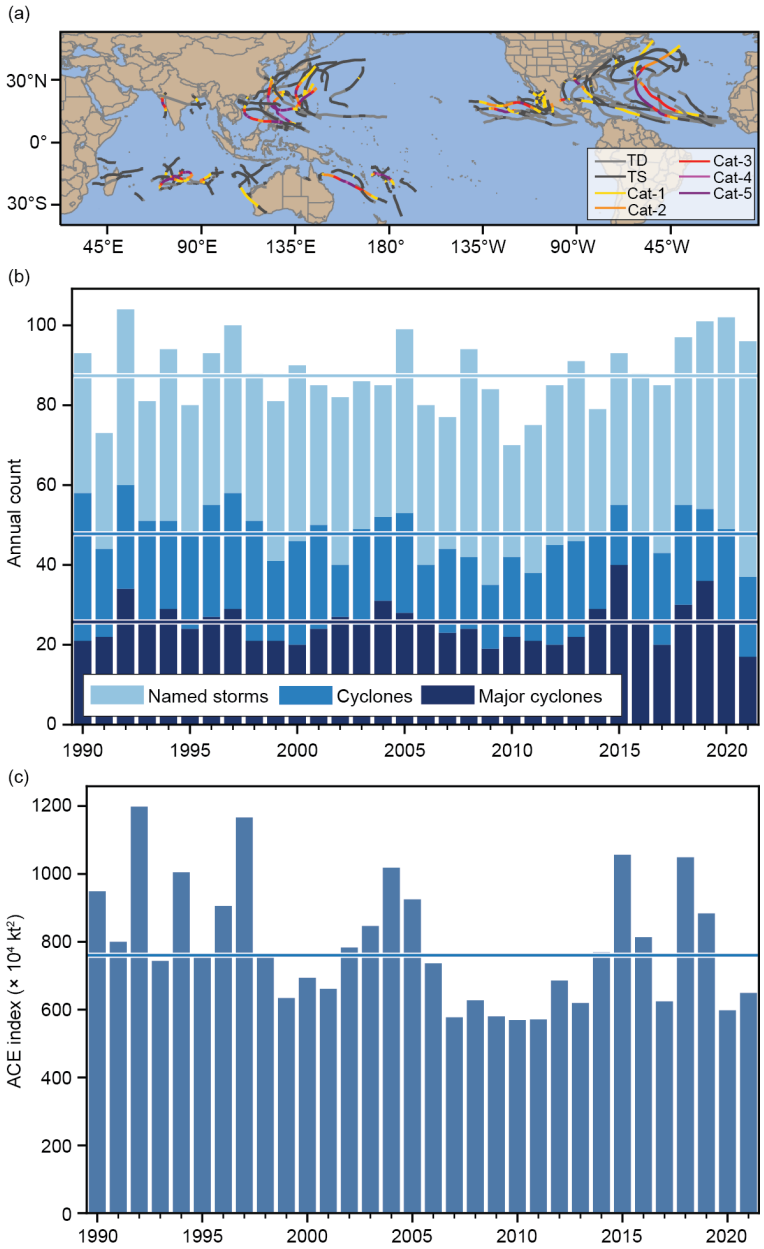

Fig. 4.21. Annual global TC statistics for the period 1990–2021. (a) storm tracks for 2021, (b) number of named storms, cyclones, and major cyclones, and (c) ACE (× 10^4 kt^2). The 1991–2020 means (horizontal lines) are included in both (b) and (c).

the ACE was 149% of the 1951–2020 median. The eastern North Pacific had more named storms than normal, but the ACE was below normal. The western North Pacific was quieter than normal by most metrics, but it produced four SSHWS Category 5 strength (sustained wind speeds ≥ 137 kt or 70.5 m s^{-1}) typhoons. The North Indian Ocean had near-normal activity. Each of the Southern Hemisphere basins had above-normal numbers of named storms. However, the ACE was below normal for Australia and near-normal for the South Indian Ocean and the Southwest Pacific.

Globally, seven storms reached SSHWS Category 5 strength, which is four more than last year (Diamond and Schreck 2021) and also more than the 1991–2020 mean of 5.3. Four of those storms occurred in the western North Pacific (Surigae, Chanthu, Mindulle, and Rai), and there was one in each of the three Southern Hemisphere basins: Faraji in the South Indian Ocean, Niran near Australia, and Yasa in the Southwest Pacific. Yasa caused major damage to Fiji in December 2020. Super Typhoon Rai was the third costliest typhoon in the history of the Philippines, causing about $1 billion (U.S. dollars) in damages and more than 400 deaths. While not reaching Category 5 status, Hurricane Ida was the most impactful storm in the Atlantic. At $75 billion (U.S. dollars) in damage, Ida was the costliest U.S. disaster of 2021 and the fifth most expensive hurricane on

record (since 1980). Ida's destruction was unique in that its damage was concentrated in two distinct regions. It made landfall as a powerful Category 4 storm in Louisiana, causing heavy damage to the Gulf Coast. As Ida's remnants moved northward, it merged with a frontal system to produce severe weather and flash flooding in the mid-Atlantic states and Northeast, with especially significant impacts in areas of Pennsylvania, New Jersey, and New York. Sidebar 4.1 provides more details on Ida's meteorological history and records.

Table 4.2. Global counts of TC activity by basin for 2021. "+" denotes top tercile; "++" is top 10%; "–" is bottom tercile; "––" is bottom 10% (all relative to 1991–2020). (Note that some inconsistencies between Table 4.2 and the text of the various basin write-ups in section 4g exist and are unavoidable, as tallying global TC numbers is challenging and involves more than simply adding up basin totals, because some storms cross TC basin boundaries, some TC basins overlap, and multiple agencies are involved in tracking and categorizing TCs.)

Basin	TCs	HTCs	Major HTCs	SS Cat 5	ACE ($\times 10^4$ kt^2)
North Atlantic	21 ++	7	4 +	0	146
Eastern Pacific	19 +	8	2 –	0	94 –
Western Pacific	23 –	10 ––	5 –	4 +	209 –
North Indian	5	3 +	1 +	0	21
South Indian	12 +	5	2 –	1 ++	100
Australia	12 +	3 –	2	1 ++	44 –
Southwest Pacific	9 +	4	2	1 ++	41
Global Totals	**97 +**	**38 ––**	**17 ––**	**7 +**	**656 –**

2) ATLANTIC BASIN—M. Rosencrans, E. S. Blake, C. W. Landsea, H. Wang, S. B. Goldenberg, and R. J. Pasch

(i) 2021 Seasonal activity

The 2021 Atlantic hurricane season produced 21 named storms, of which 7 became hurricanes and 4 of those became major hurricanes (Fig. 4.22b). The HURDAT2 (Landsea and Franklin 2013) 1991–2020 seasonal averages (included in IBTrACS) are 14.4 named storms, 7.2 hurricanes, and 3.2 major hurricanes. The 21 named storms during 2021 were the third most on record, trailing the 30 named storms in 2020 and 28 in 2005. Eight of the 21 named storms during 2021 were short-lived (≤ 2 days). There has been a large increase (approximately five per year) in detection of these "shorties" since 2000 (Landsea et al. 2010; Klotzbach et al. 2022). These increased counts primarily reflect new observational capabilities such as scatterometers, Advanced Microwave Sounding Units, and the Advanced Dvorak Technique, and have no association with any known climate variability (Villarini et al. 2011).

The 2021 seasonal Accumulated Cyclone Energy (ACE) value was 149.2% of the 1951–2020 median (which is 96.7×10^4 kt^2; Fig. 4.22c). This value was the 13th highest since 1970 and above NOAA's threshold for an above-normal season (126.1×10^4 kt^2, or 130% of median). There have now been a record six consecutive above-normal seasons, extending the current record of five. Since the current Atlantic high-activity era began in 1995 (Goldenberg et al. 2001; Bell et al. 2019, 2020), there have been 17 above-normal seasons, with 10 of those considered extremely active (ACE ≥ 165% of median, also referred to as hyperactive). By comparison, the preceding 24-year low-activity era of 1971–94 had only two above-normal seasons with none extremely active.

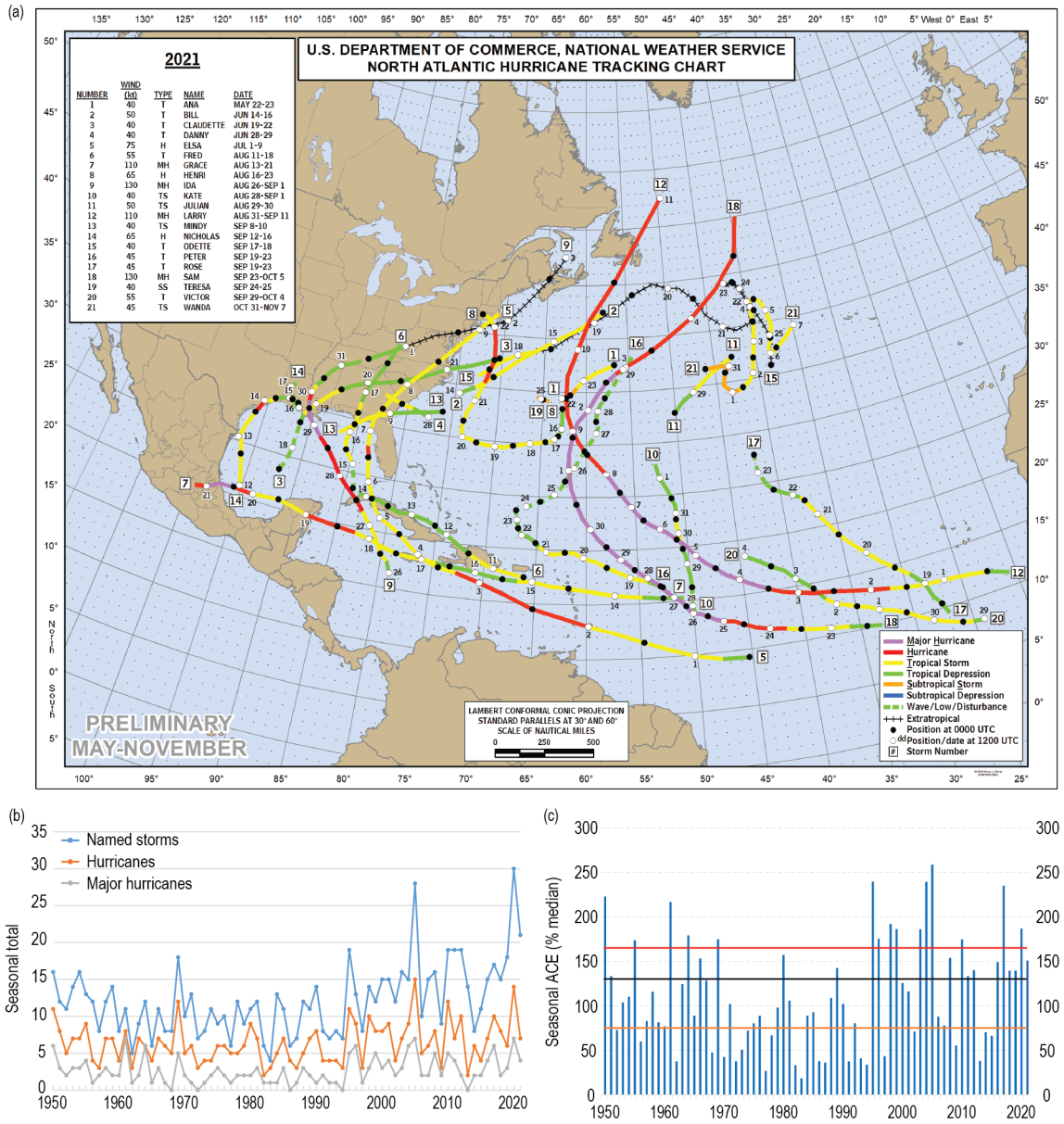

Fig. 4.22. (a) 2021 Atlantic basin storm tracks. Seasonal Atlantic hurricane activity during 1950–2021 for (b) numbers of named storms (blue), hurricanes (orange), and major hurricanes (gray) and (c) the Accumulated Cyclone Energy (ACE) index expressed as percent of the 1951–2020 median value. ACE is calculated by summing the squares of the 6-hourly maximum sustained surface wind speed (kt) for all periods while the storm is at least tropical storm strength. The black (orange) line represents NOAA's limit for an above-normal (below-normal) season and the red line is the threshold for an extremely- (aka hyper-) active season, (http://www.cpc.ncep.noaa.gov/products/outlooks/ background_information.shtml). Note that there is a low bias in activity from the 1950s to the early 1970s due to the lack of satellite imagery and technique (Dvorak) to interpret tropical cyclone intensity for systems over the open ocean. (Source: HURDAT2 [Landsea and Franklin 2013].)

(ii) Storm formation times, regions, and landfalls

Tropical cyclone (TC) activity occurred throughout most of the 2021 hurricane season (Fig. 4.23b), with a TC present every month in the official season as well as in May. Activity ramped up relatively quickly, with Elsa becoming the earliest developing fifth named Atlantic storm on record when it formed on 1 July. Of the first five named storms in the 2021 Atlantic hurricane season, four were classified as a "shortie", lasting two days or fewer. On average, 1–2 named storms form per year during May–July.

August–October (ASO), typically the most active part of the hurricane season, featured 16 named storms during 2021 compared with the 1991–2020 average of 11.1, and at least one TC was present at all times from mid-August through early October. Six of these 16 storms became hurricanes (the

seventh hurricane of the season, Elsa, formed in July), and four of those became major hurricanes. Most of these ASO storms (9 of 16) formed in the main development region (MDR), which is also typical of an above-normal season. The MDR spans the tropical Atlantic Ocean and Caribbean Sea between 9.5°N and 21.5°N (Goldenberg and Shapiro 1996; Goldenberg et al. 2001; Bell and Chelliah 2006; Bell et al. 2017, 2018, 2019). After a highly active late August and most of September, Atlantic TC activity dropped precipitously, with only one named storm developing after 29 September. Tropical Storm Wanda was first named as a subtropical storm on 31 October, gaining tropical characteristics in early November, ending a nearly month-long quiet period.

Historically, above-normal seasons result from a sharp increase in the number, intensity, and duration of storms that develop in the MDR. For the entire 2021 season, 10 of the 21 named storms formed in the MDR (Fig. 4.23a) and accounted for five of the season's seven hurricanes and all of the season's four major hurricanes. The associated MDR-related ACE value was 129% of the basin-wide median. By comparison, named storms forming in the Gulf of Mexico only contributed 5% of the basin-wide median in 2021, and storms from the extratropics contributed 15%. This MDR-related ACE value is lower than the 1991–2020 MDR average for above-normal seasons of 140% of the median. These values are roughly five times higher than the MDR average of 20% of the median for below-normal seasons (defined by NOAA as having a total basin-wide ACE less than 73×10^4 kt^2).

The actual storm tracks during 2021 (Fig. 4.22a) showed two main regions of activity. One area was oriented from west-southwest to east-northeast across the extratropics, where eight named storms formed. The MDR was also active, but in the middle of these active areas there was a quiet area in the extreme southwest Atlantic including the east coast of Florida and the Bahamas.

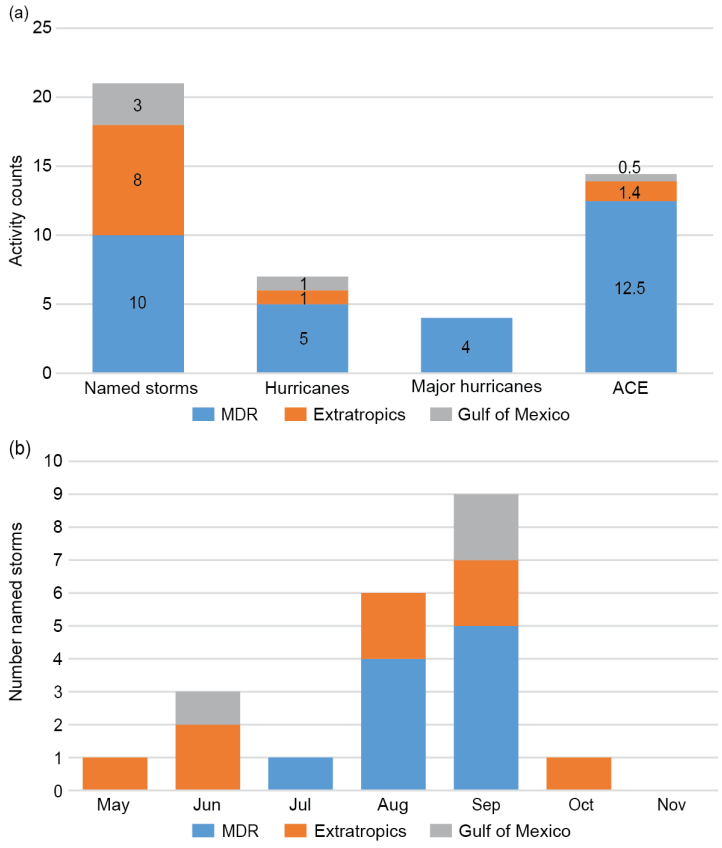

Fig. 4.23. Atlantic TC activity in 2021. (a) Total seasonal storm counts for the three storm classifications and for ACE shown for each region the storm was first named. (b) Named storm counts shown for the month and region the storm was first named. ACE reflects the entire storm ACE and is attributed to the region in which the storm was first named. Regions in (a) and (b) are indicated by the color bar below panel (b). The Atlantic MDR spans 20°–87.5°W and 9.5°–21.5°N. The "extratropics" includes all regions except for the MDR and Gulf of Mexico. (Source: HURDAT2 [Landsea and Franklin 2013].)

Several of the MDR formations have long tracks to the west-northwest. The season also featured eight storms making landfall in the continental United States, with others impacting the Caribbean, Mexico, Central America, Newfoundland, and Bermuda.

Several notable individual storms formed during the 2021 hurricane season. Hurricane Sam was a major hurricane for 7.75 days, contributing ~38% of the total seasonal ACE. Fortunately, Sam's track remained out to sea with minimal impacts. In terms of damage, Hurricane Ida was the largest disaster for the United States in 2021, causing $75 billion (U.S. dollars). Preliminary estimates indicate Ida had winds of 130 kt as it made landfall in Louisiana, which would be tied for the fifth-strongest hurricane to make landfall in the United States since more reliable records began around 1900. In addition to significant damage along the Gulf Coast, Ida also interacted with a cold front to produce torrential rain and flooding across the mid-Atlantic and Northeast. More information on Hurricane Ida is detailed in Sidebar 4.1. Hurricane Henri also brought significant rains to the Northeast just a week earlier, establishing some localized daily records but no large regional records, and causing an estimated $700 million (U.S. dollars) in damage. Hurricane Grace spread damage across the Caribbean and into Mexico, causing an estimated $300 million (U.S. dollars) in damage. Tropical Storms Elsa and Fred and Hurricane Nicholas were storms that each caused more than $1 billion (U.S. dollars) in damage (see section 7b2).

(iii) Sea surface temperatures

Four main sea surface temperature (SST) signals were present during ASO 2021 (Fig. 4.24). First, SSTs were above average throughout the MDR (Fig. 4.24a), and the area-averaged SST anomaly was +0.35°C (Fig. 4.24b). The largest anomalies in the MDR were observed throughout the Caribbean Sea and ranged from just above 0°C to +0.5°C.

Second, the area-averaged SST anomaly in the MDR was higher (by +0.17°C) than that of the remainder of the global tropics (Fig. 4.24c). This signal typifies the warm phase of the Atlantic multi-decadal oscillation (AMO; Enfield and Mestas-Nuñez 1999; Bell and Chelliah 2006) and is a ubiquitous characteristic of Atlantic high-activity eras, such as 1950–70 and 1995–present (Goldenberg et al. 2001; Vecchi and Soden 2007; Bell et al. 2018).

The third SST signal during ASO 2021 reflected above-average temperatures across most of the North Atlantic Ocean. Outside of the MDR, the largest anomalies (exceeding +1°C) occupied the western, and portions of the central, North Atlantic (Fig. 4.24a), areas where numerous tropical storms and hurricanes tracked. The area-averaged SST anomaly in the western North Atlantic (red box, Fig. 4.24a) was +0.79°C and reflected a continuation of exceptional warmth that began in 2014 (Fig. 4.24d).

The fourth SST signal during ASO 2021 was the development of La Niña in the equatorial Pacific (section 4b). As discussed below, La Niña contributed to the enhanced hurricane activity during August and September.

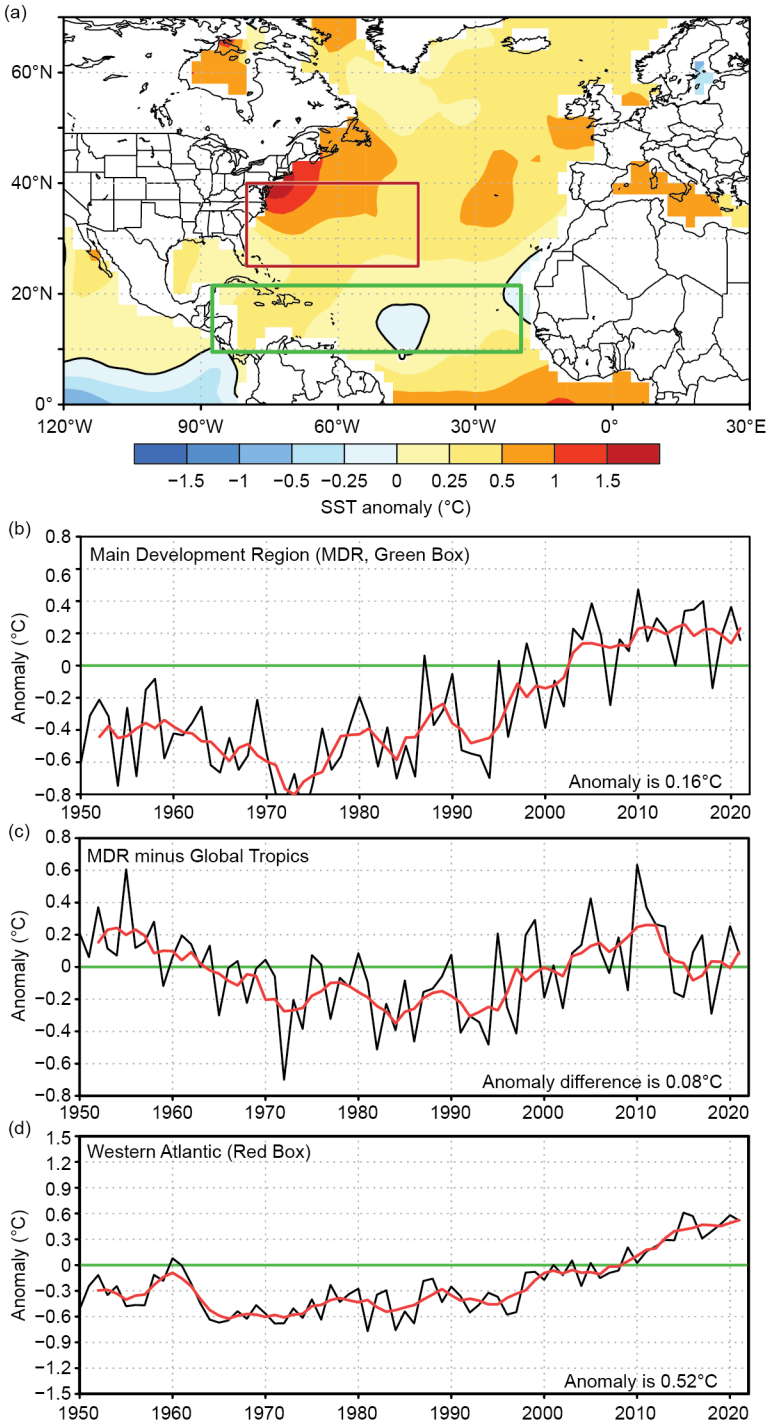

Fig. 4.24. (a) Aug–Oct 2021 SST anomalies (°C). (b–d) Time series of Aug–Oct area-averaged SST anomalies (black) and 5-pt running mean of the time series (red); (b) In the MDR (green box in (a) spanning 20°–87.5°W and 9.5°–21.5°N); (c) difference between the MDR and the global tropics (20°S–20°N); and (d) in the western North Atlantic (red box in (a) spanning 42.5°–80°W and 25°–40°N). Anomalies are departures from the 1991–2020 period means. (Source: ERSST-v5 [Huang et al. 2017].)

(iv) Atmospheric conditions

Climatologically, the ASO peak in Atlantic hurricane activity largely reflects the July–September (JAS) peak in the West African monsoon as noted in section 4e. The inter-related circulation features of an enhanced monsoon act to further increase hurricane activity, while those with an anomalously weak monsoon act to suppress it (Gray 1990; Hastenrath 1990; Landsea et al. 1992; Bell and Chelliah 2006; Bell et al. 2018, 2020). The association on multi-decadal time scales between the West African monsoon and Atlantic hurricane activity largely exists because of a common relationship to multi-decadal modes of variability (Bell and Chelliah 2006).

The West African monsoon was enhanced during JAS 2021, as indicated by negative outgoing longwave radiation (OLR) anomalies across the African Sahel (red box, Fig. 4.25a). Total OLR values in this region averaged 239 W m^{-2} (Fig. 4.25b), with values less than 240 W m^{-2}, indicating deep tropical convection. Consistent with these conditions, the larger-scale divergent circulation at 200-hPa featured an extensive area of anomalous divergence and a core of negative velocity

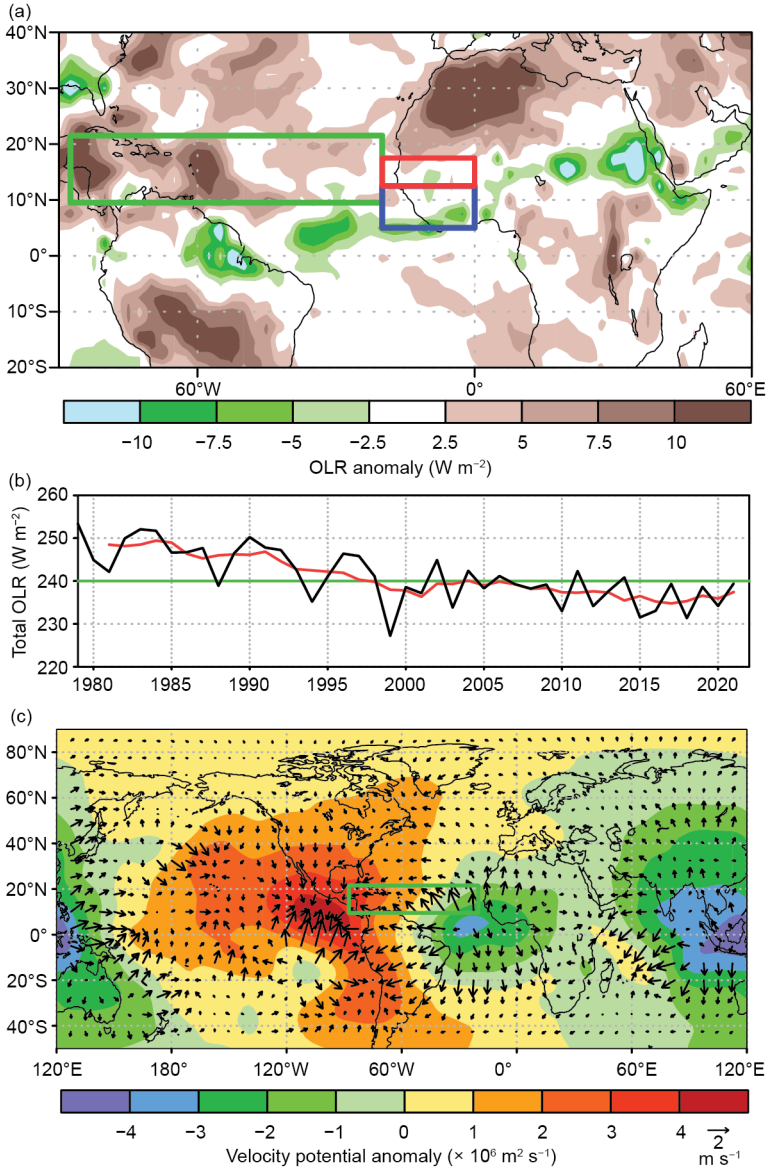

Fig. 4.25. (a) Jul–Sep 2021 anomalous OLR (W m^{-2}), with negative (positive) values indicating enhanced (suppressed) convection. (b) Time series of Jul–Sep total OLR (black) and 5-pt running mean of the time series (red) averaged over the African Sahel region (red box in (a, c) spanning 20°W–0° and 12.5°–17.5°N). (c) Aug–Oct 2021 anomalous 200-hPa velocity potential (× 10^6 m^2 s^{-1}) and divergent wind vectors (m s^{-1}). In (a), contours show total OLR values of 220 W m^{-2} and 240 W m^{-2}. In (a, c), the green box denotes the Atlantic MDR. Anomalies are departures from the 1991–2020 means. (Sources: NCEP/NCAR Reanalysis [Kalnay et al. 1996] for velocity potential and wind, and Liebmann and Smith [1996] for OLR.)

potential anomalies across subtropical northern Africa extending into the eastern Atlantic (Fig. 4.25c). The OLR time series shows that an enhanced monsoon has largely prevailed throughout the current Atlantic high-activity era and warm AMO of 1995–present (Fig. 4.25b). By contrast, a much weaker monsoon with OLR values well above 240 W m^{-2} in the Sahel region was typical of the low-activity and cool AMO period from 1971 to 1994. During ASO 2021, core atmospheric conditions within the MDR reflected a combination of the enhanced West African monsoon, La Niña, and midlatitude influences.

At 200-hPa, the enhanced monsoon amplified subtropical ridges (indicated by anticyclonic streamfunction anomalies) across Africa in both hemispheres (Fig. 4.26a). La Niña impacts in that field (Bell and Chelliah 2006) included cyclonic streamfunction anomalies in both hemispheres of the western and central subtropical Pacific. Farther north, a large anticyclonic anomaly was evident over eastern Canada. Troughing extended from northern Mexico, across Florida, and into the central extratropical Atlantic near 40°N. The streamfunction pattern over the western and central subtropical Pacific aligns with the La Niña response identified in Bell and Chelliah (2006), while the cyclonic streamfunction anomalies over northern Mexico, across Florida, and into the extratropical Pacific are dissimilar to that identified response pattern, pointing to some other source of variability having influence over those regions. The 1000-hPa anomalous height and wind field (Fig. 4.26c) showed just how strong some of the midlatitude circulations were and even shows evidence of flow deep into the tropics. Sea level pressure was also below normal over the central and eastern MDR, which would typically correspond to decreased wind shear and more convection, but vertical wind shear was near normal for the season, and OLR indicates slightly above-normal convection.

The West African monsoon was enhanced and showed direct influences on the circulation pattern during ASO 2021. An aspect of the enhanced West African monsoon system during ASO 2021 was an upward extension of the westerly wind anomalies over the eastern half of the MDR to at least 700-hPa (Fig. 4.26d), which is the approximate level of the African Easterly Jet (AEJ). This anomaly pattern contributed to a deep layer of anomalous cyclonic relative vorticity (i.e., increased horizontal cyclonic shear) along the equatorward flank of the AEJ. These conditions are known to favor increased TC activity by helping African easterly waves to be better maintained

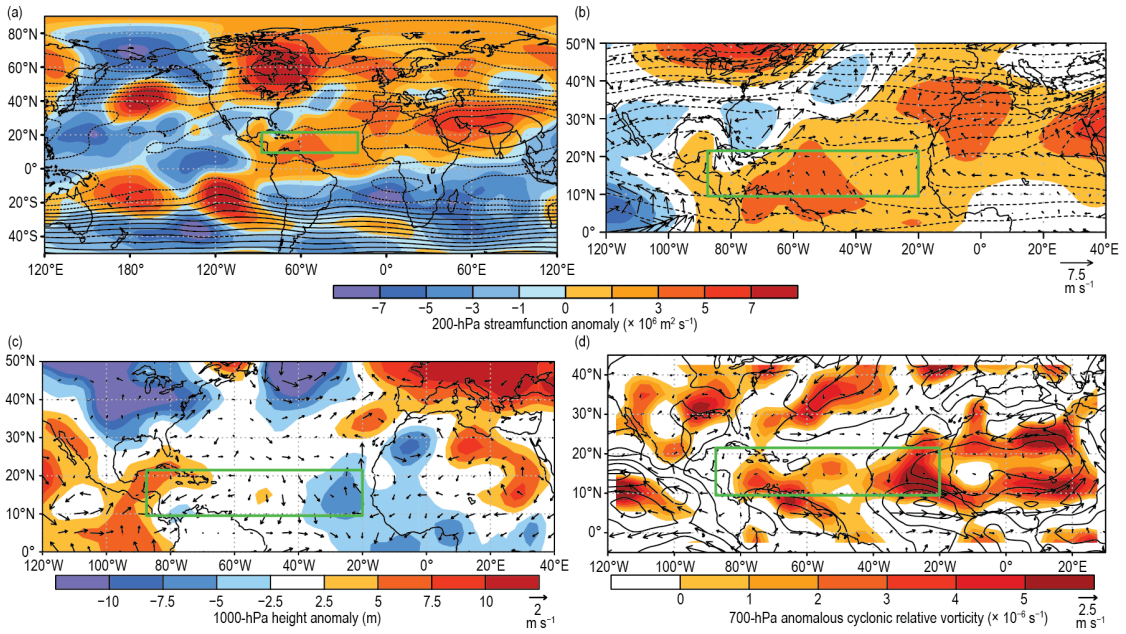

Fig. 4.26. Aug–Oct 2021: (a) 200-hPa streamfunction (contours, interval is 5 × 10^6 m^2 s^{-1}) and anomalies (shaded), with anomalous vector winds (m s^{-1}) also shown in (b); (c) anomalous 1000-hPa heights (shaded, m) and vector winds; and (d) anomalous 700-hPa cyclonic relative vorticity (shaded, × 10^6 m^2 s^{-1}) and vector winds. Green box denotes the MDR. Anomalies are departures from the 1991–2020 means. (Source: NCEP/NCAR Reanalysis [Kalnay et al. 1996].)

and by providing an inherent cyclonic rotation to their embedded convective cells (Bell et al. 2020; Landsea et al. 1998).

The anomalous low-level circulation also reflected an extensive flow of deep tropical moisture into the southern half of the central and eastern MDR. This moisture not only helps feed the monsoon, but also favors increased Atlantic hurricane activity. This situation contrasts with the drier and cooler air that normally accompanies enhanced northeasterly trade winds when the monsoon is weak.

The ASO 2021 200–850-hPa vertical wind shear was about average for much of the MDR and slightly higher than average for the western MDR/Caribbean (Fig. 4.27a). The area-averaged magnitude of the vertical wind shear for the entire MDR was 9.4 m s^{-1} (Fig. 4.27b) and for the Gulf of Mexico was 10.4 m s^{-1} (Fig. 4.27c). Both of these values are above the upper threshold of 8 m s^{-1} considered conducive to hurricane formation on monthly time scales (Bell et al. 2017), so the above-normal overall activity is even more remarkable. The sharp peak and busy month of September, in which nine named storms developed (Fig. 4.23b), was coincident with a period of anomalously low vertical wind shear in the MDR (Fig. 4.27d). The abrupt end to the season, with only one storm developing after 29 September, coincided with a period of anomalously strong wind shear across the Gulf of Mexico, Caribbean, MDR, and the extratropical Atlantic.

The MJO (Madden and Julian 1971), as discussed in section 4c, was generally stationary and inactive during September and October. Nonetheless, variations in the large-scale tropical convection may have played a role in the quiescent October. From September to October, the main convective activity shifted from the Indian Ocean to the Maritime Continent, as assessed via a combination of the multivariate MJO index of Wheeler and Hendon (2004; Fig. 4.8d) and Climate Prediction Center's weekly MJO analysis. For a typical MJO, this circulation results in increased shear over and decreased convection in the tropical Atlantic (Mo 2000), both of which decrease

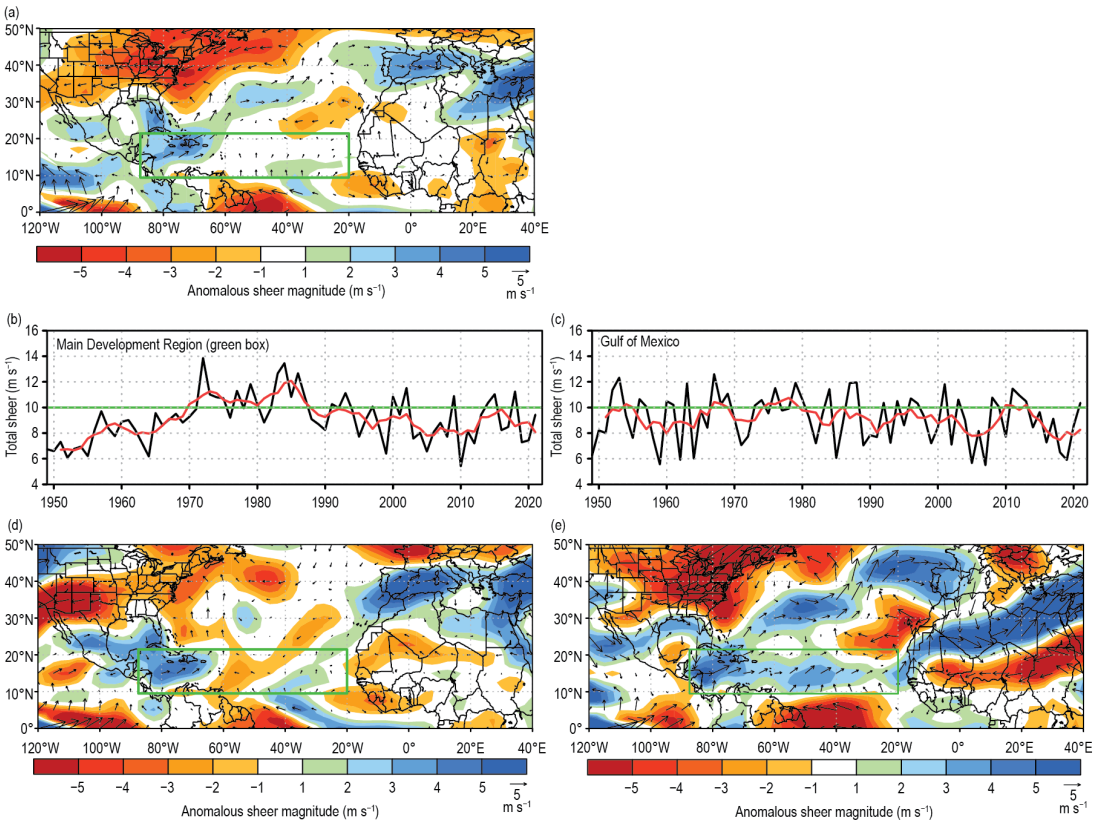

Fig. 4.27. Aug–Oct (ASO) magnitude of the 200–850-hPa vertical wind shear (m s^{-1}): (a) 2021 anomalous magnitude and vector. (b, c) Time series of ASO vertical wind shear magnitude (black) and 5-pt running mean of the time series (red) averaged over (b) the MDR (spanning 87.5°–20°W and 9.5°–21.5°N), and (c) the western Gulf of Mexico (spanning 80°–97.5°W and 21.5°–30°N). (d) Same as (a), but for Sep 2021. (e) Same as (d), but for Oct 2021. Anomalies are departures from the 1991–2020 means. (Source: NCEP/NCAR Reanalysis [Kalnay et al. 1996].)

tropical cyclone formations. Even if this were not a typical MJO, the shift in the variations of the tropical circulation may have contributed to the lack of activity in October.

The above conditions typified the many active seasons seen during the current Atlantic high-activity era. However, as with other years, interannual signals were also in play during 2021. One of those was La Niña, which favors enhanced activity as in other recent La Niña events (2010, 2016, and 2020). However, the La Niña impact may have been reduced by other interannual signals like the strong ridge over eastern Canada (Figs. 4.26a,c) with troughing over the central extratropical Atlantic and over the Gulf of Mexico. The ridge/trough combinations likely contributed to increased wind shear, especially late in the season, which may have capped activity, despite the presence of many features of the high-activity era (above-normal SST, enhanced West African Monsoon, and early season activity).

Sidebar 4.1: Hurricane Ida: A landfalling Louisiana major hurricane for the record books—P. KLOTZBACH AND R. TRUCHELUT

The 2021 Atlantic hurricane season was the sixth consecutive above-average season based on NOAA's definition, with 21 named storms, seven hurricanes, and four major hurricanes. Eight named storms and two hurricanes made landfall in the continental United States, with Hurricane Ida by far the most significant landfalling Atlantic tropical cyclone of the year. Ida struck near Port Fourchon, Louisiana, with maximum 1-minute sustained winds of 130 kt (67 m s^{-1}) on 29 August. Wind and surge caused tremendous destruction in south-central and southeastern Louisiana, with the New Orleans metropolitan area also experiencing significant wind damage. Ida's remnants interacted with a frontal system to cause significant flash flooding across the coastal plain of the northeastern United States, including Pennsylvania, New Jersey, New York, and Connecticut. The National Hurricane Center's best track report on Hurricane Ida (Beven et al. 2022) estimated that Ida caused ~$75 billion (U.S. dollars) in damage.

Here, we discuss the meteorological history of Ida and highlight some of the records that Ida set. Historical landfall records from 1851 to present are taken from the National Hurricane Center/Atlantic Oceanographic and Meteorological Laboratory archive (http://www.aoml.noaa.gov/hrd/hurdat/All_U.S._Hurricanes.html). Ida's observed values are taken from the Atlantic hurricane database (HURDAT2; Landsea and Franklin 2013) that is based on Beven et al. (2022).

Ida developed from a high-amplitude easterly wave, becoming a tropical depression at 1200 UTC on 26 August in the west-central Caribbean and intensifying into a tropical storm by 1800 UTC. Over the following 24 hours, Ida rapidly intensified from 35 kt (18 m s^{-1}) to 70 kt (36 m s^{-1}), while tracking northwestward in a light shear and warm water environment in the western Caribbean. Ida made two landfalls in Cuba as a Category 1 hurricane on 27 August, the first on the Isle of Youth and the second on Pinar Del Rio. Disruption of Ida's circulation due to land interaction and dry air entrainment temporarily arrested Ida from strengthening, and it remained a Category 1 hurricane through 28 August.

As Ida continued northwest, vertical wind shear relaxed as the hurricane tracked over a warm eddy in the east-central Gulf of Mexico, causing rapid intensification. Between 1200 UTC on 28 August and 1200 UTC on 29 August, Ida's maximum sustained winds increased by 60 kt (31 m s^{-1}), from 70 kt (36 m s^{-1}) to 130 kt (67 m s^{-1}). This 60-kt intensification in 24 hours slightly exceeded Hurricane Laura (2020)'s rate of 55 kt (28 m s^{-1}) in 24 hours in the Gulf of Mexico. Laura also made landfall over Louisiana as a 130 kt (67 m s^{-1}) hurricane in late August. During this same time period, Ida's minimum central pressure fell 57 hPa (from 986 hPa to 929 hPa). At the peak of its intensification, Ida's pressure per aircraft reconnaissance fell by ~11 hPa in one hour between 1000 UTC and 1100 UTC on 29 August. Ida maintained a 130-kt intensity until initial landfall near Port Fourchon, Louisiana at ~1655 UTC on 29 August (Fig. SB4.1).

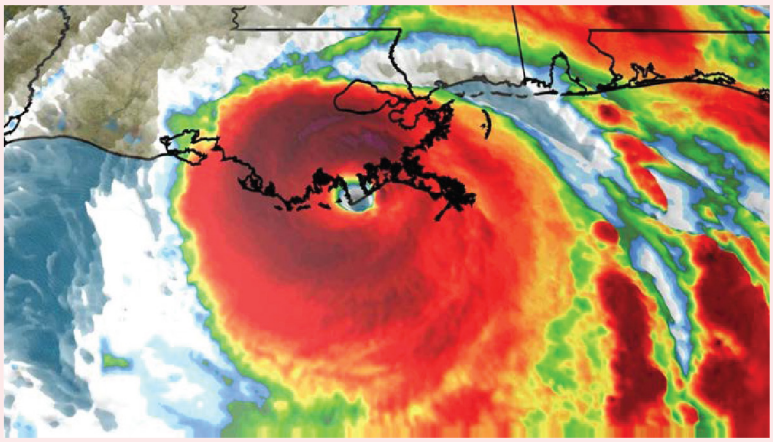

Fig. SB4.1. Infrared satellite image of Hurricane Ida at the time of its landfall at ~1655 UTC on 29 Aug 2021. Image courtesy of NOAA.

Following landfall, Ida only slowly weakened. Ida maintained Category 3+ hurricane intensity for at least five hours and Category 1+ hurricane intensity for at least 11 hours following initial landfall. This is likely due to a combination of factors, including a slow forward motion that kept part of Ida's circulation over water for most of 29 August and elevated soil moisture due to heavy antecedent rainfall over southern Louisiana. The system weakened to a tropical storm by mid-day on 30 August as it accelerated northeast over Mississippi, and it became a tropical depression on 31 August.

Ida was officially declared post-tropical while located over West Virginia on 1 September. However, as a post-tropical cyclone, Ida interacted with a frontal zone and produced copious rainfall (Fig. SB4.2), several violent tornadoes, and devastating flash flooding across the northern mid-Atlantic and southern New England. Flooding was particularly severe in and around the New York City metropolitan area, where widespread rainfall totals of 150–250 mm were recorded, including a 1-hour accumulation of 80 mm in New York's Central Park between ~0100 and 0200 UTC on 2 September. The estimated return period for 12-hour rainfall totals as observed from post-tropical Ida from the northern suburbs of Philadelphia northeast into coastal Connecticut is generally 100 to 200 years, with locally higher return periods. The final advisory on post-tropical Ida was issued on 2 September.

Hurricane Ida caused tremendous damage in southern Louisiana, with loss estimates in Louisiana of ~$55 billion (U.S. dollars), according to Beven et al. (2022). Flash flooding in the mid-Atlantic states was responsible for an additional ~$205 million in damage. Ida caused 55 direct and 32 indirect fatalities in the United States, and its precursor disturbance also caused significant flooding in Venezuela, which led to 20 fatalities. Storm surge exceeding three meters was reported to the east of where Ida made landfall. Ida's strong winds also led to extensive power outages, with over one million residents in Louisiana reported without electricity at one point.

Ida's 130 kt (67 m s^{-1}) intensity at landfall ties the Last Island Hurricane (1856) and Hurricane Laura (2020) for the strongest maximum sustained winds for a Louisiana landfalling hurricane on record. These sustained winds also equaled the fifth strongest on record for the continental United States. Ida's landfall pressure of 931 hPa was the second lowest for a Louisiana hurricane on record, trailing only Katrina (920 hPa), which struck on the same date 16 years prior to Ida. Laura and Ida are also the first two 130+ kt hurricanes on record to make landfall in the continental United States in consecutive years. The continental United States has now experienced three 130+ kt hurricane landfalls in the past four years: Michael (2018), Laura (2020), and Ida (2021). This equals the three 130+ kt hurricane landfalls recorded in the previous 82 years, 1936–2017: Camille (1969), Andrew (1992), and Charley (2004).

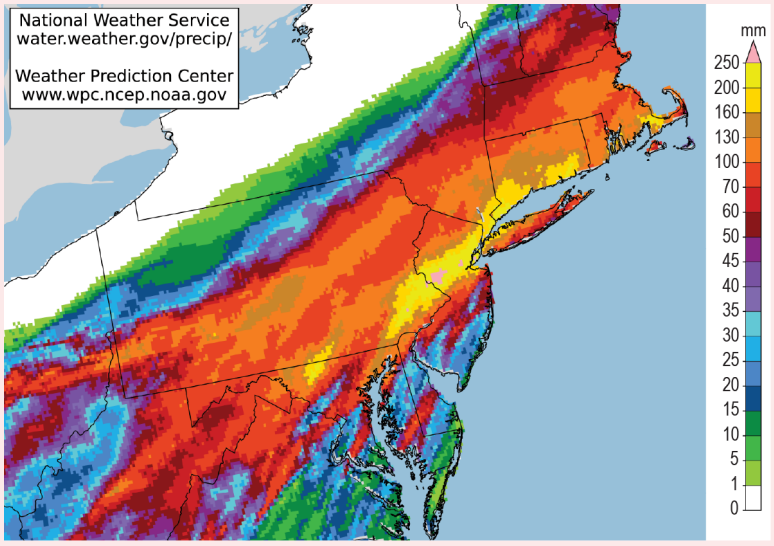

Fig. SB4.2. 48-h radar-estimated rainfall (mm) across the mid-Atlantic states and southern New England ending at 1200 UTC on 2 Sept 2021. Image courtesy of Gregory Carbin, NOAA/Weather Prediction Center.

3) EASTERN NORTH PACIFIC AND CENTRAL NORTH PACIFIC BASINS—K. M. Wood and C. J. Schreck

(i) Seasonal activity

Storm counts in this section are combined from the two agencies responsible for issuing advisories and warnings in the eastern North Pacific (ENP) basin: NOAA's National Hurricane Center in Miami, Florida (for the region from the Pacific coast of North America to 140°W), and NOAA's Central Pacific Hurricane Center in Honolulu, Hawaii (for the region between 140°W and the date line, the central North Pacific [CNP]).

A total of 19 named storms formed in the combined ENP/CNP basin (Fig. 4.28a), 8 of which became hurricanes and 2 became major hurricanes. This activity is above normal for named storms, near normal for hurricanes, and below normal for major hurricanes compared with the 1991–2020 averages of 16.9 named storms, 8.8 hurricanes, and 4.6 major hurricanes. All but one named storm occurred between the official hurricane season start date of 15 May and end date of 30 November. The first TC of the season, Tropical Storm Andres, developed on 9 May. The final named storm, Tropical Storm Sandra, weakened to a tropical depression (TD) on 8 November and dissipated the next day. No named storms were active within the CNP, which is well below the 1991–2020 average of 3.4 for the CNP.

The 2021 seasonal ACE index was 94.0 × 10^4 kt^2, or 71% of the 1991–2020 mean of 132.8 × 10^4 kt^2 (Fig. 4.28b; Bell et al. 2000), continuing the streak of below-normal activity that has persisted since 2019 (Fig. 4.28b; Wood and Schreck 2020, 2021). Much of this season's TC activity, including

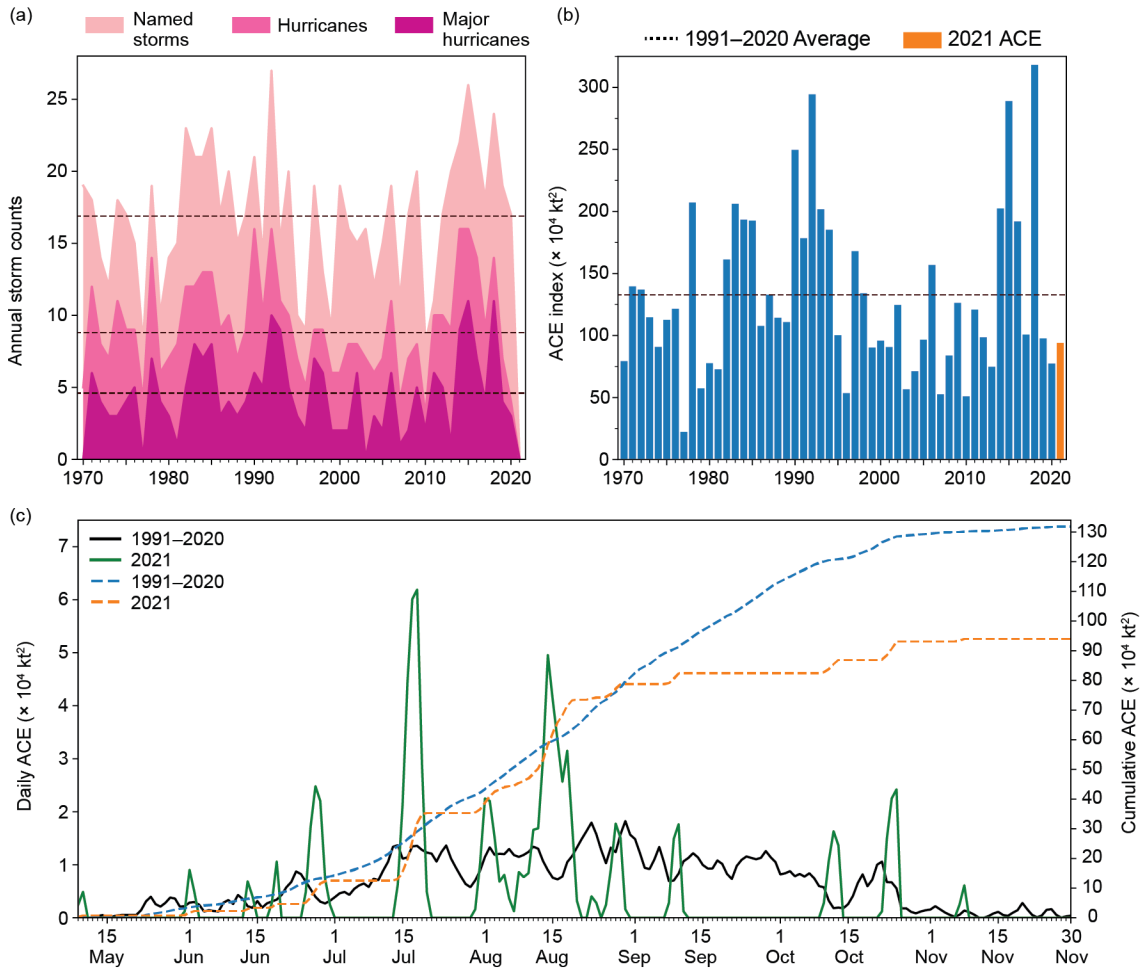

Fig. 4.28. (a) Annual ENP/CNP storm counts by category during the period 1970–2021, with the 1991–2020 average by category denoted by each dashed line. (b) Annual ACE (× 10^4 kt^2) during 1970–2021, with 2021 highlighted in orange and the 1991–2020 average denoted by the dashed line. (c) Daily ACE during 1991–2020 (solid black) and during 2021 (solid green); accumulated daily ACE during 1991–2020 (dashed blue) and during 2021 (dashed orange).

three hurricanes and both major hurricanes, was confined to July and August, in which 71% of the total ACE occurred. One hurricane (Olaf) formed in September and two (Pamela and Rick) in October (Fig. 4.28c).

The two 2021 ENP TCs that peaked as at least Category 4 hurricanes (115 kt; 59 m s^{-1}) on the Saffir-Simpson Hurricane Wind Scale contributed just over half of the season's total ACE. Hurricane Felicia (14–20 July; Cangialosi 2021a) rapidly intensified (≥ 30 kt or 15.4 m s^{-1} in 24 hours) prior to reaching its peak intensity of 125 kt (64 m s^{-1}) and eventually rapidly weakened while over the open ocean (≤ –30 kt or –15.4 m s^{-1} in 24 hours; Wood and Ritchie 2015). Hurricane Linda (10–19 August; Reinhart 2021) also rapidly intensified prior to peaking as a 115-kt major hurricane, followed by a weakening and re-intensification period that ultimately resulted in rapid weakening prior to dissipation. Both Felicia and Linda exhibited a peak 24-hour intensification of 35 kt (18 m s^{-1}). Though neither TC maintained its peak intensity for more than 12 hours, Felicia remained at major hurricane strength for 66 hours and Linda for 48 hours, their longevity contributed to these two TCs becoming the highest ACE producers of the season.

(ii) Environmental influences

Negative sea surface temperature (SST) anomalies marked much of the equatorial eastern Pacific during the 2021 ENP hurricane season alongside easterly 850-hPa wind anomalies (Fig. 4.29), likely associated with the La Niña event established in August, following the 2020 La Niña (NOAA 2020, 2021). Notably, season-averaged SSTs were near or above normal where most TCs formed and tracked (Fig. 4.29a). Most TC activity was confined to the eastern part of the basin, where OLR anomalies were near or below normal and co-located with near- or below-normal vertical wind shear (Figs. 4.29b,c). However, few TCs tracked through the below-normal shear that occurred near 140°W. Unlike recent ENP seasons, 2021 was marked by enhanced 850-hPa westerly flow near Central America, which may have contributed to the clustering of activity in the eastern part of the basin by enhancing the available low-level cyclonic vorticity (Fig. 4.29d).

Tropical cyclone activity in the ENP, especially cyclogenesis, can be affected by the MJO as well as convectively-coupled Kelvin waves (e.g., Maloney and Hartmann 2001; Aiyyer and Molinari 2008; Schreck and Molinari 2011; Ventrice et al. 2012a,b; Schreck 2015, 2016). A relatively robust MJO signal occurred in late July into early August, coinciding with the formation of four TCs in the eastern part of the basin: Hilda, Ignacio, Kevin, and Linda (Fig. 4.30; see Kiladis et al. 2005, 2009 for methodology). In addition, the passage of a Kelvin wave coincided with the development of Hilda and Ignacio. Other Kelvin waves likely contributed

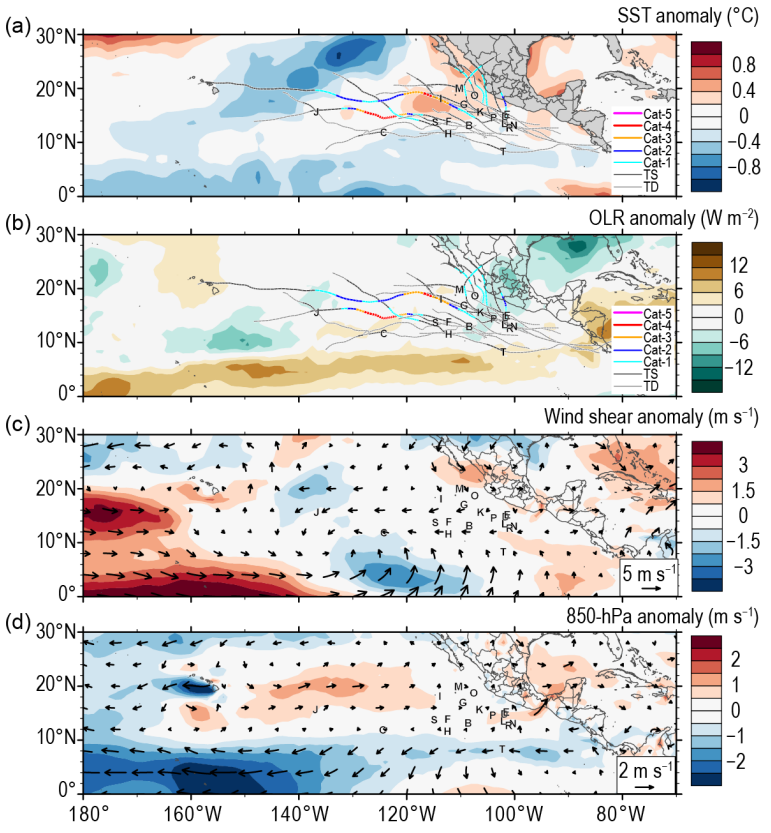

Fig. 4.29. 15 May–30 Nov 2021 anomaly maps of (a) SST (°C; Banzon and Reynolds 2013), (b) OLR (W m^{-2}; Schreck et al. 2018), (c) 200–850-hPa vertical wind shear (m s^{-1}) vector (arrows) and scalar (shading) anomalies, and (d) 850-hPa wind (m s^{-1}, arrows) and zonal wind (shading) anomalies. Anomalies are relative to the annual cycle from 1991–2020. Letters denote where each TC reached tropical storm intensity. Wind data are obtained from CFSR (Saha et al. 2014).

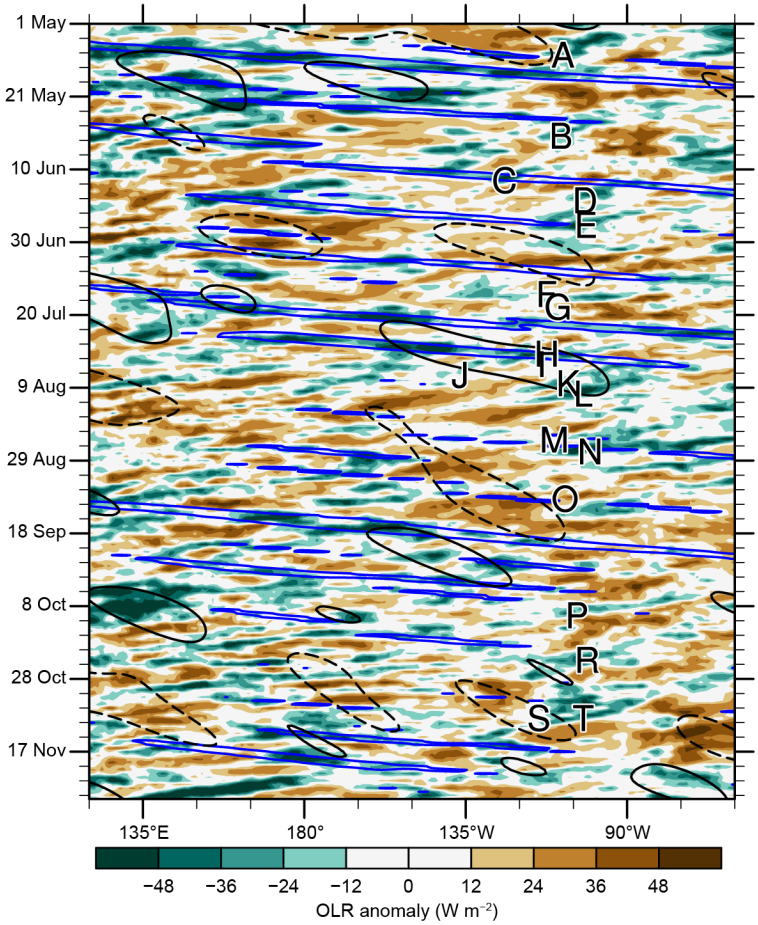

Fig. 4.30. Longitude–time Hovmöller diagram of 5°–15°N average OLR (W m^{-2}; Schreck et al. 2018). Unfiltered anomalies, from a daily 1991–2020 climatology are shaded. Negative anomalies (green) indicate enhanced convection. Anomalies filtered for Kelvin waves are contoured in blue at –10 W m^{-2} and MJO-filtered anomalies in black at ±10 W m^{-2} (dashed for positive, solid for negative). Letters denote the longitude and time when each TC reached tropical storm intensity.

to the formation of Carlos and Enrique. Finally, easterly wave activity can be inferred from Fig. 4.30 as westward-moving negative (green) anomalies; such waves were active during most of the ENP genesis events.

(iii) Impacts

Five ENP TCs made landfall on the west coast of Mexico in 2021: Tropical Storm Dolores, and Hurricanes Nora, Olaf, Pamela, and Rick. In addition, Hurricane Enrique dissipated just offshore of Baja California in the southern Gulf of California. The earlier-noted cluster of TC activity in the eastern part of the basin likely contributed to an enhanced risk of landfall relative to climatology; on average, 1.8 ENP TCs make landfall in Mexico each year (Raga et al. 2013).

Tropical Storm Dolores (18–20 June) caused three deaths from lightning, produced significant flooding in multiple Mexican states, and is estimated to have caused $50 million (U.S. dollars) in economic losses (Papin 2022). Hurricane Nora (26–30 August; https://www.nhc.noaa.gov/data/tcr/EP142021_Nora.pdf), moved parallel to the Mexican coast for an extended period of time before finally moving inland, likely causing at least $125 million (U.S. dollars) in damage in Mexico and three deaths (Aon 2021a,b). Hurricane Olaf (7–11 September) led to one direct fatality from a mudslide, caused over 190,000 customers to lose power, and resulted in an estimated $10 million (U.S. dollars) in damage (Latto 2022). No direct deaths were attributed to Hurricane Pamela (10–13 October), but two people died in Texas due to flooding induced by its remnants. The storm also caused widespread flooding and moderate wind damage in Mexico (Cangialosi 2021b). Hurricane Rick (22–25 October) caused one direct fatality, damaged over 1200 houses, and likely caused tens of millions of dollars in economic losses (Berg 2022). Though Hurricane Enrique (25–30 June) did not make landfall, its heavy rains caused freshwater flooding, river flooding, and landslides in northwest Mexico, with a peak rainfall estimate of 542 mm at Lazaro Cardenas, resulting in damage and power outages. Two direct deaths were attributed to high surf and rip currents (Latto 2021).

4) WESTERN NORTH PACIFIC BASIN—S. J. Camargo

(i) Overview

The 2021 TC season in the western North Pacific was below normal by most measures of TC activity. The data used here are primarily from JTWC best-track data for 1945–2020 and preliminary operational data for 2021. All statistics are based on the 1991–2020 climatological period unless otherwise noted.

According to the JTWC a total of 23 TCs (bottom quartile ≤ 23) reached tropical storm intensity in 2021. From these, 10 reached typhoon intensity (bottom quartile ≤ 13), with 4 reaching super typhoon status (≥ 130 kt, median = 5). There were also 6 tropical depressions (median 4.5). Only 44% of the tropical storms intensified into typhoons (bottom quartile ≤ 56%), while 40% of the typhoons reached super typhoon intensity (median = 29%). Figure 4.31a shows the number of storms in each category for the period 1945–2021.

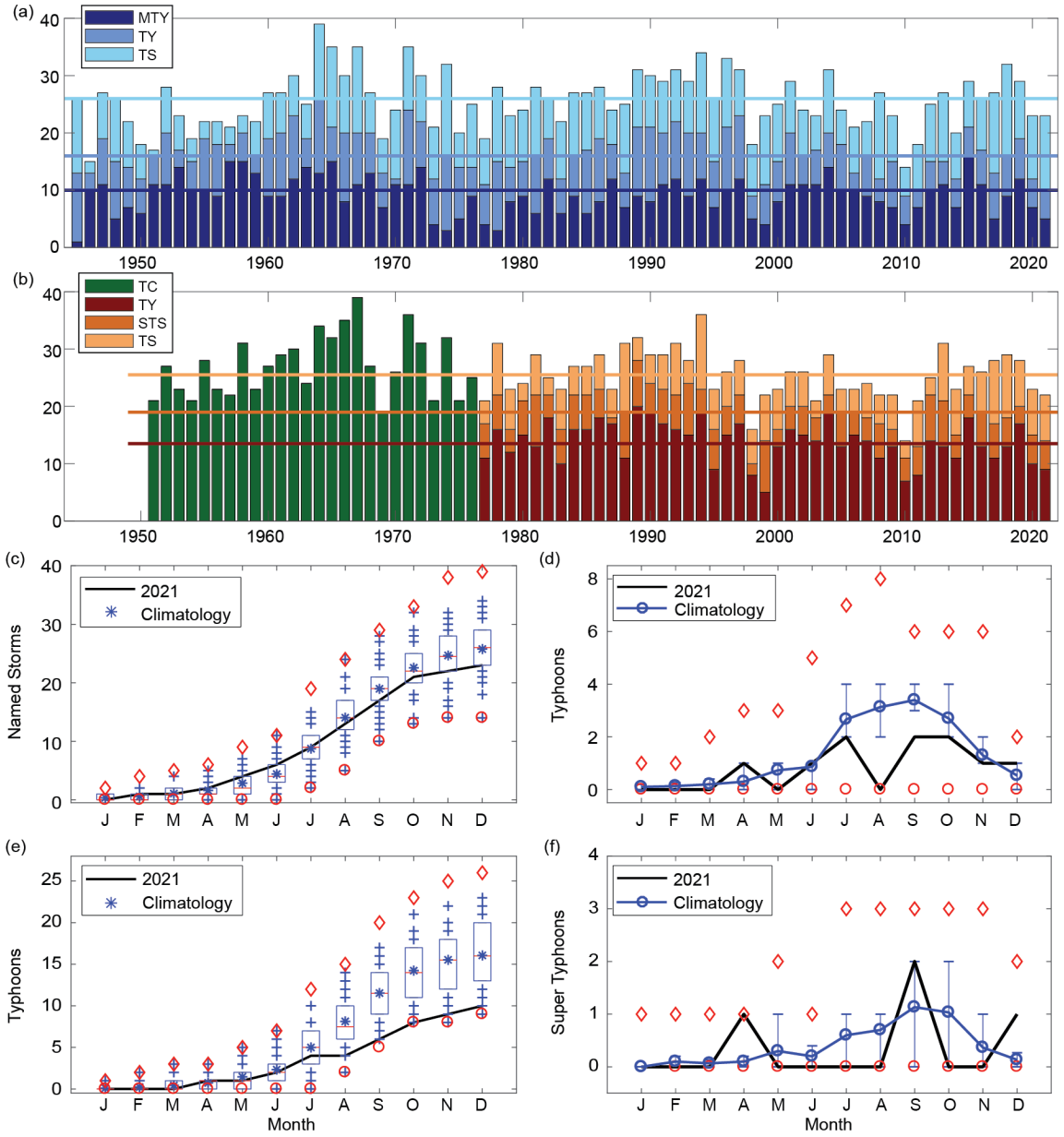

Fig. 4.31. (a) Number of tropical storms (TSs), typhoons (TYs), and major typhoons (MTY ≥ 96 kt) per year in the western North Pacific (WNP) for the period 1945–2021 based on JTWC data. (b) Number of tropical cyclones (TCs; all storms that reach TS intensity or higher) from 1951 to 1976; number of TSs, severe tropical storms (STSs), and TYs from 1977 to 2021 based on JMA data. (c) Cumulative number of tropical cyclones with TS intensity or higher (named storms) per month in the WNP in 2021 (black line) and climatology (1991–2020) as box plots (interquartile range: box; median: red line; mean: blue asterisk; values in the top or bottom quartile: blue crosses; high (low) records in the 1945–2021 period: red diamonds (circles). (e) As in (c) but for the number of typhoons. (d) and (f) show the number of typhoons and super typhoons (≥ 130 kt) per month in 2021 (black line) and the climatological mean (blue line); the red diamonds and circles denote the maximum and minimum monthly historical records and the blue error bars show the climatological interquartile range for each month (in the case of no error bars, the upper and/or lower percentiles coincide with the median). (Sources: 1945–2020 Joint Typhoon Warning Center [JTWC] best-track dataset, 2021 JTWC preliminary operational track data for [a], [c], [d], [e], and [f]. 1951–2021 Regional Specialized Meteorological Center-Tokyo, Japan Meteorological Agency [JMA] best-track dataset for [b].)

The JMA total for 2021 was 22 TCs (bottom quartile ≤ 23). As is typically the case, there were differences between the JTWC and JMA counts.[4] Storm Three (03W) was considered a tropical storm by JTWC, but was not included among the JMA 2021 storms. Namtheun was considered a typhoon by JTWC, but not by JMA (severe tropical storm). Of the 22 JMA TCs, 9 were tropical storms (top quartile ≥ 8), 5 were severe tropical storms (median = 5), and 9 were typhoons (bottom quartile ≤ 11). Only 41% of the storms reached typhoon intensity (bottom quartile ≤ 48%). The number of all TCs (1951–76) and tropical storms, severe tropical storms and typhoons (1977–2021) according to the JMA are shown in Fig. 4.31b. The Philippine Atmospheric, Geophysical and Astronomical Services Administration (PAGASA) named 15 TCs that entered its area of responsibility, including Storm 03W, named Crising locally by PAGASA, and tropical depression Nando (8–16 October), which was not named by JMA or JTWC.

(ii) Seasonal activity

The 2021 season started with the occurrence of only one storm in the period January–March (median = 0): Tropical Storm Dujuan (local name Auring), which affected the Philippines in February. Super Typhoon Suriage was active in April, only the ninth year in the historical record with a super typhoon in April (top quartile > 0), followed by Tropical Storms 03W and Choi-wan in May (top quartile ≥ 2). June had two storms (top quartile ≥ 2): Tropical Storm Koguma (top quartile ≥ 1) and Typhoon Champi (top quartile ≥ 1). The early typhoon season (January–June) had a total of 6 TCs (median = 6), with 4 tropical storms (top quartile ≥ 3) and 2 typhoons (median = 2), including 1 super typhoon (top quartile ≥ 1), as shown in Figs. 4.31c–f.

July had 5 TCs (median = 4), 2 tropical depressions (07W and 08W), 1 tropical storm (Nepartak; median = 1), and 2 typhoons (In-fa and Cempaka; bottom quartile ≤ 2). There were also 5 TCs in August (median = 6), 1 tropical depression (12W), and 4 tropical storms (Lupit, Mirinae, Nida, and Omais; top quartile ≥ 3), but none intensified to typhoon strength. The lack of typhoons active in August is a rather unusual occurrence (bottom quartile ≤ 2; see Figs. 4.31d,e) and previously only occurred in three other years in the historical record (1976, 1977, and 2014).

September also had 5 TCs (bottom quartile ≤ 5), 1 tropical depression (17W), 2 tropical storms (Conson and Dianmu; top quartile ≥ 2), and 2 typhoons (Chanthu and Mindulle; bottom quartile ≤ 3), both reaching super typhoon intensity (top quartile ≥ 2). While the number of typhoons in September was below normal, the number of super typhoons was above normal (Figs. 4.31d,f). October also had 5 TCs (top quartile ≥ 5): 1 tropical depression (26W), 2 tropical storms (Lionrock and Kompasu; top quartile ≥ 1), and 2 typhoons (Namtheun and Malou; median = 2.5). The peak season (July–October) had a total of 21 TCs (median = 20) and 9 tropical storms (top quartile ≥ 8). The number of TCs and tropical storms is in the near-normal range, but only 7 typhoons (bottom quartile ≤ 9) with just 2 reaching super typhoon intensity (bottom quartile ≤ 2) occurred during the peak season (Figs. 4.31c,e).

Typhoon Nyatoh formed in November, the only storm active in that month (TC and typhoon bottom quartiles ≤ 1). The season closed with 2 TCs in December (top quartile ≥ 2): the devastating Super Typhoon Rai (typhoons: top quartile ≥ 1; super typhoons: top quartile > 0) followed by Tropical Depression 29W. Super typhoons in December are uncommon. Since 1980, when the data quality became more reliable, super typhoons have only developed in four other Decembers (1997, 2001, 2002, and 2016), with the remaining other seven occurrences happening in the 1950s and 1960s. The total number of TCs in the late season (November and December) was 3 (bottom quartile ≤ 3), including 2 typhoons (top quartile ≥ 2) and 1 super typhoon (top quartile ≥ 1). The low number of typhoons and super typhoons during the peak season was mainly responsible for the season being characterized as below normal, even with the relatively high level of activity in December.

[4] It is well known that there are systematic differences between the JMA and the JTWC and the datasets, which have been extensively documented in the literature (e.g., Knapp et al. 2013; Schreck et al. 2014).

The total seasonal ACE in 2021 (Fig. 4.32a) was in the bottom quartile of the climatological distribution, the 16th lowest in the historical record. The ACE value was in the bottom quartile of the climatological distribution in January, March, August, October, and November (Fig. 4.32b). January and March both had zero ACE, while the latter three months were respectively the third, seventh, and fourth lowest ACE values in the historical record for those months. In contrast, in February, April, and December, the ACE values were in the top quartile of the climatological distribution, reaching the 10th, 4th, and 13th highest ACE values in the historical record for those months. While the ACE climatological values are typically low in January and March (climatologically: 0.3% and 0.9% of the season total), August and October are in the peak typhoon season and have high climatological ACE values, typically contributing a combined 40% of seasonal ACE; therefore, the combined low ACE value in those months (only 14%) was a major factor in the low total ACE value. Low ACE values are typical of La Niña in the western North Pacific (Camargo and Sobel 2005), which was present most of the year (section 4b). During La Niña events the mean typhoon genesis is displaced to the northwest, leading to shorter tracks and weaker typhoons and, subsequently, to lower ACE values.

The ACE for four storms in 2021 were in the top quartile of the climatological ACE for individual storms: Typhoon Rai and Super Typhoons Surigae, Chanthu, and Mindulle. The ACE for Surigae was in the 99th percentile. Together these four storms contributed to 65% of the total seasonal ACE (21%, 19%, 14%, and 11% respectively).

The mean genesis location in 2021 was 15.3°N and 133.3°E, northwest of the climatological mean of 13.3°N, 140.5°E. The mean track position in 2021 was 18.9°N, 132.1°E, similarly northwest of the climatology mean of 17.8°N, 135.9°E (standard deviations of 1.6° latitude and 5.2° longitude). There is a well-known connection between genesis and track shifts in the WNP basin and El Niño/La Niña (Chia and Ropelewski 2002; Camargo and Sobel 2005; Camargo et al. 2007a) to the southeast/northwest. The 2021 first position conditions are typical of La Niña seasons (genesis mean La Niña: 15.1°N, 136.5°E).

There were 88.25 days in 2021 with active tropical storms and typhoons (bottom quartile ≤ 86). From these active days, 36.75 had typhoons (bottom quartile ≤ 42.7), 18.5 days had major (including super) typhoons (SSHWS categories 3–5; bottom quartile ≤ 15.75). The percentage of active days with typhoons and major typhoons was 28% (bottom quartile ≤ 27%) and 14% (median = 15%), respectively. The median lifetime for TCs reaching tropical storm intensity was 5.5 days (bottom quartile ≤ 7 days) and for those reaching typhoon intensity was 7.5 days (bottom quartile ≤ 7.75 days).

The longest-lived storm in 2021 was Typhoon In-fa (14 days), followed by Tropical Storm Omais (13.75 days) and Super

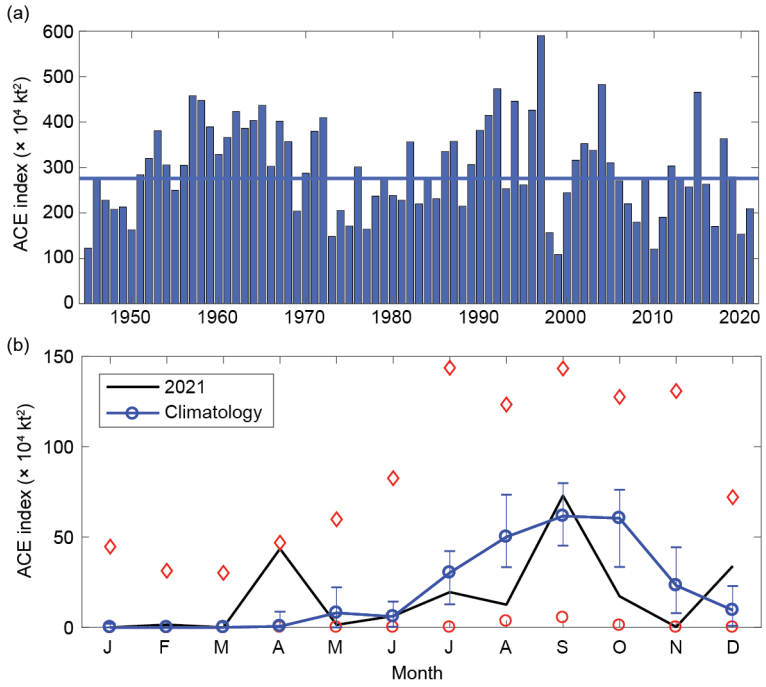

Fig. 4.32. (a) Accumulated Cyclone Energy (ACE, × 10^4 kt^2) per year in the western North Pacific for the period 1945–2021. The solid blue line indicates the median for the climatology (1991–2020). (b) ACE per month in 2021 (black line) and the median during 1991–2020 (blue line), the blue error bars indicate the climatological interquartile range. In case of no error bars, the upper and/or lower percentiles coincide with the median. The red diamonds and circles denote the maximum and minimum values per month during the 1945–2020 period. (Source: 1945–2020 Joint Typhoon Warning Center [JTWC] best-track dataset, 2021 JTWC preliminary operational track data.)

Typhoons Surigae (12.25 days) and Chanthu (12 days), with all four storms in the top quartile of the distribution (≥ 10 days). From the 23 TCs, only 8 had lifetimes above the median (7.25 days). Short-lived storms are another characteristic of La Niña in the western North Pacific (Camargo and Sobel 2005; Camargo et al. 2007a). The maximum number of TCs active simultaneously in 2021 was four and occurred on 5 August (Tropical Depression 12W and Tropical Storms Lupit, Mirinae, and Nida). The historical record is six active TCs in the basin (14–15 August 1996).

(iii) Environmental conditions

Figure 4.33 shows the tracks and environmental conditions associated with the 2021 typhoon season. The La Niña event that started in 2020 returned to cool neutral ENSO conditions during the summer of 2021, but returned to La Niña conditions in August 2021 and strengthened through the end of the year to moderate conditions. The SST anomaly pattern during the peak typhoon season (JASO) was dominated by the standard eastern Pacific La Niña pattern, which includes above-normal SSTs in the western North Pacific near the Asian continent (Fig. 4.33a). The potential intensity (Emanuel 1988; Fig. 4.33b) had weak negative anomalies in the eastern part of the basin and positive anomalies closer to the Asian continent. With the exception of two bands of 600-hPa relative humidity anomalies (Fig. 4.33c) in the equatorial region (positive to the west, negative to the east), the mid-level relative humidity was close to climatological conditions.

The genesis potential index (GPI; Fig. 4.33d; Emanuel and Nolan 2004; Camargo et al. 2007b) is an empirical nonlinear index that describes regions of enhanced probability of TC formation,

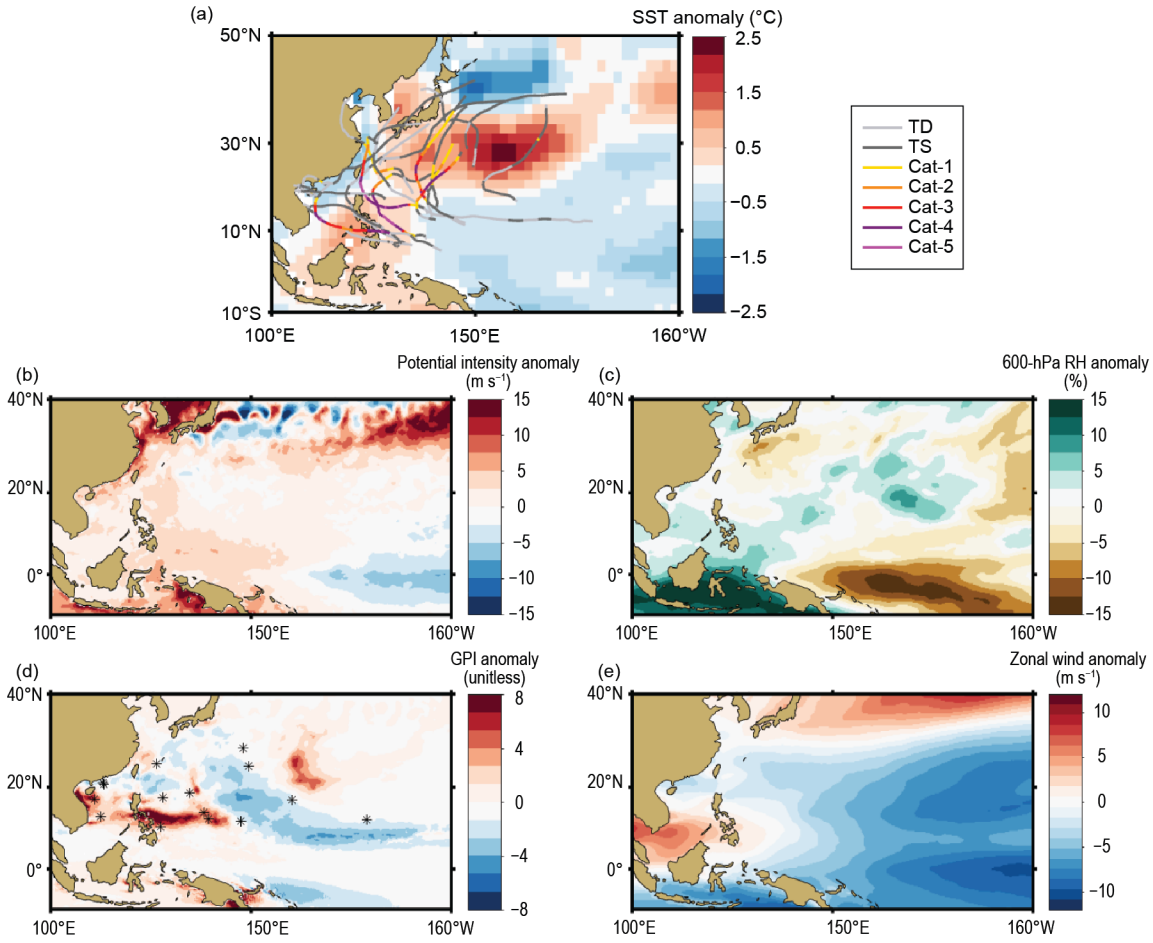

Fig. 4.33. Jul–Oct (JASO) 2021: (a) SST anomalies (°C) and the tracks of all 2021 storms with colors denoting their intensity, (b) potential intensity anomalies (m s^{-1}), (c) 600-hPa relative humidity anomalies (%), (d) genesis potential index (GPI) anomalies and first position of storms from JASO 2021 marked with an asterisk, and (e) zonal winds at 850-hPa (m s^{-1}). All anomalies are relative to their 1991–2020 climatologies. (Sources: SST: ERSSTv5 [Huang et al. 2017]; other environmental fields: ECMWF ERA5 reanalysis [Hersbach et al. 2020], tracks and first position: JTWC preliminary operational track data.)

based on four environmental fields: potential intensity, mid-level relative humidity, vertical wind shear, and low-level relative vorticity. In JASO 2021 was characterized by one region of positive anomalies, in the South China Sea and the Philippines, and a larger negative region to the east. The first position of the storms forming during those months is also shown in Fig. 4.33d (black asterisks), with TCs that formed located outside of the negative GPI anomaly region. The extent of the monsoon trough, defined by the 850-hPa zonal winds (Fig. 4.33e), was restricted from the South China Sea to the Philippines, as is typical in La Niña events, which would be reflected in the vorticity field of GPI. Tropical cyclone activity south of 30°N was restricted to the area close to the Philippines. The below-normal SST conditions and potential intensity in most of the basin, as well as the short extension of the monsoon trough, help explain the below-normal activity in the basin in 2021.

(iv) Tropical cyclone impacts

Including tropical depressions, 19 storms made landfall in 2021 (median = 17.5, 1961–2020 climatology). Landfall here is defined when the storm track is over land and the previous location was over the ocean. In order to include landfall over small islands, tracks were interpolated from 6-hour to 15-minute intervals, and a high-resolution land mask was used. In the case of multiple landfalls, we considered the landfall with the highest intensity for each storm. Eleven storms made landfall as tropical depressions (top quartile > 5), 5 as tropical storms (bottom quartile < 8), and 2 as typhoons (bottom quartile < 3): Cempaka and Super Typhoon Rai.

Rai (named Odette by PAGASA) caused the most severe and widespread damage, making nine landfalls in different locations in the southern Philippines, including as a Category 5 typhoon. More than 400 people were killed, and it was the third costliest typhoon in the Philippines history, causing $1 billion (U.S. dollars) in economic losses and damage (Aon 2022). The impacts were mainly caused by widespread flooding, which damaged or destroyed over a million houses and affected crops. The extent of the damage led the provinces of Cebu and Bohol to be placed into a state of calamity. The United Nations estimated that 13 million people were affected by the typhoon, which led to an international effort to assist the country.

5) NORTH INDIAN OCEAN BASIN—A. D. Magee and C. J. Schreck

(i) Seasonal activity

The North Indian Ocean (NIO) TC season typically occurs between April and December, with two peaks of activity: May–June and October–December, due to the presence of the monsoon trough over tropical waters of the NIO during these periods. Tropical cyclone genesis typically occurs in the Arabian Sea and the Bay of Bengal between 8°N and 15°N. The Bay of Bengal, on average, experiences four times more TCs than the Arabian Sea (Dube et al. 1997).

The 2021 NIO TC season had five named storms, three of which became cyclones, including one major cyclone (Extremely Severe Cyclonic Storm Tauktae). These numbers were all near the IBTrACS–JTWC 1991–2020 climatology of 5.5 named storms, 2.2 cyclones, and 1.1 major cyclones (Fig. 4.34).

While the number of storms was near-normal, the 2021 seasonal ACE index (January–December 2021) of 16.3×10^4 kt^2 was almost one-third less than the 1991–2020 mean of 24.7×10^4 kt^2 and over five times less than the record ACE of 93.0×10^4 kt^2 recorded in 2019. Indian Ocean dipole (IOD) conditions, as measured by the Dipole Mode Index, were positive during March and April and negative between May and July 2021 (section 4f). Environmental conditions during May were characterized by cooler SSTs in the western Arabian Sea and warmer SSTs in the Bay of Bengal (Fig. 4.35a). There was also a large area of enhanced convection in the Arabian Sea, present near the areas of cyclogenesis around Extremely Severe Super Cyclonic Storm Tauktae (Fig. 4.35b). Neutral/negative wind shear anomalies (Fig. 4.35c) were also present around the areas of cyclogenesis for both Extremely Severe Super Cyclonic Storm Tauktae and Very Severe Cyclonic Storm Yaas.

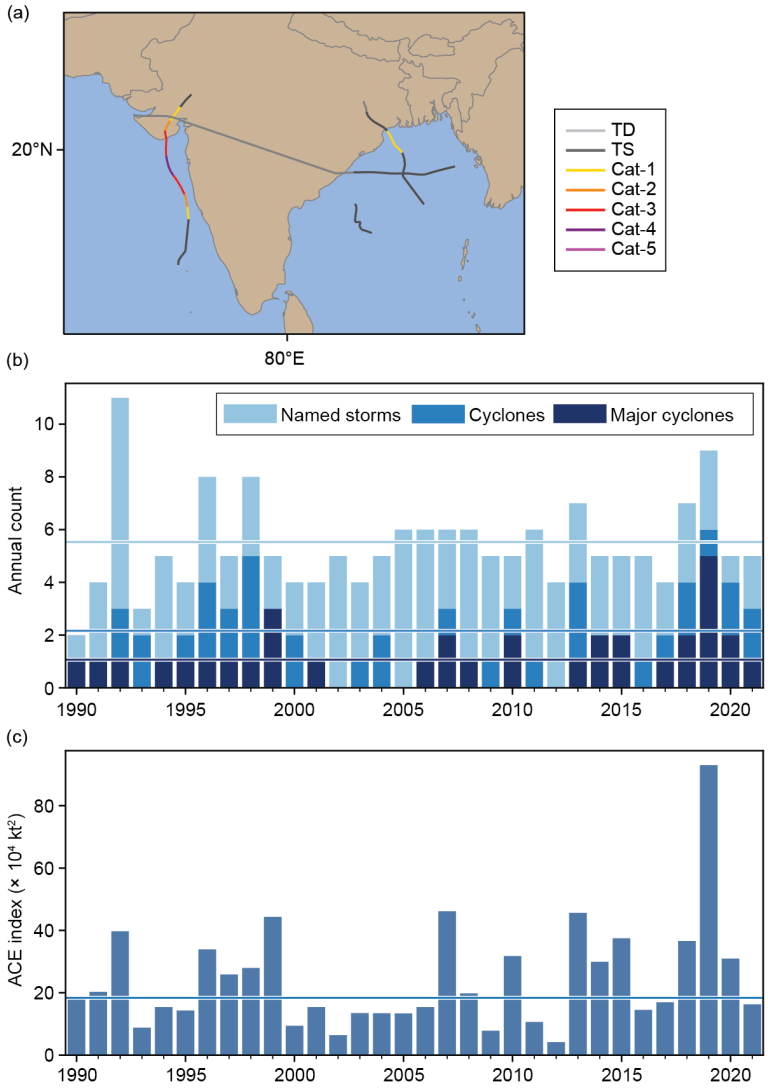

Fig. 4.34. Annual TC statistics for the NIO for 1990–2021: (a) storm tracks for 2021, (b) number of named storms, cyclones, and major cyclones, and (c) ACE (× 10^4 kt^2). Horizontal lines, representing the 1991–2020 climatology are included in both (b) and (c).

(ii) Individual tropical cyclones and impacts

Extremely Severe Super Cyclonic Storm Tauktae was the first cyclone of the 2021 season to form in the NIO basin. Initially forming from a depression off the Indian coast of Kerala in the Arabian Sea on 14 May, the low tracked towards the east and began to strengthen while tracking towards the north. On 15 May, Tauktae reached severe cyclonic storm status and continued to track parallel to the coastline of Kerala, Karnataka, Goa, and Maharashtra, eventually reaching peak intensity with maximum 1-minute sustained winds of 119 kt (61 m s^{-1}) and a minimum central pressure of 935 hPa on 17 May, equivalent to a SSHWS Category 4 system. Shortly after, Cyclone Tauktae underwent an eyewall replacement cycle resulting in a temporary reduction in intensity before it re-intensified and made landfall on the Gujarat coastline. In total, 174 deaths were reported, with a further 80 people reported missing. A number of fishing vessels and fishermen were lost at sea due to the substantial storm surge associated with this event. Cyclone Tauktae brought heavy rainfall and flash flooding across Gujarat, causing significant damage to infrastructure and agriculture. In Vijapadi, a village near to where Tauktae made landfall, most houses were destroyed by the cyclone. Wave heights in excess of four meters were reported off the coast of Gujarat. Impacts were also reported in neighboring Pakistan, where strong winds resulted in a number of roof and wall collapse incidents.

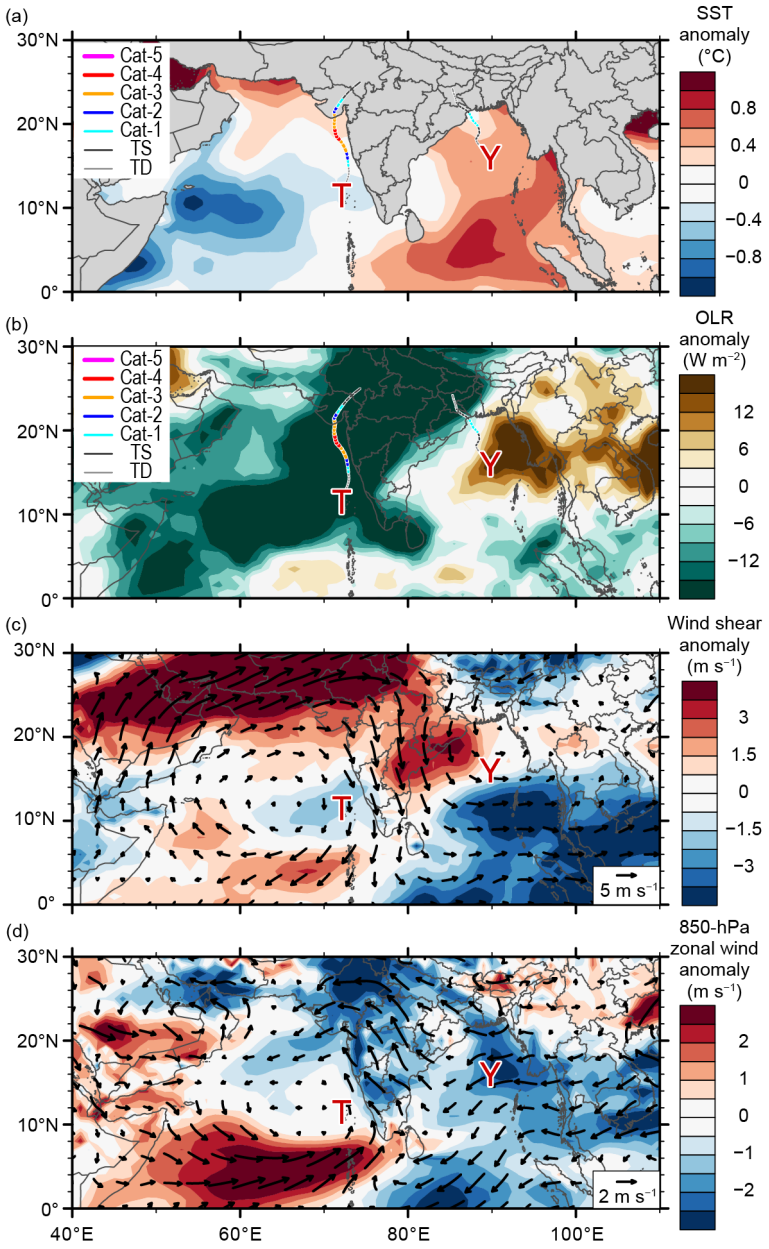

Fig. 4.35. May 2021 NIO anomaly maps of (a) SST (°C; Banzon and Reynolds, 2013), (b) OLR (W m^{-2}; Schreck et al. 2018); (c) 200–850-hPa vertical wind shear (m s^{-1}) vector (arrows) and scalar anomalies (shading), and (d) 850-hPa winds (m s^{-1}, arrows) and zonal wind anomalies (shading). Anomalies are relative to the annual cycle from 1991–2020. Letter symbols denote where each NIO TC attained its initial tropical storm intensity. (Source: Wind data from CFSR [Saha et al. 2014].)

Very Severe Cyclonic Storm Yaas formed from a low-pressure system in the Bay of Bengal. Favorable environmental conditions and anomalously high SSTs promoted intensification, and the system tracked in a northwesterly direction towards the coastline of northern Odisha. Yaas achieved its peak intensity with maximum sustained winds of 64 kt (33 m s^{-1}) and a minimum central pressure of 974 hPa on 25 May as it made landfall on the northern Odisha coastline of India. Impacts associated with Cyclone Yaas resulted in 20 fatalities and widespread destruction across India, Bangladesh, and Nepal. Over 1000 villages in West Bengal were submerged by floodwaters, and strong winds uprooted trees and snapped palm trees along the coast. Widespread and prolonged rainfall also resulted in flooding of farmland in West Bengal and Odisha. Storm surge generated by Cyclone Yaas impacted low-lying coastal communities in Bangladesh, resulting in the inundation of several villages. The Sundarbans were also inundated with seawater.

Cyclones Gulab and Shaheen were related tropical cyclones that occurred consecutively and in quick succession. Cyclone Gulab, the third named cyclone of the 2021 NIO TC season, formed

from a low-pressure system over the Bay of Bengal. Favorable SSTs and wind shear, along with an active pulse of the MJO (section 4c), assisted with the organization of Gulab, which followed a westerly trajectory towards northern Andhra Pradesh, India. Cyclone Gulab made landfall on 26 September, with maximum sustained winds of 39 kt (20 m s^{-1}) and a minimum central pressure of 983 hPa. Gulab continued to track over the Indian subcontinent and began to decay, eventually weakening to an area of low pressure near west Vidarbha. In the Arabian Sea, favorable environmental conditions, including SSTs up to 31°C, enabled the regeneration of the system, named Cyclone Shaheen, which continued to track towards the west.

On 3 October, Cyclone Shaheen achieved peak intensity with maximum sustained winds of 70 kt (36 m s^{-1}) and a minimum central pressure of 975 hPa, a Category 1 TC on the SSHWS. Shortly after, Cyclone Shaheen made landfall over the northern coast of Oman. In Oman alone, 14 people were killed, and many locations recorded a year's worth of rain in less than 24 hours, causing coastal and inland flooding. This flooding forced many people to seek shelter from the rising water on their roofs. Dams reportedly overflowed, and intense and prolonged rainfall resulted in numerous landslides across Oman. Widespread power outages were reported across the country. Impacts were also reported in Iran, the United Arab Emirates, and Yemen. The trajectory of Cyclones Gulab and Shaheen, from the Bay of Bengal, across the Indian subcontinent, and across the Arabian Sea into the Gulf of Oman, is a relatively infrequent occurrence. This track path has only been observed twice previously (1981 and 1959).

6) SOUTH INDIAN OCEAN BASIN—A. D. Magee and C. J. Schreck

(i) Seasonal activity

The South Indian Ocean TC basin extends south of the equator and from the African coastline to 90°E. While the SIO TC season extends year-round, from July to June, most TC activity typically occurs between November and April when the Intertropical Convergence Zone is located in the SH. The 2020/21 season includes TCs that occurred from July 2020 to June 2021. Landfalling TCs typically impact Madagascar, Mozambique, and the Mascarene Islands, including Mauritius and La Réunion; however, impacts can be felt in other locations within the region. Above-average storm activity was observed in the SIO basin with 12 named storms, compared to the IBTrACS-JTWC 1991–2020 mean of 10.5 (Fig. 4.36). The 5 cyclones were near-average (6.1), while the 2 major cyclones were below average (3.5). January 2021 was a particularly active month with three named cyclones (Danilo, Joshua, and Eloise) occurring within the basin.

The 2020/21 seasonal ACE index was 99.8×10^4 kt^2, which is near the 1991–2020 climatology of 94.4×10^4 kt^2. Cyclone-favorable conditions, including anomalously high SSTs (Fig. 4.37a), large areas of enhanced convection (< –12 W m^{-2}; Fig. 4.37b) in the eastern part of the basin (Fig. 4.37a), anomalously weak wind shear (Fig. 4.37c), and low-level westerly anomalies (Fig. 4.37d) were present in the main development region east of 70°E.

(ii) Noteworthy TCs and impacts

Severe Tropical Storm Chalane was the first storm of the season to make landfall, and did so across Madagascar and then Mozambique. Favorable environmental conditions enabled the cyclone to intensify while the system tracked in a westerly direction towards Madagascar. On approach to Madagascar, Chalane encountered strong wind shear, resulting in a temporary deterioration of the system prior to its landfall on 26 December in Mahavelona, Madagascar. The storm tracked towards the southwest over Madagascar as a surface trough and entered the Mozambique Channel on 28 December. Chalane intensified and gained severe tropical storm status with maximum sustained winds of 60 kt (31 m s^{-1}) and a minimum central pressure of 990 hPa—a tropical storm event on the SSHWS. On 30 December, Chalane made landfall near Beira, Mozambique, with flooding due to prolonged rainfall claiming seven lives. In Madagascar,

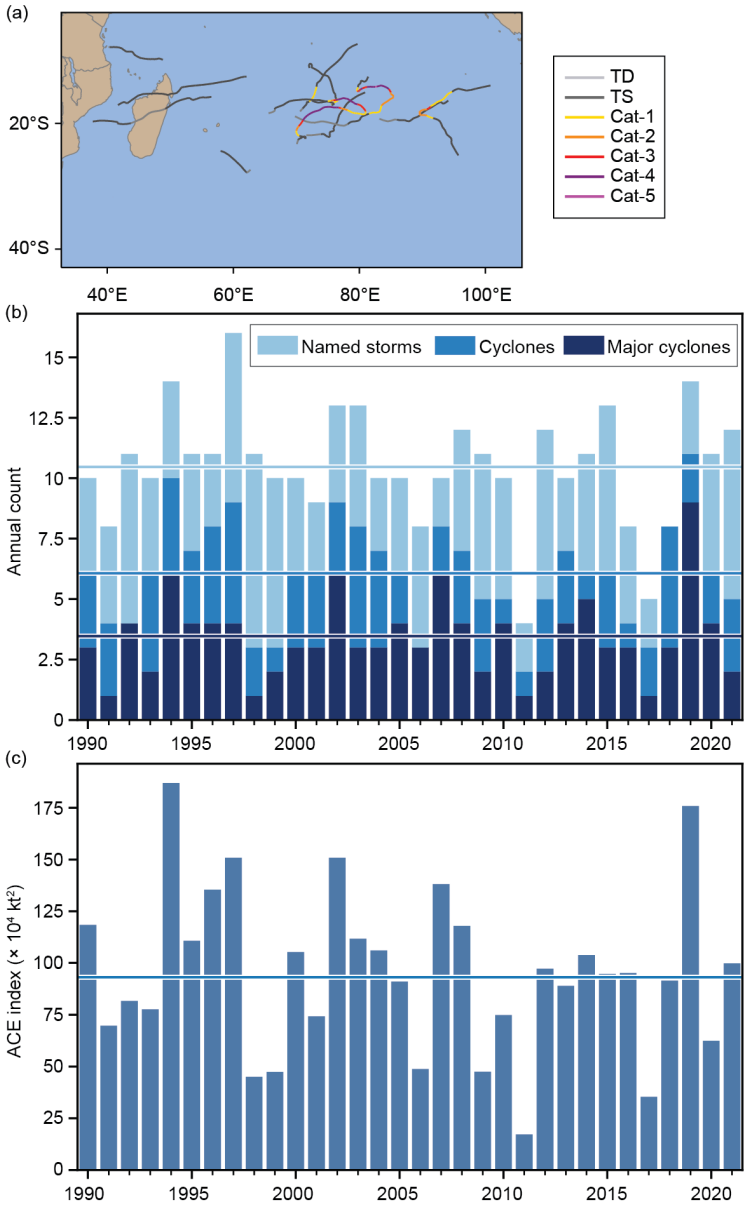

Fig. 4.36. Annual TC statistics for the SIO for 1990–2021: (a) storm tracks for 2021, (b) number of named storms, cyclones, and major cyclones, and (c) ACE (× 10^4 kt^2). Horizontal lines, representing the 1991–2020 climatology, are included in both (b) and (c). Note that the preliminary data for Tropical Cyclone Guambe were corrupted. It has been included in the counts, but it is missing from the track maps.

351 mm of rainfall was recorded in a 24-hour period at Toamasina. Impacts were also reported in Zimbabwe and Namibia.

Severe Tropical Storm Eloise, the third of three storms to form in January 2021, developed from an area of disturbed weather across the central South Indian Ocean. Eloise tracked to the southwest toward Madagascar and continued to intensify, reaching a peak intensity of 51 kt (26 m s^{-1}) and minimum central pressure of 994 hPa on 18 January, equivalent to a tropical storm event on the SSHWS. Eloise made landfall in Antalaha, Madagascar, on 19 January, and similar to Severe Tropical Storm Chalane, re-emerged into the Mozambique Channel after weakening upon landfall and tracking towards the southwest. Eloise made landfall north of Beira, Mozambique, and caused extreme flooding and unusually wet conditions in the weeks before Eloise made landfall. Eloise resulted in 27 confirmed fatalities across Madagascar, Mozambique, Zimbabwe, South Africa, and Eswatini.

Very Intense Tropical Cyclone Faraji, the only Category 5 (SSHWS) event to occur in the basin during the 2020/21 SIO TC season, developed from a well-defined surface circulation on 4 February

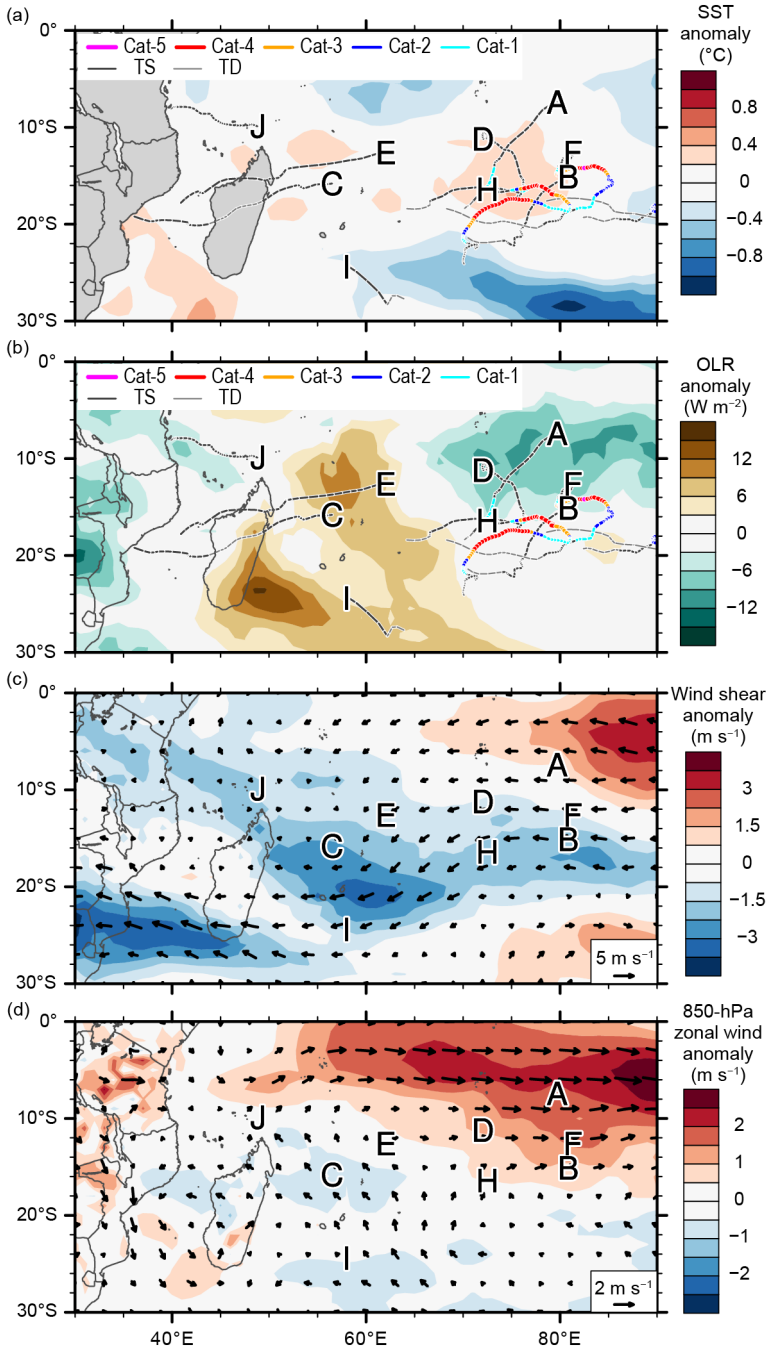

Fig. 4.37. Nov 2020–Apr 2021 SIO anomaly maps of (a) SST (°C; Banzon and Reynolds 2013), (b) OLR (W m^{-2}; Schreck et al. 2018); (c) 200–850-hPa vertical wind shear (m s^{-1}) vector (arrows) and scalar anomalies (shading), and (d) 850-hPa winds (m s^{-1}, arrows) and zonal wind anomalies (shading). Anomalies are relative to the annual cycle from 1991 to 2020. Letter symbols denote where each SIO TC attained its initial tropical storm intensity. (Source: Wind data from CFSR [Saha et al. 2014].)

near the Chagos Archipelago. After tracking towards the south, Faraji rapidly intensified to a Category 4 system before weakening slightly, caused by cooler SSTs due to upwelling. As Faraji tracked towards the east, favorable environmental conditions enabled intensification to reach a peak intensity of 138 kt (71 m s^{-1}) and a minimum central pressure of 920 hPa on 8 February (a Category 5 system on the SSHWS). Faraji subsequently weakened as it turned towards the south and then tracked towards the west, where it decayed. Faraji did not make landfall and no significant damage was reported.

Tropical Cyclone Guambe, the third tropical cyclone of 2021 to make landfall across Mozambique, initially developed as a disturbance in the Mozambique Channel. Guambe made landfall near Inhambane close to where Severe Tropical Storm Eloise had made landfall weeks earlier.

After moving inland and delivering prolonged and intense rainfall, the system tracked towards the northeast and re-entered the Mozambique Channel, where the system then tracked towards the south. The system continued to intensify and reached a peak intensity of 54 kt (28 m s^{-1}) and a minimum central pressure of 980 hPa on 22 February, equivalent to a tropical storm on the SSHWS. No fatalities were reported, but damage was reported in Madagascar, Mozambique, South Africa, and Eswatini.

Moderate Tropical Storm Iman initially formed from a weak tropical disturbance in the Mozambique Channel. Iman continued to organize and strengthen as a tropical depression where it made landfall on the west coast of Madagascar on 5 March. The system emerged into the South Indian Ocean and continued to track towards the southeast as it strengthened to achieve tropical storm intensity on the SSHWS, with maximum intensity of 45 kt (23 m s^{-1}) and a minimum central pressure of 991 hPa on 7 March. Although Iman did not make landfall on La Reunion, intense thunderstorms associated with the system did impact the island. Intense rainfall, wind, and lightning resulted in widespread loss of power on La Reunion and flooding in Saint-Denis.

The last named storm of the season, Severe Tropical Storm Jobo, formed from a zone of disturbed weather to the east of the Chagos Archipelago. The system tracked towards the west and reached a maximum intensity of 55 kt (28 m s^{-1}) and a minimum central pressure of 995 hPa on 21 April (equivalent to a tropical storm on the SSHWS), as the system passed approximately 200 km to the north of Madagascar. Jobo continued to track towards the northwest, and the system was downgraded to a remnant low before making landfall on the coast of Tanzania. Extreme wind associated with Jobo resulted in damage to some of the outer islands of the Seychelles, and 22 deaths were reported across the Seychelles, northern Madagascar, and Tanzania.

7) AUSTRALIAN BASIN—B. C. Trewin

(i) Seasonal activity

The 2020/21 TC season was close to normal for the broader Australian basin (areas south of the equator and between 90°E and 160°E,[5] which includes Australian, Papua New Guinea, and Indonesian areas of responsibility). The 1991–2020 IBTrACS seasonal averages for the basin are 10.2 named storms, 5.0 TCs, and 2.5 major TCs, which compares with the 2020/21 counts of 12, 3, and 2, respectively (Fig. 4.38; Table 4.2), but four of the 2020/21 storms were too weak to be classified as named storms by the Australian Bureau of Meteorology. Weak-to-moderate La Niña conditions were present during the 2020/21 season, which are historically associated with increased TC occurrence in the Australian region.

There were four named TCs in the western sector[6] of the broader Australian region during 2020/21, none in the northern sector, and four in the eastern sector. Two systems made landfall in Australia as TCs: one in Western Australia and one in the Gulf of Carpentaria.

(ii) Landfalling and other significant TCs

The most significant tropical cyclone in the region in 2020/21, in terms of impact, was Seroja. Seroja's precursor low formed near the southwestern end of the island of Timor on 3 April. The precursor low brought extremely heavy rain, with Kupang, in western Timor, receiving 551 mm total during 1–4 April, including 460 mm on the 3rd and 4th alone.

After having been nearly stationary for two days, the low reached cyclone intensity on 5 April. It commenced moving west to southwest, parallel to and several hundred kilometers to the northwest of the Western Australian coast, continuing on that track for several days to reach

[5] The Australian Bureau of Meteorology's warning area overlaps both the southern Indian Ocean and southwest Pacific.

[6] The western sector covers areas between 90°E and 125°E. The eastern sector covers areas east of the eastern Australian coast to 160°E, as well as the eastern half of the Gulf of Carpentaria. The northern sector covers areas from 125°E east to the western half of the Gulf of Carpentaria. The western sector incorporates the Indonesian area of responsibility, while the Papua New Guinea area of responsibility is incorporated in the eastern sector.

21°S, 108°E on 10 April. Its turn towards the southeast, which had been delayed by a Fujiwara interaction (rare in the Australian region; https://glossary.ametsoc.org/wiki/Fujiwhara_effect) with Cyclone Odette, started at this point, as it accelerated towards the Western Australia coast over the following 36 hours. The storm intensified as it reached the coast, reaching severe Category 3 intensity and making landfall at about 28°S, just south of Kalbarri, at about 1200 UTC on 11 April, at near peak intensity (central pressure 971 hPa, maximum 10-minute sustained winds 65 kt [33 m s^{-1}]). A gust of 92 kt (47 m s^{-1}) was reported at Meanarra Tower, near Kalbarri. Seroja continued to move on a southeastern track inland and was downgraded to a tropical low near Merredin on 12 April. No severe cyclone had made landfall so far south since 1956. Cyclone Alby (1978) had major impacts on southwest Western Australia but did not make landfall.

At least 226 deaths were attributed to Seroja, almost all due to flooding and landslides from the precursor low. Indonesia reported 181 deaths, mostly in East Nusa Tenggara province on the islands of Flores and Timor, with 44 reported in Timor-Leste. One death occurred in Australia in storms associated with the Seroja-Odette circulation. According to Reliefweb (UN Office from Coordination of Humanitarian Affairs), this was the largest known loss of life from a tropical cyclone in the basin for more than 40 years, since the Flores cyclone in 1973 resulted in 1653 deaths (http://www.bom.gov.au/cyclone/nt/Unnamed_Flores_Sea.shtml). In Australia, there was severe wind damage near the landfall point, with an estimated 70% of the buildings in the towns of Kalbarri and Northampton significantly damaged or destroyed. Building codes in this area are less stringent than in areas farther north, which are more frequently affected by tropical cyclones.

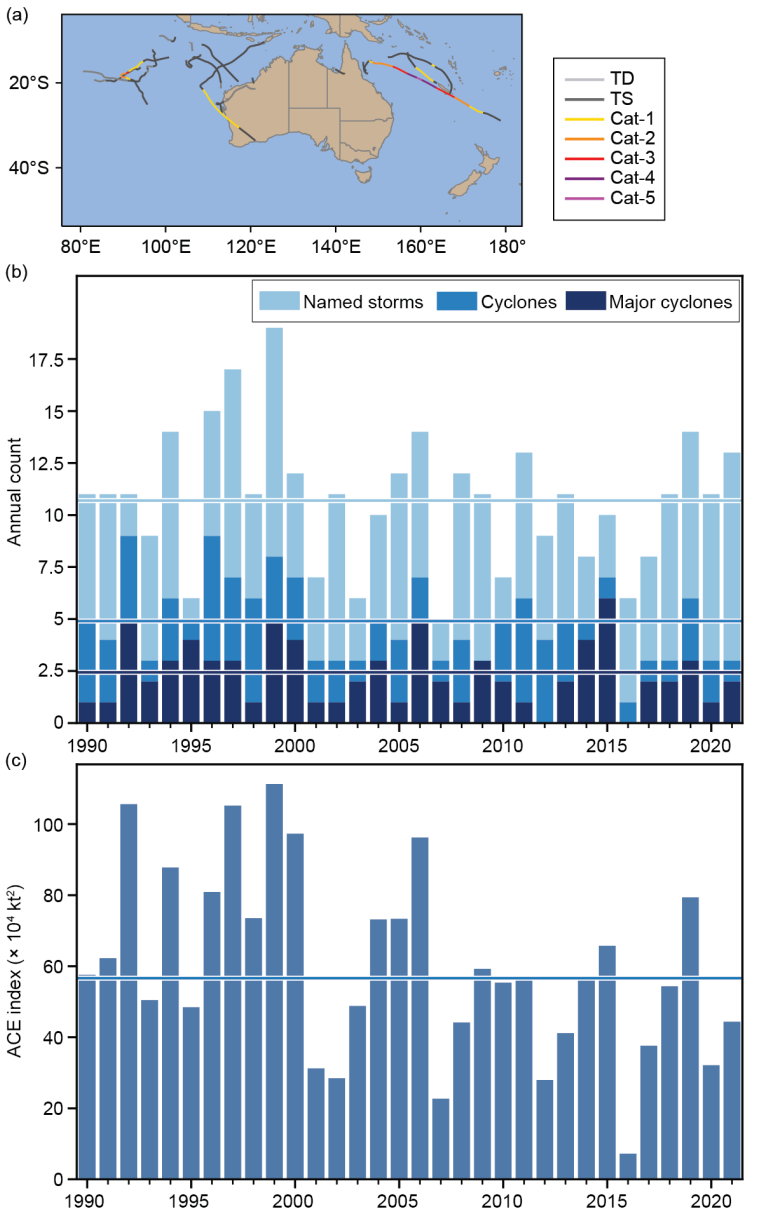

Fig. 4.38. Annual TC statistics for the Australian basin for 1990–2021: (a) storm tracks for 2021, (b) number of named storms, cyclones, and major cyclones, and (c) ACE (× 10^4 kt^2). The 1991–2020 means (horizontal lines) are included in both (b) and (c). Classifications are based on the SSHWS.

The most intense cyclone of the season in the region was Cyclone Niran, which formed off the coast of Queensland, reaching cyclone intensity on 2 March, before moving east and intensifying. The storm reached Category 5 intensity on 5 March near 19°S, 159°E, just before leaving the Australian region, with maximum sustained winds of 110 kt (56.6 m s^{-1}). The most significant impacts of Niran in Australia were from strong winds and heavy rain associated with its precursor low on 1–2 March. There were significant losses to crops, particularly bananas, in the Innisfail area. Niran went on to have substantial impacts in New Caledonia after leaving the Australian region (section 4g8).

Along with Seroja and Niran, the third severe cyclone of the season in the region was Marian, a long-lived system (26 February to 6 March), which remained well off the west coast of Australia and affected no land areas. Marian's peak intensity (maximum sustained winds 85 kt (43.7 m s^{-1}) was reached near 19°S, 90°E on 2 March.

Eastern Australia's only landfall of the season was Cyclone Imogen, a short-lived cyclone which made landfall as a Category 1 system on 3 January near Karumba on the east coast of the Gulf of Carpentaria, with maximum sustained winds of 45 kt (23.2 m s^{-1}). Imogen's major impacts resulted from heavy rain and flooding, although there was also some tree damage. Normanton received 262.6 mm of rain in the 24 hours to 0900 local time on 4 January, its heaviest 24-hour total since 1958, while Sweers Island received 222 mm on the 4th and 450 mm over the three days 2–4 January.

8) SOUTHWEST PACIFIC BASIN—A. D. Magee, A. M. Lorrey, H. J. Diamond, and J.-M. Woolley

(i) Seasonal activity

The 2020/21 Southwest Pacific TC season officially commenced in November 2020 and ended in April 2021. Best track data for 2020/21 were gathered from the Fiji Meteorological Service, Australian Bureau of Meteorology, and New Zealand MetService, Ltd. The Southwest Pacific basin (defined by Diamond et al. [2012] as 135°E–120°W) had nine TCs (based on the Australian TC Intensity Scale unless noted otherwise), including two severe (or major) TCs (based on the Australian TC intensity scale). Figure 4.39 shows the TC activity based on the basin spanning the area 160°E–120°W to avoid overlaps with the Australian basin that could result in double counting of storms; however, it is important to use the climatological definition of the Southwest Pacific basin (Diamond et al. 2012) instead of the more traditional political boundary.

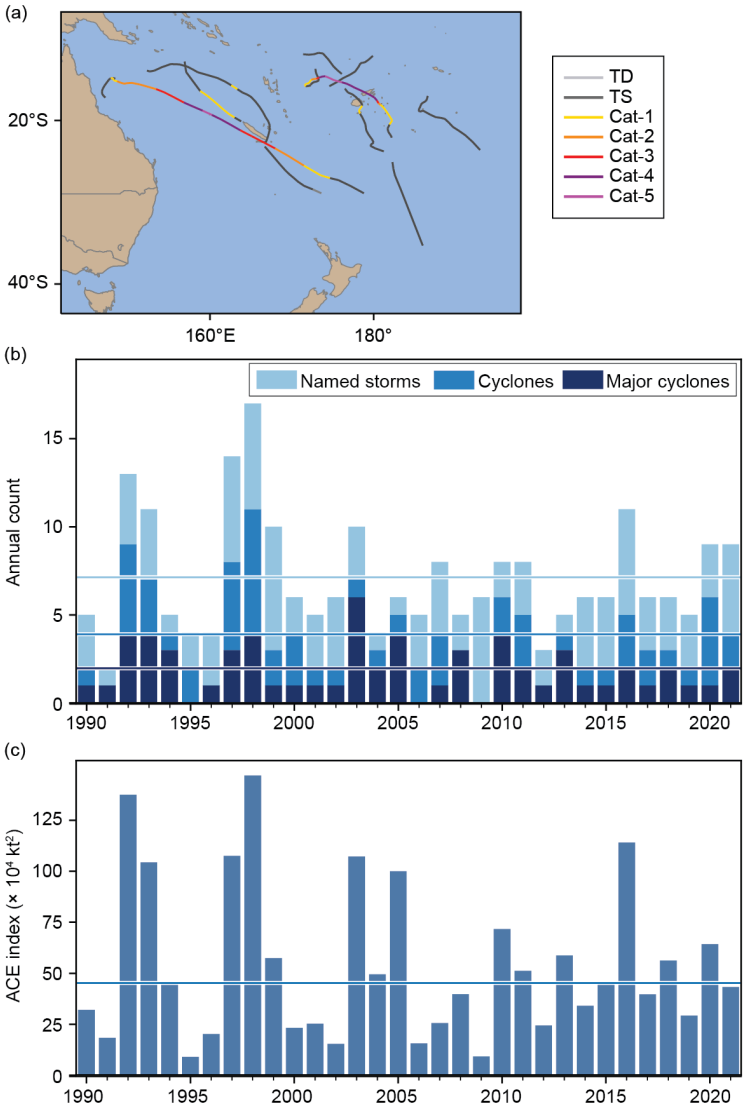

Fig. 4.39. Annual TC statistics for the Southwest Pacific for 1990–2021: (a) storm tracks for 2021, (b) number of named storms, cyclones, and major cyclones, and (c) ACE (× 10^4 kt^2). The 1991–2020 means (horizontal lines) are included in both (b) and (c). Classifications are based on the SSHWS.

The South Pacific Enhanced Archive of Tropical Cyclones (SPEArTC; Diamond et al. 2012) indicates a 1991–2020 seasonal average of 9.8 named TCs, including 4.3 severe (or major) TCs. Therefore, the 2020/21 TC season had near-normal activity with 8 named (and one unnamed) tropical cyclones, of which 3 were severe (Category 3 or above), as per Magee et al. (2022).

(ii) Storm tracks, landfalls, and impacts

Severe Tropical Cyclone Yasa was the first tropical cyclone and severe tropical cyclone of the 2020/21 Southwest Pacific tropical cyclone season. Developing from an area of low pressure north of Port Vila, Vanuatu, Yasa intensified to Category 1 status on 13 December 2020. Cyclone Yasa

underwent rapid intensification and after a slow loop northwest of Fiji, eventually tracked southeast towards Fiji, achieving Category 5 intensity on 16 December with peak 10-minute sustained winds of 125 kt (64 m s^{-1}) and a minimum central pressure of 917 hPa. Severe Tropical Cyclone Yasa made landfall over Vanua Levu, Fiji, and resulted in considerable widespread damage. Four lives were lost due to strong winds and flooding associated with the event. Since the beginning of reliable records, Yasa was the earliest Category 5 tropical cyclone (on both the Australian scale and SSHWS) in the basin.

Tropical Cyclone Zazu initially formed as a tropical disturbance approximately 500 km to the northeast of Niue. Favorable conditions promoted intensification and on 15 December, Cyclone Zazu achieved Category 2 status with peak 10-minute sustained winds of 50 kt (26 m s^{-1}) and a minimum central pressure of 980 hPa. Heavy surf associated with Zazu damaged a wharf on Niue, and strong winds caused minor damage in Tonga.

Tropical Cyclone Imogen originated from a tropical low that formed in the Gulf of Carpentaria under favorable conditions, including SSTs up to 31°C, which promoted intensification. On 3 January, Imogen was named and achieved Category 1 status, eventually achieving peak 10-minute sustained winds of 45 kt (23 m s^{-1}) and a minimum central pressure of 990 hPa. Cyclone Imogen was the first tropical cyclone of the 2020/21 Australian region TC season (section 4g7).

Tropical Cyclone Kimi formed from a weak tropical low to the northeast of Cooktown on 17 January. Kimi continued to track to the south and was expected to make landfall; however, a notable increase in wind shear caused the system to loop and quickly dissipate on 19 January. This short-lived and relatively compact system achieved Category 2 status with peak 10-minute sustained winds of 55 kt (28 m s^{-1}) and minimum central pressure of 987 hPa. Cyclone Kimi caused Townsville Airport to temporarily cease operations (between 18 and 19 January) and resulted in considerable rainfall and flash flooding with 24-hour accumulated rainfall of 158 mm at Innisfail.

Severe Tropical Cyclone Ana developed from a tropical disturbance that formed approximately 200 km to the northeast of Port Vila, Vanuatu. Initially tracking to the east and then southeast, Ana gradually intensified and achieved Category 1 intensity on 29 January, approximately 350 km to the northwest of Nadi, Fiji. Tracking towards the southeast, Cyclone Ana passed through the northern Yasawa Islands, where it continued to intensify, making landfall near Rakiraki, Fiji, on 31 January. Near Kadavu Island, Severe Tropical Cyclone Ana achieved Category 3 intensity with peak 10-minute sustained winds of 65 kt (33 m s^{-1}) and minimum central pressure of 970 hPa. Ana rapidly weakened to a subtropical low on 1 February and continued to track towards the southeast. On approach to Fiji, Severe Tropical Cyclone Ana caused significant flooding in Nadi and Rakiraki, and considerable damage was reported in Suva after landfall. Five people were reported missing with one confirmed fatality. This event prompted a humanitarian aid response as the region was still recovering from Severe Tropical Cyclone Yasa, a Category 5 event, one month prior.

Tropical Cyclone Bina developed from an east-northeastward tracking TD that initially developed approximately 700 km northeast of Port Vila. Favorable environmental conditions promoted intensification to a Category 1 tropical cyclone on 31 January with peak 10-minute sustained winds of 45 kt (23 m s^{-1}) and a minimum central pressure of 991 hPa. Bina tracked in a southeasterly direction towards Vanua Levu, Fiji, where it was downgraded to a TD on 1 February. Although the event made landfall over Vanua Levu as a TD, it did so within 24 hours of Severe Tropical Cyclone Ana, prolonging the gale force winds and rainfall.

Tropical Cyclone Lucas originated from a tropical low formed from a monsoon trough in the Gulf of Carpentaria. Tracking towards the east over the Cape York Peninsula and then towards the southwest, Lucas eventually intensified to a Category 2 system, achieving peak 10-minute sustained winds of 60 kt (31 m s^{-1}) and a minimum central pressure of 975 hPa. Cyclone Lucas made landfall on New Caledonia on 2 February and resulted in damage to power infrastructure and power outages across the Loyalty Islands, as well as contamination of drinking water supplies.

Severe Tropical Cyclone Niran, the third severe TC and second Category 5 TC for the season, initially formed off the coast of northern Queensland and was named on 1 March (see section 4g7) while tracking towards the southwest. Niran intensified to a Category 5 system on 5 March on approach to New Caledonia, achieving peak 10-minute sustained winds of 110 kt (57 m s^{-1}) and a minimum central pressure of 931 hPa. Unfavorable wind shear weakened the system to a Category 3 event before it passed close to the southern coastline of New Caledonia.

h. Tropical cyclone heat potential—F. Bringas, G. J. Goni, I-I Lin, and J. A. Knaff

Tropical cyclone heat potential (TCHP; e.g., Goni et al. 2009, 2017) is an indicator of the available heat stored in the upper ocean that can potentially induce tropical cyclone (TC) intensification and regulate ocean–atmosphere enthalpy fluxes and TC-induced sea surface temperature (SST) cooling (e.g., Lin et al. 2013). TCHP is calculated as the integrated heat content between the sea surface and the 26°C isotherm (D26), which is generally taken to be the minimum temperature required for TC genesis and intensification (Leipper and Volgenau 1972; Dare and McBride 2011).

Provided that atmospheric conditions are favorable, TC intensification, including rapid intensification, has been associated with areas in the ocean that have TCHP values above 50 kJ cm^{-2} (e.g., Shay et al. 2000; Mainelli et al. 2008; Lin et al. 2014; 2021; Knaff et al. 2018, 2020). High SSTs prior to TC formation usually lead to less SST cooling during the lifetime of the TC, and hence higher enthalpy fluxes from the ocean into the storm, favoring intensification (e.g., Lin et al. 2013). Similarly, upper ocean salinity is another condition of relevance for TC intensification because fresh water-induced barrier layers may also modulate the upper ocean mixing and cooling during a TC, and hence the air–sea fluxes (e.g., Balaguru 2012; Domingues et al. 2015). Upper ocean thermal conditions observed during 2021 are presented here in terms of two parameters: (1) TCHP anomaly values with respect to their long-term mean (1993–2020) and (2) TCHP anomaly values compared to conditions observed in 2020. TCHP anomalies during 2021 (Fig. 4.40) are computed for June–November in the Northern Hemisphere and November 2020–April 2021 in the Southern Hemisphere. In Fig. 4.40, the seven regions where TCs are known to form, travel, and intensify are highlighted. In all of these regions, TCHP values exhibit large temporal and spatial variability due to mesoscale features, trends, and short- to long-term modes of variability, such as the North Atlantic Oscillation (NAO), El Niño-Southern Oscillation (ENSO), and the Pacific Decadal Oscillation (PDO). The differences in TCHP anomalies between 2020 and 2021 are also computed for the primary months of TC activity in each hemisphere (Fig. 4.41).

During the 2021 season, TCHP exhibited above-average values across most basins (Fig. 4.40). TCHP anomalies above 30 kJ cm^{-2} were observed in areas within several regions, including the North Indian Ocean, southeast Indian Ocean, western Pacific Ocean, and the Gulf of Mexico. These positive anomalies may be indicative of favorable oceanic conditions during 2021 for TC development and intensification. Compared to 2020, TCHP anomalies in 2021 were higher in the southeast Indian Ocean, southwest Pacific, and part of the Gulf of Mexico basin, while the anomalies were lower in the rest of the basins (Fig. 4.41). In particular, TCHP anomalies during 2021 were lower than those in 2020 and below the long-term average in the eastern North Pacific basin, linked to the negative phase of ENSO (La Niña) that re-emerged in August 2021.

In the Southern Hemisphere, TCHP during 2021 was mostly above the long-term average, with values of more than 30 kJ cm^{-2} in the southeast Indian Ocean and ~10 kJ cm^{-2} in the southwest Indian Ocean (Fig. 4.40). TCHP was more than 20 kJ cm^{-2} higher than 2020 values in the southeast Indian Ocean and southwest Pacific, while they were 20 kJ cm^{-2} lower in areas of the southwest Indian Ocean (Fig. 4.41). The 2020/21 cyclone season in the southwest Indian Ocean was above average and produced seven TCs of Category 1 or above intensity, including Very Intense TC Faraji (Category 5; section 4g6). Ocean conditions with high TCHP anomalies in the southeast Indian Ocean and southwest Pacific around Australia translated, however, to a below-average but deadly season with five TCs, including Severe TC Seroja and Category 5 Niran (section 4g8), the most

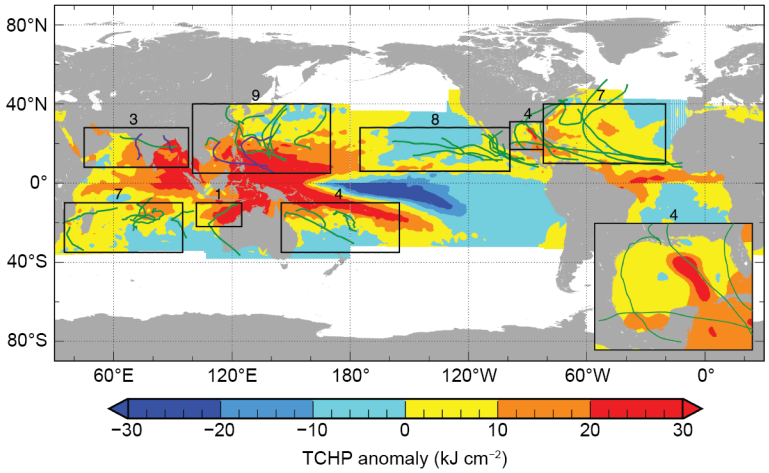

Fig. 4.40. Global anomalies of TCHP (kJ cm^{-2}) during 2021 computed as described in the text. The boxes indicate the seven regions where TCs occur: from left to right, southwest Indian, North Indian, northwest Pacific, southeast Indian, South Pacific, East Pacific, and North Atlantic (shown as Gulf of Mexico and tropical Atlantic separately). The green lines indicate the trajectories of all tropical cyclones reaching at least Category 1 (1-min average wind ≥ 64 kt, 34 m s^{-1}) and above during Nov 2020–Apr 2021 in the Southern Hemisphere and Jun–Nov 2021 in the Northern Hemisphere. The purple lines indicate the trajectories of tropical cyclones Category 1 or stronger in the Northern Hemisphere that occurred outside the Jun–Nov 2021 period. The numbers above each box correspond to the number of Category 1 and stronger cyclones that travel within each box. The Gulf of Mexico conditions are shown in the inset in the lower right corner.

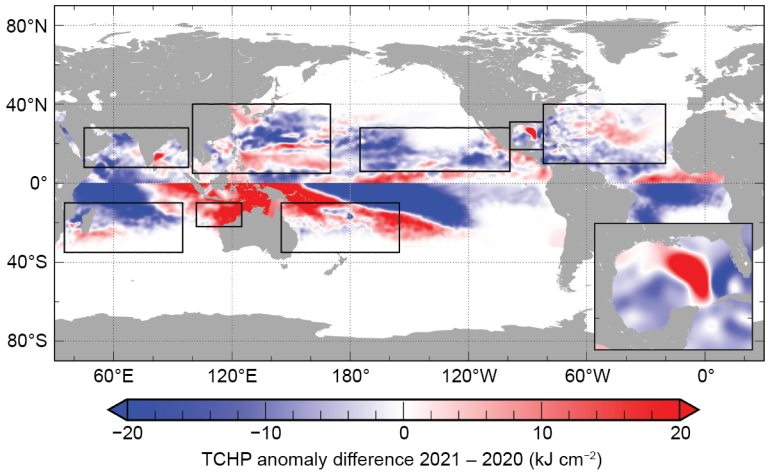

Fig. 4.41. TCHP anomaly difference (kJ cm^{-2}) between the 2021 and 2020 tropical cyclone seasons (Jun–Nov in the Northern Hemisphere and Nov–Apr in the Southern Hemisphere). The Gulf of Mexico conditions are shown in the inset in the lower right corner.

intense storm of the region for this season. Anomalously high values of TCHP in the Coral Sea were partially responsible for Niran's slow, but steady, development just off the coast of Queensland while being nearly stationary and noticeably affected by vertical wind shear on 2–3 March, followed by its rapid intensification that commenced once the storm began to move on 4 March.

The North Indian Ocean was characterized by above-average TCHP during 2021, with anomalies in excess of 30 kJ cm^{-2} in the Bay of Bengal (Fig. 4.40); however, these values were lower than those observed the previous year (Fig. 4.41). Three Category 1 or stronger TCs occurred in the region (Fig. 4.40), two of which occurred in May and are shown in Fig. 4.40 as purple lines. The most intense TC in this basin during 2021 was Extremely Severe TC Tauktae in May (section 4g5), with peak intensity of 3-minute sustained wind speed of 100 kt (51 m s^{-1}) and minimum pressure of 950 hPa. TCHP values exceeding 140 kJ cm^{-2} over the southeast Arabian Sea were cited as a contributing environmental factor, noting values were lower but exceeding 50 kJ cm^{-2} along the storm track (IMD 2021).

Upper ocean thermal conditions are largely modulated by the state of ENSO in the North Pacific (e.g., Lin et al. 2014, 2020; Zheng et al. 2015). During 2021, La Niña was observed from August to the end of the year. This is similar to 2020, in which a stronger La Niña (compared to 2021) was observed during August 2020 to May 2021. As is typical during a La Niña year, TCHP was above average in the western North Pacific (Lin et al. 2014, 2020), with anomalies well above 30 kJ cm^{-2} closer to the equator and average anomalies of ~20 kJ cm^{-2} throughout the region compared to the long-term average (Fig. 4.40). Compared to 2020, TCHP in the western North Pacific displayed both negative and positive anomalies, possibly associated with the difference in the La Niña characteristics of these two years. TCHP anomalies were slightly negative compared to average in the eastern North Pacific and moderately negative compared to 2020 (Fig. 4.41). Category 5 Super Typhoon Surigae was the most intense storm both in the western North Pacific and globally in 2021. Interestingly, it occurred

in April (i.e., boreal spring) and not summer and is therefore shown in Fig. 4.40 as a purple track line. TCHP observations show that Surigae intensified to 165 kts (85 m s^{-1}) peak intensity over a region of high TCHP of ~120–140 kJ cm^{-2}, ~30 kJ cm^{-2} higher than the long-term mean for April. Another notable western North Pacific Category 5 TC was Super Typhoon Chanthu, which intensified to its peak intensity of 155 kts (80 m s^{-1}) in September, when traveling over the Kuroshio warm current region south of Taiwan, where high TCHP values of ~130 kJ cm^{-2} were observed.

In the North Atlantic basin, upper ocean thermal conditions during the 2021 hurricane season were characterized by TCHP values moderately above the long-term average, with anomalies between +10 and +20 kJ cm^{-2} (Fig. 4.40) but as much as 10 kJ cm^{-2} lower than the previous year in the regions where most TCs form and intensify in this basin (Fig. 4.41). An exception was the area associated with the location of the northern extension of the Loop Current in the Gulf of Mexico, where TCHP anomalies were more than 30 kJ cm^{-2} higher than the long-term average and more than 20 kJ cm^{-2} higher than the values of 2020. Consistent with the higher-than-average TCHP anomalies, 2021 was the third most active Atlantic hurricane season on record with 21 named storms, including seven hurricanes at Category 1 or above intensity.

During 2021, Hurricanes Grace and Ida reached their peak intensities, corresponding to Category 3 and 4 storms, respectively. The genesis of Hurricane Grace started off Cabo Verde on 10 August. The system continued to organize and became a named tropical storm on 14 August, reaching Category 1 when traveling in the Caribbean Sea. After the storm moved offshore from the Yucatan Peninsula into the southwest region of the Gulf of Mexico, Grace underwent rapid intensification on 23 August from Category 1 to Category 3 in a 15-hour period while moving over an area with SST > 28°C and TCHP > 60 kJ cm^{-2}, above the 50-kJ cm^{-2} threshold required to support Atlantic hurricane intensification (Mainelli et al. 2008). Hurricane Ida, the second most intense Atlantic storm in 2021, reached Category 1 when traveling on 26–27 August over an area in the Caribbean Sea with favorable ocean conditions, including TCHP values of more than 120 kJ cm^{-2} and extensive areas of low salinity surface layers associated with the Amazon and Orinoco riverine plumes, observed by underwater gliders deployed in the region (https://www.aoml.noaa.gov/hurricane-glider-project). Low-surface salinity areas create barrier layer conditions that reduce upper-ocean turbulent mixing and maintain high enthalpy fluxes from the ocean into the hurricane, therefore contributing to TC organization and intensification (e.g., Balaguru et al. 2015; Domingues et al. 2015). After traveling over the western portion of Cuba and entering the Gulf of Mexico, Ida moved over a region of increasingly favorable ocean conditions over the main location of the northern extension of the Loop Current, the same area where the largest TCHP anomalies in the North Atlantic and Gulf of Mexico basins occurred (Fig. 4.40). These favorable conditions contributed to Ida's intensification, including rapid intensification reaching Category 4 on 29 August with peak intensity of 1-minute sustained wind speeds of 130 kt (67 m s^{-1}) and a minimum central barometric pressure of 929 hPa, after traveling over a warm region with TCHP > 140 kJ cm^{-2} associated with a strong anticyclonic eddy that was shed by the Loop Current.

In summary, favorable upper-ocean thermal conditions were observed in all seven basins during the 2021 season, except in the eastern North Pacific, where conditions were average to slightly below average compared to the long-term mean. Additionally, TCHP anomaly values during 2021 exhibited similar to lower values in most regions compared to the previous year in most basins.

Acknowledgments

Our thanks go out to Gregory Carbin, Alex Lamers, and David Novak, of NOAA's Weather Prediction Center for assisting us with re-constructing a key precipitation graphic in Sidebar 4.1 on the Hurricane Ida story.

Appendix 1: Chapter 4 – Acronyms

ACE	Accumulated Cyclone Energy
AEJ	African Easterly Jet
AMO	Atlantic multi-decadal oscillation
ASO	August–October
CNP	central North Pacific
CPC	Climate Prediction Center
DJF	December–February
EASM	East Asian summer monsoon
ENP	eastern North Pacific
ENSO	El Niño–Southern Oscillation
GPCP	Global Precipitation Climatology Project
GPI	genesis potential index
HTCs	hurricanes/typhoons/cyclones
IBTrACS	International Best Track Archive for Climate Stewardship
IO	Indian Ocean
IOB	Indian Ocean basin
IOD	Indian Ocean dipole
ITCZ	Intertropical Convergence Zone
JAS	July–September
JASO	July–October
JJA	June–August
JMA	Japan Meteorological Agency
JTWC	Joint Typhoon Warning Center
MAM	March–May
MDR	main development region
MJO	Madden-Julian oscillation
NAF	northern Africa
NH	Northern Hemisphere
NIO	North Indian Ocean
nIOD	Negative Indian Ocean dipole
OLR	outgoing longwave radiation
OND	October–December
ONI	Oceanic Niño Index
PAGASA	Philippine Atmospheric, Geophysical and Astronomical Services Administration
RMM	Real-time Multivariate
RSMCs	Regional Specialized Meteorological Centers

SAM	Southern Annular Mode
SH	Southern Hemisphere
SON	September–November
SPCZ	South Pacific Convergence Zone
SPEArTC	South Pacific Enhanced Archive of Tropical Cyclones
SSHWS	Saffir-Simpson Hurricane Wind Scale
SST	sea surface temperature
std. dev.	standard deviation
TC	tropical cyclone
TCHP	tropical cyclone heat potential
TD	tropical depression
WMO	World Meteorological Organization
WNP	western North Pacific

Appendix 2: Supplemental Material

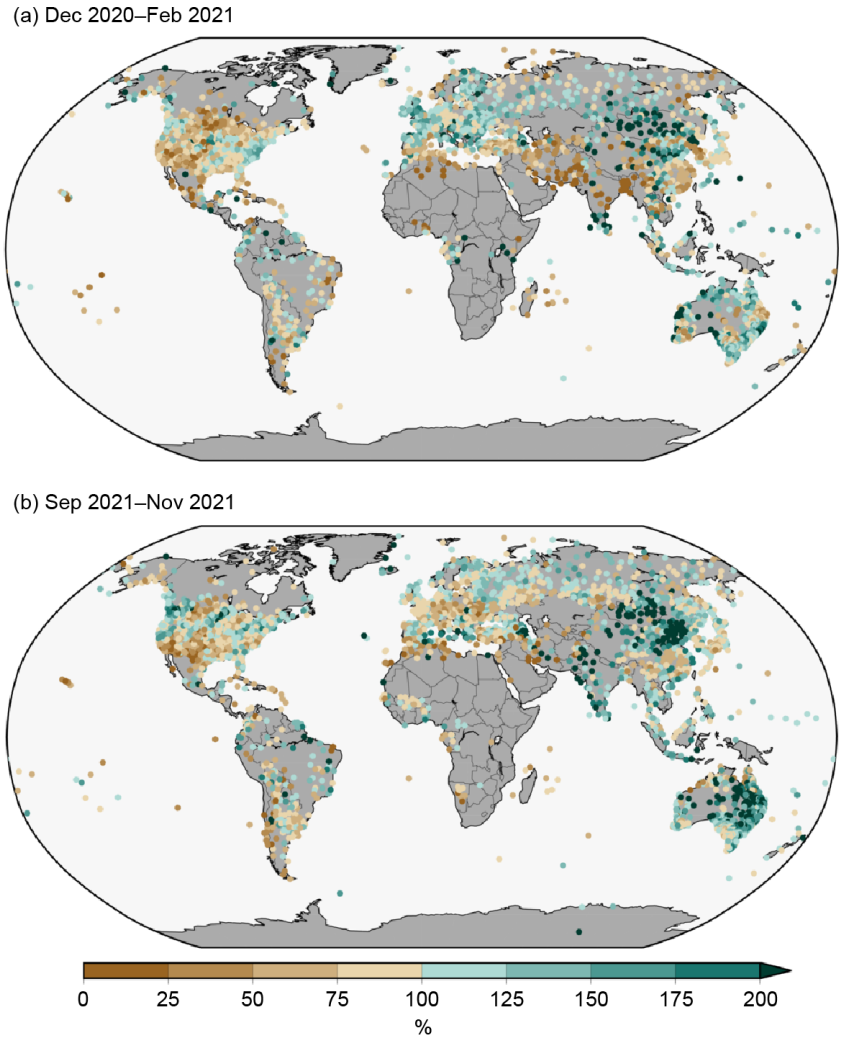

Fig. A4.1. Land-only percent of normal precipitation during (a) DJF 2020/21 and (b) SON 2021 (relative to a 1961–1990 base period). [Figure provided by NOAA NCEI and data are from GHCN-M version 4beta (Menne et al. 2017).]

References

Aiyyer, A., and J. Molinari, 2008: MJO and tropical cyclogenesis in the Gulf of Mexico and eastern Pacific: Case study and idealized numerical modeling. *J. Atmos. Sci.*, **65**, 2691–2704, https://doi.org/10.1175/2007JAS2348.1.

Aon, 2021a: Global Catastrophe Recap, August 2021, 19 pp, http://thoughtleadership.aon.com/Documents/20210009_analytics-if-august-global-recap.pdf.

——, 2021b: Global Catastrophe Recap, September 2021, 22 pp, http://thoughtleadership.aon.com/Documents/20210012-analytics-if-september-global-recap.pdf.

——, 2022: Global Catastrophe Recap, December 2021, 23 pp, https://www.aon.com/reinsurance/getmedia/e5d555d8-ade5-4fc4-b4b2-24ddad4bfb3d/20220124-analytics-if-december-global-recap.pdf.aspx.

Balaguru, K., P. Chang, R. Saravanan, L. R. Leung, Z. Xu, M. Li, and J. S. Hsieh, 2012: Ocean barrier layers' effect on tropical cyclone intensification. *Proc. Natl. Acad. Sci. USA*, **109**, 142343–142347, https://doi.org/10.1073/pnas.1201364109.

Banzon, V. F., and R. W. Reynolds, 2013: Use of WindSat to extend a microwave-based daily optimum interpolation sea surface temperature time series. *J. Climate*, **26**, 2557–2562, https://doi.org/10.1175/JCLI-D-12-00628.1.

Baxter, S., S. Weaver, J. Gottschalck, and Y. Xue, 2014: Pentad evolution of wintertime impacts of the Madden–Julian oscillation over the contiguous United States. *J. Climate*, **27**, 7356–7367, https://doi.org/10.1175/JCLI-D-14-00105.1.

Behringer, D. W., 2007: The Global Ocean Data Assimilation System (GODAS) at NCEP. *11th Symp. on Integrated Observing and Assimilation Systems for Atmosphere, Oceans, and Land Surface*, San Antonio, TX, Amer. Meteor. Soc., 3.3, http://ams.confex.com/ams/87ANNUAL/techprogram/paper_119541.htm.

——, M. Ji, and A. Leetmaa, 1998: An improved coupled model for ENSO prediction and implications for ocean initialization. Part I: The ocean data assimilation system. *Mon. Wea. Rev.*, **126**, 1013–1021, https://doi.org/10.1175/1520-0493(1998)126<1013:AICMFE>2.0.CO;2.

Bell, G. D., and M. Chelliah, 2006: Leading tropical modes associated with interannual and multi-decadal fluctuations in North Atlantic hurricane activity. *J. Climate*, **19**, 590–612, https://doi.org/10.1175/JCLI3659.1.

——, and Coauthors, 2000: The 1999 North Atlantic Hurricane season [in "Climate Assessment for 1999"]. *Bull. Amer. Meteor. Soc.*, **81** (6), S19–S22, https://doi.org/10.1175/1520-0477(2000)81[s1:CAF]2.0.CO;2.

——, E. S. Blake, C. W. Landsea, C. Wang, J. Schemm, T. Kimberlain, R. J. Pasch, and S. B. Goldenberg, 2017: Atlantic basin [in "State of the Climate in 2016"]. *Bull. Amer. Meteor. Soc.*, **98** (8), S108–S112, https://doi.org/10.1175/2017BAMSStateoftheClimate.1.

——, ——, ——, S. B. Goldenberg, and R. J. Pasch, 2018: Atlantic basin [in "State of the Climate in 2017"]. *Bull. Amer. Meteor. Soc.*, **99** (8), S114–S118, https://doi.org/10.1175/2018BAMSStateoftheClimate.1.

——, ——, ——, H. Wang, S. B. Goldenberg, and R. J. Pasch 2019: Atlantic basin [in "State of the Climate in 2018"]. *Bull. Amer. Meteor. Soc.*, **100** (9), S113–S119, https://doi.org/10.1175/2019BAMSStateoftheClimate.1.

——, E. S. Blake, C. W. Landsea, M. Rosencrans, H. Wang, S. B. Goldenberg, and R. J. Pasch, 2020: Atlantic basin [in "State of the Climate in 2019"]. *Bull. Amer. Meteor. Soc.*, **101** (7), S204–S212, https://doi.org/10.1175/BAMS-D-20-0077.1.

Berg, R., 2022: Hurricane Rick (EP172021). National Hurricane Center Tropical Cyclone Rep., 21 pp., https://www.nhc.noaa.gov/data/tcr/EP172021_Rick.pdf.

Beven, J., A. Hagen, and R. Berg, 2022: Hurricane Ida (AL092021). National Hurricane Center Tropical Cyclone Rep., 163 pp., https://www.nhc.noaa.gov/data/tcr/AL092021_Ida.pdf.

Camargo, S. J., and A. H. Sobel, 2005: Western North Pacific tropical cyclone intensity and ENSO. *J. Climate*, **18**, 2996–3006, https://doi.org/10.1175/JCLI3457.1.

——, A. W. Robertson, S. J. Gaffney, P. Smyth, and M. Ghil, 2007a: Cluster analysis of typhoon tracks: Part II: Large-scale circulation and ENSO. *J. Climate*, **20**, 3654–3676, https://doi.org/10.1175/JCLI4203.1.

——, K. A. Emanuel, and A. H. Sobel, 2007b: Use of a genesis potential index to diagnose ENSO effects on tropical cyclone genesis. *J. Climate*, **20**, 4819–4834, https://doi.org/10.1175/JCLI4282.1.

——, M. C. Wheeler, and A. H. Sobel, 2009: Diagnosis of the MJO modulation of tropical cyclogenesis using an empirical index. *J. Atmos. Sci.*, **66**, 3061–3074, https://doi.org/10.1175/2009JAS3101.1.

Cangialosi, J. P., 2021a: Hurricane Felicia (EP062021). National Hurricane Center Tropical Cyclone Rep., 15 pp., https://www.nhc.noaa.gov/data/tcr/EP062021_Felicia.pdf.

——, 2021b: Hurricane Pamela (EP162021). National Hurricane Center Tropical Cyclone Rep., 17 pp., https://www.nhc.noaa.gov/data/tcr/EP162021_Pamela.pdf.

Cassou, C., 2008: Intraseasonal interaction between the Madden–Julian Oscillation and the North Atlantic Oscillation. *Nature*, **455**, 523–527, https://doi.org/10.1038/nature07286.

Chia, H. H., and C. F. Ropelewski, 2002: The interannual variability in the genesis location of tropical cyclones in the northwest Pacific. *J. Climate*, **15**, 2934–2944, https://doi.org/10.1175/1520-0442(2002)015<2934:TIVITG>2.0.CO;2.

Chen, L., and J.-J. Luo, 2021: Indian Ocean dipole [in "State of the Climate in 2020"]. *Bull. Amer. Meteor. Soc.*, **103** (8), S21–S25, https://doi.org/10.1175/BAMS-D-21-00090.1.

Dare, R. A., and J. L. McBride, 2011: Sea surface temperature response to tropical cyclones. *Mon. Wea. Rev.*, **139**, 3798–3808, https://doi.org/10.1175/MWR-D-10-05019.1.

Diamond, H. J., and J. A. Renwick, 2015: The climatological relationship between tropical cyclones in the southwest Pacific and the Madden–Julian Oscillation. *Int. J. Climatol.*, **35**, 676–686, https://doi.org/10.1002/joc.4012.

——, and C. J. Schreck III , Eds., 2019: The tropics [in "State of the Climate in 2018"]. *Bull. Amer. Meteor. Soc.*, **100** (9), S101–S140, https://doi.org/10.1175/2019BAMSStateoftheClimate.1.

——, and ——, Eds, 2020: The tropics [in "State of the Climate in 2019"]. *Bull. Amer. Meteor. Soc.*, **100** (8), S185–S238, https://doi.org/10.1175/BAMS-D-20-0077.1.

——, and ——, Eds., 2021: The tropics [in "State of the Climate in 2020"]. *Bull. Amer. Meteor. Soc.*, **102** (8), S199–S262, https://doi.org/10.1175/BAMS-D-21-0080.1.

——, A. M. Lorrey, K. R. Knapp, and D. H. Levinson, 2012: Development of an enhanced tropical cyclone tracks database for the southwest Pacific from 1840 to 2011. *Int. J. Climatol.*, **32**, 2240–2250, https://doi.org/10.1002/joc.2412.

Ding, Q., E. J. Steig, D. S. Battisti, and J. M. Wallace, 2012: Influence of the tropics on the southern annular mode. *J. Climate*, **25**, 6330–6348, https://doi.org/10.1175/JCLI-D-11-00523.1.

Domingues, R., and Coauthors, 2015: Upper ocean response to Hurricane Gonzalo (2014): Salinity effects revealed by targeted and sustained underwater glider observations. *Geophys. Res. Lett.*, **42**, 7131–7138, https://doi.org/10.1002/2015GL065378.

Dube, S. K., D. Rao, P. C. Sinha, T. S. Murty, and N. Bahuluyan, 1997: Storm surge in the Bay of Bengal and Arabian Sea: The problem and its prediction. *Mausam*, **48**, 283–304, https://doi.org/10.54302/mausam.v48i2.4012.

Ebita, A., and Coauthors, 2011: The Japanese 55-year Reanalysis "JRA-55": An interim report. *SOLA*, **7**, 149–152, https://doi.org/10.2151/sola.2011-038.

Emanuel, K. A., 1988: The maximum intensity of hurricanes. *J. Atmos. Sci.*, **45**, 1143–1155, https://doi.org/10.1175/1520-0469(1988)045<1143:TMIOH>2.0.CO;2.

——, and D. S. Nolan, 2004: Tropical cyclone activity and the global climate system. *26th Conf. on Hurricanes and Tropical Meteorology*, Miami, FL, Amer. Meteor. Soc., 10A.2, https://ams.confex.com/ams/26HURR/techprogram/paper_75463.htm.

Enfield, D. B., and A. M. Mestas-Nuñez, 1999: Multiscale variabilities in global sea surface temperatures and their relationships with tropospheric climate patterns. *J. Climate*, **12**, 2719–2733, https://doi.org/10.1175/1520-0442(1999)012<2719:MVIGSS>2.0.CO;2.

Feng, M., M. J. McPhaden, S. Xie, and J. Hafner, 2013: La Niña forces unprecedented Leeuwin Current warming in 2011. *Sci. Rep.*, **3**, 1277. https://doi.org/10.1038/srep01277.

Frank, W. M., and P. E. Roundy, 2006: The role of tropical waves in tropical cyclogenesis. *Mon. Wea. Rev.*, **134**, 2397–2417, https://doi.org/10.1175/MWR3204.1.

Gill, A. E., 1980: Some simple solutions for heat-induced tropical circulation. *Quart. J. Roy. Meteor. Soc.*, **106**, 447–462, https://doi.org/10.1002/qj.49710644905.

Goldenberg, S. B., and L. J. Shapiro, 1996: Physical mechanisms for the association of El Niño and West African rainfall with Atlantic major hurricane activity. *J. Climate*, **9**, 1169–1187, https://doi.org/10.1175/1520-0442(1996)009<1169:PMFTAO>2.0.CO;2.

——, C. W. Landsea, A. M. Mestas-Nuñez, and W. M. Gray, 2001: The recent increase in Atlantic hurricane activity: Causes and implications. *Science*, **293**, 474–479, https://doi.org/10.1126/science.1060040.

Goni, G. J., and Coauthors, 2009: Applications of satellite-derived ocean measurements to tropical cyclone intensity forecasting. *Oceanography*, **22**, 190–197, https://doi.org/10.5670/oceanog.2009.78.

——, and Coauthors, 2017: Autonomous and Lagrangian ocean observations for Atlantic tropical cyclone studies and forecasts. *Oceanography*, **30**, 92–103, https://doi.org/10.5670/oceanog.2017.227.

Gray, W. M., 1990: Strong association between West African rainfall and U.S. landfall of intense hurricanes. *Science*, **249**, 1251–1256, https://doi.org/10.1126/science.249.4974.1251.

Guo, Y., X. Jiang, and D. E. Waliser, 2014: Modulation of the convectively coupled Kelvin waves over South America and the tropical Atlantic Ocean in association with the Madden–Julian Oscillation. *J. Atmos. Sci.*, **71**, 1371–1388, https://doi.org/10.1175/JAS-D-13-0215.1.

Hastenrath, S., 1990: Decadal-scale changes of the circulation in the tropical Atlantic sector associated with Sahel drought. *Int. J. Climatol.*, **10**, 459–472, https://doi.org/10.1002/joc.3370100504.

Hendon, H., C. Zhang, and J. Glick, 1999: Interannual variation of the Madden–Julian oscillation during austral summer. *J. Climate*, **12**, 2538–2550, https://doi.org/10.1175/1520-0442(1999)012<2538:IVOTMJ>2.0.CO;2.

Hersbach, H., and Coauthors, 2020: The ERA5 global reanalysis. *Quart. J. Roy. Meteor. Soc.*, **146**, 1999–2049, https://doi.org/10.1002/qj.3803.

Hong, C.-C., T. Li, and J.-J. Luo, 2008: Asymmetry of the Indian Ocean Dipole. Part II: Model diagnosis. *J. Climate*, **21**, 4849–4858.

Huang, B., and Coauthors, 2017: Extended Reconstructed Sea Surface Temperature, version 5 (ERSSTv5): Upgrades, validations, and intercomparisons. *J. Climate*, **30**, 8179–8205, https://doi.org/10.1175/JCLI-D-16-0836.1.

Huang, B., C. Liu, V. Banzon, E. Freeman, G. Graham, B. Hankins, T. Smith, and H.-M. Zhang, 2020: Improvements of the Daily Optimum Interpolation Sea Surface Temperature (DOISST) version 2.1. *J. Climate*, **34**, 2923–2939, https://doi.org/10.1175/JCLI-D-20-0166.1.

Huffman, G. J., R. F. Adler, D. T. Bolvin, and G. Gu, 2009: Improving the global precipitation record: GPCP version 2.1. *Geophys. Res. Lett.*, **36**, L17808, https://doi.org/10.1029/2009GL040000.

IMD, 2021: Extremely Severe Cyclonic Storm TAUKTAE over the Arabian Sea (14th–19th May, 2021): A report. India Meteorological Department, 64 pp., https://rsmcnewdelhi.imd.gov.in/uploads/report/26/26_e0cc1a_Preliminary%20Report%20on%20ESCS%20TAUKTAE-19july.pdf.

Kalnay, E., and Coauthors, 1996: The NCEP/NCAR 40-Year Reanalysis Project. *Bull. Amer. Meteor. Soc.*, **77**, 437–471, https://doi.org/10.1175/1520-0477(1996)077<0437:TNYRP>2.0.CO;2.

Kayano, M., and V. Kousky, 1999: Intraseasonal (30–60 day) variability in the global tropics: Principal modes and their evolution. *Tellus*, **51**, 373–386, https://doi.org/10.3402/tellusa.v51i3.13459.

Kiladis, G. N., and K. M. Weickmann, 1992: Circulation anomalies associated with tropical convection during northern winter. *Mon. Wea. Rev.*, **120**, 1900–1923, https://doi.org/10.1175/1520-0493(1992)120<1900:CAAWTC>2.0.CO;2.

——, K. H. Straub, and P. T. Haertel, 2005: Zonal and vertical structure of the Madden–Julian oscillation. *J. Atmos. Sci.*, **62**, 2790–2809, https://doi.org/10.1175/JAS3520.1.

——, M. C. Wheeler, P. T. Haertel, K. H. Straub, and P. E. Roundy, 2009: Convectively coupled equatorial waves. *Rev. Geophys.*, **47**, RG2003, https://doi.org/10.1029/2008RG000266.

Klotzbach, P. J., K. M. Wood, C. J. Schreck III, S. G. Bowen, C. M. Patricola, and M. M. Bell, 2022: Trends in global tropical cyclone activity: 1990–2021. *Geophys. Res. Lett.*, **49**, e2021GL095774, https://doi.org/10.1029/2021GL095774.

Knaff, J. A., C. R. Sampson, and K. D. Musgrave, 2018: An operational rapid intensification prediction aid for the western North Pacific. *Wea. Forecasting*, **33**, 799–811, https://doi.org/10.1175/WAF-D-18-0012.1.

Knapp, K. R., M. C. Kruk, D. H. Levinson, H. J. Diamond, and C. J. Neumann, 2010: The International Best Track Archive for Climate Stewardship (IBTrACS): Unifying tropical cyclone data. *Bull. Amer. Meteor. Soc.*, **91**, 363–376, https://doi.org/10.1175/2009BAMS2755.1.

——, J. A. Knaff, C. R. Sampson, G. M. Riggio, and A. D. Schnapp, 2013: A pressure-based analysis of the historical western North Pacific tropical cyclone intensity record. *Mon. Wea. Rev.*, **141**, 2611–2631, https://doi.org/10.1175/MWR-D-12-00323.1.

Knutson, T. R., and K. M. Weickmann, 1987: 30–60 day atmospheric oscillations: Composite life cycles of convection and circulation anomalies. *Mon. Wea. Rev.*, **115**, 1407–1436, https://doi.org/10.1175/1520-0493(1987)115<1407:DAOCLC>2.0.CO;2.

Kousky, V. E., and M. T. Kayano, 1994: Principal modes of outgoing longwave radiation and 250-mb circulation for the South American sector. *J. Climate*, **7**, 1131–1143, https://doi.org/10.1175/1520-0442(1994)007<1131:PMOOLR>2.0.CO;2.

Krishnamurti, T. N., and D. Subrahmanyam, 1982: The 30–50 day mode at 850 mb during MONEX. *J. Atmos. Sci.*, **39**, 2088–2095, https://doi.org/10.1175/1520-0469(1982)039<2088:TDMAMD>2.0.CO;2.

Landsea, C. W., and J. L. Franklin, 2013: Atlantic hurricane database uncertainty and presentation of a new database format. *Mon. Wea. Rev.*, **141**, 3576–3592, https://doi.org/10.1175/MWR-D-12-00254.1.

——, W. M. Gray, P. W. Mielke, and K. J. Berry, 1992: Long-term variations of western Sahelian monsoon rainfall and intense U.S. landfalling hurricanes. *J. Climate*, **5**, 1528–1534, https://doi.org/10.1175/1520-0442(1992)005<1528:LTVOWS>2.0.CO;2.

——, G. D. Bell, W. M. Gray, and S. B. Goldenberg, 1998: The extremely active 1995 Atlantic hurricane season: Environmental conditions and verification of seasonal forecasts. *Mon. Wea. Rev.*, **126**, 1174–1193, https://doi.org/10.1175/1520-0493(1998)126<1174:TEAAHS>2.0.CO;2.

——, G. A. Vecchi, L. Bengtsson, and T. R. Knutson, 2010: Impact of duration thresholds on Atlantic tropical cyclone counts. *J. Climate*, **23**, 2508–2519, https://doi.org/10.1175/2009JCLI3034.1.

Latto, A., 2021: Hurricane Enrique (EP052021). National Hurricane Center Tropical Cyclone Rep., 20 pp., https://www.nhc.noaa.gov/data/tcr/EP052021_Enrique.pdf.

——, 2022: Hurricane Olaf (EP152021). National Hurricane Center Tropical Cyclone Rep., 21 pp., https://www.nhc.noaa.gov/data/tcr/EP152021_Olaf.pdf.

Lau, W. K.-M., and D. E. Waliser, 2012: *Intraseasonal Variability in the Atmosphere-Ocean Climate System*. Springer, 642 pp.

Leipper, D. F., and D. Volgenau, 1972: Hurricane heat potential of the Gulf of Mexico. *J. Phys. Oceanogr.*, **2**, 218–224, https://doi.org/10.1175/1520-0485(1972)002<0218:HHPOTG>2.0.CO;2.

Liebmann, B., and C. A. Smith, 1996: Description of a complete (interpolated) outgoing longwave radiation dataset. *Bull. Amer. Meteor. Soc.*, **77**, 1275–1277, https://doi.org/10.1175/1520-0477-77.6.1274.

Lin, I. I., and Coauthors, 2013: An ocean coupling potential intensity index for tropical cyclones. *Geophys. Res. Lett.*, **40**, 1878–1882, https://doi.org/10.1002/grl.50091.

Lin, H., G. Brunet, and J. Derome, 2009: An observed connection between the North Atlantic oscillation and the Madden–Julian oscillation. *J. Climate*, **22**, 364–380, https://doi.org/10.1175/2008JCLI2515.1.

——, I.-F. Pun, and C.-C. Lien, 2014: "Category-6" Supertyphoon Haiyan in global warming hiatus: Contribution from subsurface ocean warming. *Geophys. Res. Lett.*, **41**, 8547–8553, https://doi.org/10.1002/2014GL061281.

——, and Coauthors, 2020: ENSO and tropical cyclones. *El Niño Southern Oscillation in a Changing Climate, Geophys. Monogr.*, Vol. 253, Amer. Geophys. Union, 377–408, https://doi.org/10.1002/9781119548164.ch17.

Liu, T., J. Li, C. Sun, T. Lian, and Y. Zhang, 2021: Impact of the April–May SAM on central Pacific Ocean sea temperature over the following three seasons. *Climate Dyn.*, **57**, 775–786, https://doi.org/10.1007/s00382-021-05738-4.

Luo, J.-J., 2017: Indian Ocean dipole [in "State of the Climate in 2016"]. *Bull. Amer. Meteor. Soc.*, **98** (8), S126–S128, https://doi.org/10.1175/2017BAMSStateoftheClimate.1.

——, S. Masson, S. Behera, and T. Yamagata, 2007: Experimental forecasts of the Indian Ocean Dipole using a coupled OAGCM. *J. Climate*, **20**, 2178–2190, https://doi.org/10.1175/JCLI4132.1.

——, R. Zhang, S. K. Behera, Y. Masumoto, F.-F. Jin, R. Lukas, and T. Yamagata, 2010: Interaction between El Niño and extreme Indian Ocean dipole. *J. Climate*, **23**, 726–742, https://doi.org/10.1175/2009JCLI3104.1.

——, W. Sasaki, and Y. Masumoto, 2012: Indian Ocean warming modulates Pacific climate change. *Proc. Natl. Acad. Sci. USA*, **109**, 18 701–18 706, https://doi.org/10.1073/pnas.1210239109.

Madden, R., and P. Julian, 1971: Detection of a 40–50 day oscillation in the zonal wind in the tropical Pacific. *J. Atmos. Sci.*, **28**, 702–708, https://doi.org/10.1175/1520-0469(1971)028<0702:DOADOI>2.0.CO;2.

——, and ——, 1972: Description of global-scale circulation cells in the tropics with a 40–50 day period. *J. Atmos. Sci.*, **29**, 1109–1123, https://doi.org/10.1175/1520-0469(1972)029<1109:DOGSCC>2.0.CO;2.

——, and ——, 1994: Observations of the 40–50-day tropical oscillation: A review. *Mon. Wea. Rev.*, **122**, 814–837, https://doi.org/10.1175/1520-0493(1994)122<0814:OOTDTO>2.0.CO;2.

Magee, A. D., A. S. Kiem, and A. M. Lorrey, 2022: Insights into the usefulness of a new extreme weather guidance tool: The Long-Range Tropical Cyclone Outlook for the Southwest Pacific (TCO-SP). *Bull. Amer. Meteor. Soc.*, **103**, E1220–E1233, https://doi.org/10.1175/BAMS-D-21-0108.1.

Mainelli, M., M. DeMaria, L. Shay, and G. Goni, 2008: Application of oceanic heat content estimation to operational forecasting of recent Atlantic category 5 hurricanes. *Wea. Forecasting*, **23**, 3–16, https://doi.org/10.1175/2007WAF2006111.1.

Maloney, E. D., and D. L. Hartmann, 2001: The Madden–Julian Oscillation, barotropic dynamics, and North Pacific tropical cyclone formation. Part I: Observations. *J. Atmos. Sci.*, **58**, 2545–2558, https://doi.org/10.1175/1520-0469(2001)058<2545:TMJOBD>2.0.CO;2.

Matsuno, T., 1966: Quasi-geostrophic motions in the equatorial area. *J. Meteor. Soc. Japan*, **44**, 25–43, https://doi.org/10.2151/jmsj1965.44.1_25.

Matthews, A. J., 2008: Primary and successive events in the Madden–Julian Oscillation. *Quart. J. Roy. Meteor. Soc.*, **134**, 439–453, https://doi.org/10.1002/qj.224.

Mo, K. C., 2000: The association between intraseasonal oscillations and tropical storms in the Atlantic Basin. *Mon. Wea. Rev.*, **128**, 4097–4107, https://doi.org/10.1175/1520-0493(2000)129<4097:TABIOA>2.0.CO;2.

——, and V. E. Kousky, 1993: Further analysis of the relationship between circulation anomaly patterns and tropical convection. *J. Geophys. Res.*, **98**, 5103–5113, https://doi.org/10.1029/92JD02952.

Moreno, P. I., and Coauthors, 2018: Onset and evolution of southern annular mode-like changes at centennial timescale. *Sci. Rep.*, **8**, 3458, https://doi.org/10.1038/s41598-018-21836-6.

Münnich, M., and J. D. Neelin, 2005: Seasonal influence of ENSO on the Atlantic ITCZ and equatorial South America. *Geophys. Res. Lett.*, **32**, L21709, https://doi.org/10.1029/2005GL023900.

NOAA, 2020: El Niño/Southern Oscillation (ENSO) diagnostic discussion. NOAA/NWS, 10 September, https://www.cpc.ncep.noaa.gov/products/analysis_monitoring/enso_disc_sep2020/ensodisc.shtml.

——, 2021: El Niño/Southern Oscillation (ENSO) diagnostic discussion. NOAA/NWS, 12 August, https://www.cpc.ncep.noaa.gov/products/analysis_monitoring/enso_disc_aug2021/ensodisc.shtml.

Nobre, P., and J. Shukla, 1996: Variations of sea surface temperature, wind stress and rainfall over the tropical Atlantic and South America. *J. Climate*, **9**, 2464–2479, https://doi.org/10.1175/1520-0442(1996)009<2464:VOSSTW>2.0.CO;2.

Papin, P. P., 2022: Tropical Storm Dolores (EP042021). National Hurricane Center Tropical Cyclone Rep., 20 pp., https://www.nhc.noaa.gov/data/tcr/EP042021_Dolores.pdf.

Pezza, A. B., and A. S. Coelho, 2021: Atlantic [in "State of the Climate in 2020"]. *Bull. Amer. Meteor. Soc.*, **102** (9), S215–S216, https://doi.org/10.1175/BAMS-D-21-0080.1.

Raga, G. B., B. Bracamontes-Ceballos, L. Farfán, and R. Romero-Centeno, 2013: Landfalling tropical cyclones on the Pacific coast of Mexico: 1850–2010. *Atmósfera*, **26**, 209–220, https://doi.org/10.1016/S0187-6236(13)71072-5.

Ramage, C. S., 1971: *Monsoon Meteorology*. Academic Press, 296 pp.

Reinhart, B. J., D. Wroe, and S. Houston, 2021: Hurricane Linda (EP122021). National Hurricane Center Tropical Cyclone Rep.,19 pp., https://www.nhc.noaa.gov/data/tcr/EP122021_Linda.pdf.

Reynolds, R. W., N. A. Rayner, T. M. Smith, D. C. Stokes, and W. Wang, 2002: An improved in situ and satellite SST analysis for climate. *J. Climate*, **15**, 1609–1625, https://doi.org/10.1175/1520-0442(2002)015<1609:AIISAS>2.0.CO;2.

Riddle, E., M. Stoner, N. Johnson, M. L'Heureux, D. Collins, and S. Feldstein, 2013: The impact of the MJO on clusters of wintertime circulation anomalies over the North American region. *Climate Dyn.*, 40, 1749–1766, https://doi.org/10.1007/s00382-012-1493-y.

Ropelewski, C. F., and M. S. Halpert, 1987: Global and regional scale precipitation patterns associated with the El Niño–Southern Oscillation. *Mon. Wea. Rev.*, **115**, 1606–1626, https://doi.org/10.1175/1520-0493(1987)115<1606:GARSPP>2.0.CO;2.

——, and ——, 1989: Precipitation patterns associated with the high index phase of the Southern Oscillation. *J. Climate*, **2**, 268–284, https://doi.org/10.1175/1520-0442(1989)002<0268:PPAWTH>2.0.CO;2.

Saha, S., and Coauthors, 2014: The NCEP Climate Forecast System version 2. *J. Climate*, **27**, 2185–2208, https://doi.org/10.1175/JCLI-D-12-00823.1.

Saji, N. H., B. N. Goswami, P. N. Vinayachandran, and T. Yamagata, 1999: A dipole mode in the tropical Indian ocean. *Nature*, **401**, 360–363, https://doi.org/10.1038/43854.

Schneider, T., T. Bischoff, and G. H. Haug, 2014: Migrations and dynamics of the intertropical convergence zone. *Nature*, **513**, 45–53, https://doi.org/10.1038/nature13636.

Schreck, C. J., 2015: Kelvin waves and tropical cyclogenesis: A global survey. *Mon. Wea. Rev.*, **143**, 3996–4011, https://doi.org/10.1175/MWR-D-15-0111.1.

——, 2016: Convectively coupled Kelvin waves and tropical cyclogenesis in a semi-Lagrangian framework. *Mon. Wea. Rev.*, **144**, 4131–4139, https://doi.org/10.1175/MWR-D-16-0237.1.

——, and J. Molinari, 2011: Tropical cyclogenesis associated with Kelvin waves and the Madden–Julian oscillation. *Mon. Wea. Rev.*, **139**, 2723–2734, https://doi.org/10.1175/MWR-D-10-05060.1.

——, ——, and A. Aiyyer, 2012: A global view of equatorial waves and tropical cyclogenesis. *Mon. Wea. Rev.*, **140**, 774–788, https://doi.org/10.1175/MWR-D-11-00110.1.

——, J. M. Cordeira, and D. Margolin, 2013: Which MJO events affect North American temperatures? *Mon. Wea. Rev.*, **141**, 3840–3850, https://doi.org/10.1175/MWR-D-13-00118.1.

——, K. R. Knapp, and J. P. Kossin, 2014: The impact of best track discrepancies on global tropical cyclone climatologies using IBTrACS. *Mon. Wea. Rev.*, **142**, 3881–3899, https://doi.org/10.1175/MWR-D-14-00021.1.

——, H.-T. Lee, and K. R. Knapp, 2018: HIRS outgoing longwave radiation—Daily climate data record: Application toward identifying tropical subseasonal variability. *Remote Sens.*, **10**, 1325, https://doi.org/10.3390/rs10091325.

Shay, L. K., G. J. Goni, and P. G. Black, 2000: Effects of a warm oceanic feature on Hurricane Opal. *Mon. Wea. Rev.*, **128**, 1366–1383, https://doi.org/10.1175/1520-0493(2000)128<1366:EOAWOF>2.0.CO;2.

Smith, T. M., R. W. Reynolds, T. C. Peterson, and J. Lawrimore, 2008: Improvements to NOAA's historical merged land–ocean surface temperature analysis (1880–2006). *J. Climate*, **21**, 2283–2296, https://doi.org/10.1175/2007JCLI2100.1.

Vecchi, G. A., and B. J. Soden, 2007: Effect of remote sea surface temperature change on tropical cyclone potential intensity. *Nature*, **450**, 1066–1071, https://doi.org/10.1038/nature06423.

Ventrice, M. J., C. D. Thorncroft, and M. A. Janiga, 2012a: Atlantic tropical cyclogenesis: A three-way interaction between an African easterly wave, diurnally varying convection, and a convectively coupled atmospheric Kelvin wave. *Mon. Wea. Rev.*, **140**, 1108–1124, https://doi.org/10.1175/MWR-D-11-00122.1.

Ventrice, M. J., C. D. Thorncroft, and C. J. Schreck, 2012b: Impacts of convectively coupled Kelvin waves on environmental conditions for Atlantic tropical cyclogenesis. *Mon. Wea. Rev.*, **140**, 2198–2214, https://doi.org/10.1175/MWR-D-11-00305.1.

Villarini, G., G. A. Vecchi, T. R. Knutson, and J. A. Smith, 2011: Is the recorded increase in short duration North Atlantic tropical storms spurious? *J. Geophys. Res.*, **116**, D10114, https://doi.org/10.1029/2010JD015493.

Vincent, D. G., 1994: The South Pacific Convergence Zone (SPCZ): A review. *Mon. Wea. Rev.*, **122**, 1949–1970, https://doi.org/10.1175/1520-0493(1994)122<1949:TSPCZA>2.0.CO;2.

Waliser, D. E., and C. Gautier, 1993: A satellite-derived climatology of the ITCZ. *J. Climate*, **6**, 2162–2174, https://doi.org/10.1175/1520-0442(1993)006<2162:ASDCOT>2.0.CO;2.

Wang, B., 1994: Climatic regimes of tropical convection and rainfall. *J. Climate*, **7**, 1109–1118, https://doi.org/10.1175/1520-0442(1994)007<1109:CROTCA>2.0.CO;2.

——, and Q. Ding, 2008: Global monsoon: Dominant mode of annual variation in the tropics. *Dyn. Atmos. Ocean*, **44**, 165–183, https://doi.org/10.1016/j.dynatmoce.2007.05.002.

——, J. Liu, H. J. Kim, P. J. Webster, and S. Y. Yim, 2012: Recent change of the global monsoon precipitation (1979–2008). *Climate Dyn.*, **39**, 1123–1135, https://doi.org/10.1007/s00382-011-1266-z.

Wheeler, M. C., and G. N. Kiladis, 1999: Convectively coupled equatorial waves: Analysis of clouds and temperature in the wavenumber-frequency domain. *J. Atmos. Sci.*, **56**, 374–399, https://doi.org/10.1175/1520-0469(1999)056<0374:CCEWAO>2.0.CO;2.

——, and H. H. Hendon, 2004: An all-season real-time multivariate MJO index: Development of an index for monitoring and prediction. *Mon. Wea. Rev.*, **132**, 1917–1932, https://doi.org/10.1175/1520-0493(2004)132<1917:AARMMI>2.0.CO;2.

Wood, K. M., and E. A. Ritchie, 2015: A definition for rapid weakening in the North Atlantic and eastern North Pacific. *Geophys. Res. Lett.*, **42**, 10 091–10 097, https://doi.org/10.1002/2015GL066697.

——, and C. J. Schreck, 2020: Eastern North Pacific and Central North Pacific basins [in "State of the Climate in 2019"]. *Bull. Amer. Meteor. Soc.*, **101** (8), S212–S214, https://doi.org/10.1175/BAMS-D-20-0077.1.

——, and ——, 2021: Eastern North Pacific and Central North Pacific basins [in "State of the Climate in 2020"]. *Bull. Amer. Meteor. Soc.*, **102** (8), S233–S236, https://doi.org/10.1175/BAMS-D-21-0080.1.

Xie, P., and P. A. Arkin, 1997: Global precipitation: A 17-year monthly analysis based on gauge observations, satellite estimates, and numerical model outputs. *Bull. Amer. Meteor. Soc.*, **78**, 2539–2558, https://doi.org/10.1175/1520-0477(1997)078<2539:GPAYMA>2.0.CO;2.

Yim, S. Y., B. Wang, J. Liu, and Z. W. Wu, 2014: A comparison of regional monsoon variability using monsoon indices. *Climate Dyn.*, **43**, 1423–1437, https://doi.org/10.1007/s00382-013-1956-9.

Zhang, C., 2005: Madden–Julian oscillation. *Rev. Geophys.*, **43**, RG2003, https://doi.org/10.1029/2004RG000158.

——, and J. Gottschalck, 2002: SST anomalies of ENSO and the Madden–Julian oscillation in the equatorial Pacific. *J. Climate*, **15**, 2429–2445, https://doi.org/10.1175/1520-0442(2002)015<2429:SAOEAT>2.0.CO;2.

Zhang, H.-M., and Coauthors, 2019: Updated temperature data give a sharper view of climate trends. *Eos*, **100**, https://doi.org/10.1029/2019EO128229.

Zheng, T., T. Feng, K. Xu, and X. Cheng, 2020: Precipitation and the associated moist static energy budget off Western Australia in conjunction with Ningaloo Niño. *Front. Earth Sci.*, **8**, https://doi.org/10.3389/feart.2020.597915

Zheng, Z.-W., I.-I. Lin, B. Wang, H.-C. Huang, and C.-H. Chen, 2015: A long neglected damper in the El Nino–typhoon relationship: A 'Gaia-like' process. *Sci. Rep.*, **5**, 11103, https://doi.org/10.1038/srep11103.